SCANNING TUNNELING MICROSCOPY AND SPECTROSCOPY OF

DEFECTS IN LOW-DIMENSIONAL MATERIALS

by

JON M. MILLS

A DISSERTATION

Presented to the Department of Chemistry and Biochemistry
and the Division of Graduate Studies of the University of Oregon
in partial fulfillment of the requirements
for the degree of
Doctor of Philosophy

December 2021

DISSERTATION APPROVAL PAGE

Student: Jon M. Mills

Title: Scanning Tunneling Microscopy and Spectroscopy of Defects in Low-Dimensional Materials

This dissertation has been accepted and approved in partial fulfillment of the requirements for the Doctor of Philosophy degree in the Department of Chemistry and Biochemistry by:

James S. Prell	Chairperson
George V. Nazin	Advisor
James E. Hutchison	Core Member
Hailin Wang	Institutional Representative

and

Krista Chronister	Vice Provost for Graduate Studies

Original approval signatures are on file with the University of Oregon Division of Graduate Studies.

Degree awarded December 2021

DISSERTATION ABSTRACT

Jon M. Mills

Doctor of Philosophy

Department of Chemistry and Biochemistry

December 2021

Title: Scanning Tunneling Microscopy and Spectroscopy of Defects in
 Low-Dimensional Materials

With semiconductor device dimensions shrinking to smaller and
smaller sizes the individual components become more susceptible to
surface or interface atomic defects, as the surface atoms are a larger
percentage of the whole device, the interface electronic structure quickly
becomes the electronic structure of the whole device. Here we use
scanning tunneling microscopy and scanning tunneling spectroscopy
(STM/STS) along with density functional theory (DFT) calculations to
investigate the impact of the atomic scale defects on the local density of
states (LDOS) of a variety of low-dimensional materials. First, we will
show work investigating defects in hydrogen-passivated silicon
nanocrystals deposited on the Au(111) surface. Using two-dimensional
STS spatial mapping we will show both localized and delocalized defect
induced states in the LDOS. We will show how surface reconstruction or
single-atom defects account for the changes in the LDOS. Then we will
report on an exotic two-dimensional structure, an alkali halide ultra-thin
film with trigonal planar coordination. Using a combination of STM and

DFT we will show, for the first time, how a submonolayer of rubidium iodide coordinates to the Ag(111) substrate, and how upon increasing monolayer coverage the RbI film will reconstruct into the traditional (100) terminated structure. We will end with a study of the impact of defects in an ultra-thin film dielectric on the electronic structure of single walled carbon nanotubes. The research presented in this dissertation increases our understanding of how atomic defects impact the electronic structure of low-dimensional materials,

This dissertation includes both previously published and unpublished co-authored material.

CURRICULUM VITAE

NAME OF AUTHOR: Jon M. Mills

GRADUATE AND UNDERGRADUATE SCHOOLS ATTENDED:

University of Oregon, Eugene
Texas State University, San Marcos

DEGREES AWARDED:

Doctor of Philosophy, Chemistry, 2021, University of Oregon
Bachelor of Science, Chemistry, 2013, Texas State University

AREAS OF SPECIAL INTEREST:

Scanning Tunneling Microscopy
Scanning Tunneling Spectroscopy

PROFESSIONAL EXPERIENCE:

Graduate Research Assistant, Department of Chemistry and
Biochemistry, University of Oregon, Eugene, OR, 2014-2021

Graduate Teaching Assistant, Department of Chemistry and
Biochemistry, University of Oregon, Eugene, OR, 2013-2021

PUBLICATIONS:

Kislitsyn, D. A.; Mills, J. M.; Chiu, S. K.; Taber, B. N.; Barnes, J.D.; Gervasi, C. F.; Goforth, A. M.; Nazin, G. V. Creation and Annihilation of Charge Traps in Silicon Nanocrystals: Experimental Visualization and Spectroscopy. J. Phys. Chem. Lett. **2018**, 9, 710.

Taber, B. N.; Gervasi, C. F.; Mills, J. M.; Kislitsyn, D. A.; Darzi, E. R.; Crowley, W. G.; Jasti, R.; Nazin, G. V. Quantum Confinement of Surface Electrons by Molecular Nanohoop Corrals. *J. Phys. Chem. Lett.* **2016**, 7, 3073.

Kislitsyn, D. A.; Mills, J. M.; Kocevski, V.; Chiu, S. K.; DeBenedetti, W. J. I.; Gervasi, C. F.; Taber, B. N.; Rosenfield, A. E.; Eriksson, O.; Rusz, J.; Goforth, A. M.; Nazin, G. V. Communication: Visualization and

Spectroscopy of Defects Induced by Dehydrogenation in Individual Silicon Nanocrystals. *J. Chem. Phys.* **2016**, 144, 5.

Taber, B. N.; Kislitsyn, D. A.; Gervasi, C. F.; Mills, J. M.; Rosenfield, A. E.; Zhang, L.; Mannsfeld, S. C. B.; Prell, J. S.; Briseno, A. L.; Nazin, G. V. Real-Space Visualization of Conformation-Independent Oligothiophene Electronic Structure. *J. Chem. Phys.* **2016**, 144, 7.

Kislitsyn, D. A.; Kocevski, V.; Mills, J. M.; Chiu, S. K.; Gervasi, C. F.; Taber, B. N.; Rosenfield, A. E.; Eriksson, O.; Rusz, J.; Goforth, A. M.; Nazin, G. V. Mapping of Defects in Individual Silicon Nanocrystals Using Real-Space Spectroscopy. *J. Phys. Chem. Lett.* **2016**, 7, 1047.

ACKNOWLEDGMENTS

To those who inspired it
and will not read it.

TABLE OF CONTENTS

LIST OF FIGURES

B.1. Impact of the finite bias voltage drop inside a SiNC on the STS spectra. (a) "Direct" tunnelling through an occupied electronic state with energy E_S below the Fermi level (E_F) of the Au(111) substrate (corresponding states shown in blue). In a biased tunnel junction involving a SiNC (corresponding states shown in red), a finite voltage drop occurs across the SiNC volume changing the energy of all electronic states by $\alpha e V_B$, where V_B is the bias voltage, and $\alpha < 1$ is a function of the SiNC dimensions and dielectric susceptibility. Tunnelling into the state thus occurs when the Fermi level of the tip is aligned with the electronic state, which happens when $E_S = (1 - \alpha)eV_B$ (here, and everywhere in Figure B.1, we assume that all quantities are positive). The onset tunnelling voltage can thus be calculated as $E_S/(1 - \alpha)$.[9, 10] (b) "Reverse" tunneling through an

LIST OF TABLES

CHAPTER I

INTRODUCTION

1.1. Background

The scanning tunneling microscopy (STM), invented by Binning et al.[1-3] in 1982, helped pioneer the field of atomic-scale science. The STM is uniquely able to characterize both the electronic and topographic properties of surfaces with sub-nanometer resolution in real space, this capability has allowed scientists to obtain real space images, and more importantly, spectroscopy with atomic precision. One of the first tests of the STM was to image the 7×7 reconstruction of the Si(111) surface.[4] Even though a number of different experiments using several different surface techniques has been performed, there was disagreement over which of the possible atomic models was correct.[5-10] The real space images provided by STM settled the debate, identifying the dimer-adatom-stacking-fault model first proposed by Takayanagi et al.[11] as the correct Si(111)-(7×7) surface structure, a complex structure with a 49 atom unit cell, thus proving that STM is an indispensable research tool.

There are numerous different designs for STMs, the "louse" type piezoelectric walkers used by Binnig and Rohrer in the first STM,[1] the inch-worm types,[12] there are piezoelectric (piezo) driven slip–stick motors such as the Besocke-type beetle,[13] or the Pan style used in this dissertation,[14] there are even STMs that use a micrometer screw drive

(these are predominantly used by enthusiasts that build low-cost STMs at home) that are either manually controlled or use a stepper motor.

The requirements for instruments with atomic resolution place a number of constraints on the designs; low frequency vibrations, thermal drift, and electrical noise are the biggest obstacles. In order to combat these factors and improve the capabilities of STMs a number of methods have been introduced such as the use of, ultra-high vacuum (UHV) environments, cryogenic temperatures, and ultrathin insulating layers. UHV (pressure less than 10^{-9} torr) environments allow for the creation of atomically flat and atomically clean surfaces, it decouples the STM from air acoustic vibrations, and prevents airborne contaminants from affecting the tunneling current. Cryogenic operating temperatures have numerous benefits including, freezing weekly bound physiosorbed molecules on the substrate surface, increasing the mechanical stability of the STM, reducing the thermal drift of the instrument itself, reducing the thermal noise in the electronic signal, and reducing thermal broadening in scanning tunneling spectroscopy (STS). The use of ultra-thin dielectric layers decouples the adsorbates from the metallic surface reducing the coupling further improving STS resolution, and allowing for the imaging of molecular orbitals of the adsorbed molecules without the hybridization of the orbitals with the metal substrate.[15]

These improvements have allowed scientists to develop numerous novel experiments such as; inelastic electron tunneling spectroscopy,[16-17]

a technique which requires a very stable tip-sample junction, which is insensitive to mechanical vibrations, but allows for vibrational spectroscopy of molecules with single-bond sensitivity; or when a magnetic field is applied to the tunneling junction. allowing for the measurement of real space and momentum space properties of magnetic vortices within type-II superconductors,[18] the addition of a magnetic field also allows for the measurement of the energy required to flip the spin of a single atom;[19] STM induced luminescence spectroscopy allows for the investigations of the optical properties of nanostructures on the atomic scale.[20-21]

1.2. Motivation

Moore's Law (an observation that transistor density doubles about every two years)[22] necessitates that the smallest parts of transistors have to shrink by a factor of 0.7 every device generation. As devices continue to shrink the individual components become more susceptible to surface or interface atomic defects, as the surface atoms are a larger percentage of the whole device, the interface electronic structure quickly becomes the electronic structure of the whole device. Atomic defects in the surface of a device or at the interface can, for example, change the wavelength of light emitted by a quantum dot,[23-26] or alter the charge carrier transport characteristics in carbon nanotube based transistors.[27-28] Understanding how atomic defects in these low-dimensional systems modify the local density of states is essential for future applications.

1.3. Overview of Dissertation

The research described within this dissertation details experiments performed on systems using STM, with the goal of improving our understanding of how atomic defects affect the local electronic structure of low-dimensional systems, culminating in a study of how defects in a monolayer of a dielectric affect the electronic structure of a carbon nanotube.

Chapter I provides a brief background of STM, discusses the motivation of the dissertation, and contains this dissertation outline. Chapter II provides the basic theoretical background of the tunneling phenomenon and the theoretical underpinning of both scanning tunneling microscopy and the various forms of scanning tunneling spectroscopy.

The first low-dimensional system studied was zero-dimensional colloidal silicon nanocrystal quantum dots. Which are challenging to study with a STM, due to their complex three dimensional structure, and their weak stability on metallic substrates,[29] which is further complicated by substrate cleanliness concerns from the in-vacuum pulse valve method used to deposit the nanocrystals.[30] These results are described in Chapter III, which was previously published under the title "Mapping of Defects in Individual Silicon Nanocrystals Using Real-Space Spectroscopy" in The Journal of Physical Chemistry Letters, co-authored by Dmitry A. Kislitsyn, Vancho Kocevski, Jon M. Mills, Sheng-Kuei Chiu,

Christian F. Gervasi, Benjamen N. Taber, Ariel E. Rosenfield, Olle Eriksson, Ján Rusz, Andrea M. Goforth, and George V. Nazin; Chapter IV, which was previously published under the title "Communication: Visualization and spectroscopy of defects induced by dehydrogenation in individual silicon nanocrystals" in The Journal of Chemical Physics, co-authored by Dmitry A. Kislitsyn, Jon M. Mills, Vancho Kocevski, Sheng-Kuei Chiu, William J. I. DeBenedetti, Christian F. Gervasi, Benjamen N. Taber, Ariel E. Rosenfield, Olle Eriksson, Ján Rusz, Andrea M. Goforth, and George V. Nazin. Chapter V, which was previously published under the title "Creation and Annihilation of Charge Traps in Silicon Nanocrystals: Experimental Visualization and Spectroscopy" in The Journal of Physical Chemistry Letters, co-authored by Dmitry A. Kislitsyn, Jon M. Mills, Sheng-Kuei Chiu, Benjamen N. Taber, James D. Barnes, Christian F. Gervasi, Andrea M. Goforth, and George V. Nazin.

The second system, chapter VI is based upon an article being prepared for submission, co-authored with Benjamin W. McDowell, Motoaki Honda, and George V. Nazin, where we use STM/STS and density functional theory (DFT) to study a sub-monolayer of a novel insulating material, rubidium iodide (RbI), deposited onto the Ag(111) surface. An ultrathin insulating film is capable of decoupling the electronic states of an adsorbate from the metal states of the substrate,[15] allowing the STM to probe the intrinsic electronic properties of the individual adsorbates of interest. We identified and characterized two

5

unique single-layer structures of RbI, which are structurally distinct from the bulk crystal, and which differ in their coordination both within the adlayer and to the substrate surface. The coexistence of trigonal and square RbI phases, suggests a preference for the adlayer to undergo surface reconstruction rather than form a second layer. We attribute this result to stabilizing charge redistribution effects, which are maximized in a single-layered structure. These results represent key insights into the growth of exotic thin film structures. Chapter VII is based upon an article prepared for submission, co-authored with Benjamin W. McDowell, Motoaki Honda, Benjamen N. Taber, Christian F. Gervasi, and George V. Nazin, where we use STM/STS and density functional theory (DFT) to study atomic scale defects and phase boundary defects in a sub-monolayer of RbI deposited onto the Ag(111) and the Au(111) – (22 × √3) surface, we also explore the impact of environmental electrostatic perturbations on the local density of states (LDOS) single-walled carbon nanotube (CNT). CNTs adsorbed on a metal, Au(111), and a dielectric, monolayer RbI on Au(111), serve as models for strong and weak electrostatic interactions, respectively. In both cases, STS revealed modulations in the CNT LDOS corresponding to features in the underlying material.

Chapter VIII details the design, and construction of a new pan style STM scanner assembly, magnetic STM tip holders, and the redesign of the modules inside the UHV chamber necessary to accommodate the

new magnetic STM tip holders. This design reduces the possibilities for applying any external lateral force to the piezo-electric ceramic cylinder scan tube, thereby reducing the possibility of accidently breaking the STM (something I have personal experience with). During the scanner assembly upgrade a number of design and construction choices were made specifically to reduce electromagnetic or radio frequency interference, these choices are detailed in chapter VIII.

References are located at the very end of this dissertation, they are organized by chapter and are cited anew in each chapter they appear for simplicity.

CHAPTER II

SCANNING TUNNELING MICROSCOPY: PRINCIPLE AND INSTRUMENTATION

2.1. Theory of Tunneling

The STM is based upon the quantum mechanical principle of electrons tunneling through a potential barrier.[1-2] In layman's terms, quantum tunneling is when a particle with energy less than a potential barrier penetrates the side of the barrier non-destructively, passes through the barrier, and exits the other side with the same energy it entered the barrier with. Obviously, this phenomenon is not observed in the macroscopic world, as anyone who has ever bounced a ball off a wall can attest to.
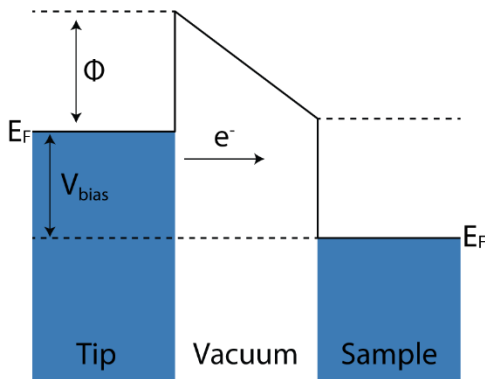
Figure 2.1. Principle of STM imaging. At cryogenic temperatures, all states below the Fermi levels (E_F) of the tip and sample, respectively, are occupied. By applying a bias voltage (V_{bias}) to the STM junction electrons tunnel from an occupied state near the Fermi level of the tip into an empty state of the sample (or vice versa). For simplicity, it is assumed that the work function Φ is the same for tip and sample.

Even very high velocity high energy macroscopic objects are unable to tunnel through a barrier, otherwise the humble sandbag would be unable to provide ballistic protection. The basic concept of quantum tunneling is illustrated is figure 2.1.

In quantum mechanics a particle (in this case an electron) is described by a wavefunction $\psi(z)$ that satisfies the Schrödinger equation,[3]

$$-\left(\frac{\hbar^2}{2m}\frac{d^2}{dz^2} + V(z)\right)\psi(z) = E\psi(z), \qquad \text{(Equation 2.1)}$$

where E is the total energy of the particle, $V(z)$ is the one-dimensional time-independent potential, m is the mass of the particle, and $\hbar$ is the reduced Planck constant. To solve the Schrödinger equation the potential $V(z)$ and the boundary conditions must be specified. The simplest situation is when the potential $V(z)$ is zero and there are no boundary conditions, thus when $E > V(z)$, the Schrödinger equation becomes,

$$-\frac{\hbar^2}{2m}\frac{d^2\psi(z)}{dz^2} = E\psi(z) \Rightarrow \left(\frac{d^2}{dz^2} + k^2\right)\psi(z) = 0 \qquad \text{(Equation 2.2)}$$

with k the wave number being,

$$k^2 = \frac{2mE}{\hbar^2}. \qquad \text{(Equation 2.3)}$$

The general solution is then a combination of the two independent plane waves, $\psi_+(z)$ and $\psi_-(z)$, with $\psi_\pm(z) = e^{\pm ikz}$. The complete wave function is then,

$$\psi_k(z) = Ae^{ikz} + Be^{-ikz} \qquad \text{(Equation 2.4)}$$

9

where A and B are arbitrary constants, the intensities of the waves given by $|A|^2$ and $|B|^2$ respectively. Ae^{ikz} represents a wave traveling in the positive z direction, and Be^{-ikz} represents a wave traveling in the negative z direction (if instead of being in the Z plane we were working in the X plane Ae^{ikx} represents traveling to the right and Be^{-ikx} represents traveling to the left).

If we introduce a potential barrier,

$$V(z) = \begin{cases} 0, & x < 0, \\ V_0, & 0 \le x \le a, \\ 0, & x > a. \end{cases} \qquad \text{(Equation 2.5)}$$

as illustrated in figure 2.2 this is analogous to the tip-vacuum-sample environment a STM operates in. We can equate the tip to the $x < 0$ region, the sample to the $x > a$ region, and the vacuum to the $0 \le x \le a$ region with a potential barrier. The general solutions for this are as follows,

$$\psi(z) = \begin{cases} \psi_1(z) = Ae^{ik_1z} + Be^{-ik_1z}, & x \le 0, \\ \psi_2(z) = Ce^{ik_2z} + De^{-ik_2z}, & 0 \le x \le a, \\ \psi_3(z) = Fe^{ik_1z}, & x \ge a. \end{cases} \qquad \text{(Equation 2.6)}$$

where the wave number has two forms depending on

$$k_1^2 = \frac{2mE}{\hbar^2}, k_2^2 = \frac{2m(E - V_0)}{\hbar^2} = \frac{-2m(V_0 - E)}{\hbar^2}.$$

In the $x \le 0$ region, even when E is much much greater that V_0 there is still some probability the incoming particle will be reflected, to reuse the bullet analogy, in quantum mechanics there is always a small probability a piece of Tenjugo (the thinnest paper in the world) will reflect a bullet.

Note that in the regime of interest, where $E < V_0$ k_2 is imaginary and thus $\psi_2(z)$ can be written as $Ce^{k_2 z} + De^{-k_2 z}$. The tunneling probability T is,

$$T = \frac{FF^*}{AA^*} \qquad \text{(Equation 2.7)}$$

After calculating F in terms of A, the transmission probability can be expressed as,

$$T = \left[1 + \frac{1}{4}\left(\frac{k_1^2 + k_2^2}{k_1 k_2}\right)^2 \sinh^2(k_2 a) \right]^{-1}. \qquad \text{(Equation 2.8)}$$

As the width a of the potential barrier is finite the wavefunction on the other end of the barrier is finite, and therefore a transmitted wave exists, showing that an electron has a small but finite probability of tunneling through the vacuum barrier of the STM junction. Now that I have shown that tunneling does take place, I will describe the theoretical model describing experimental results of an STM.
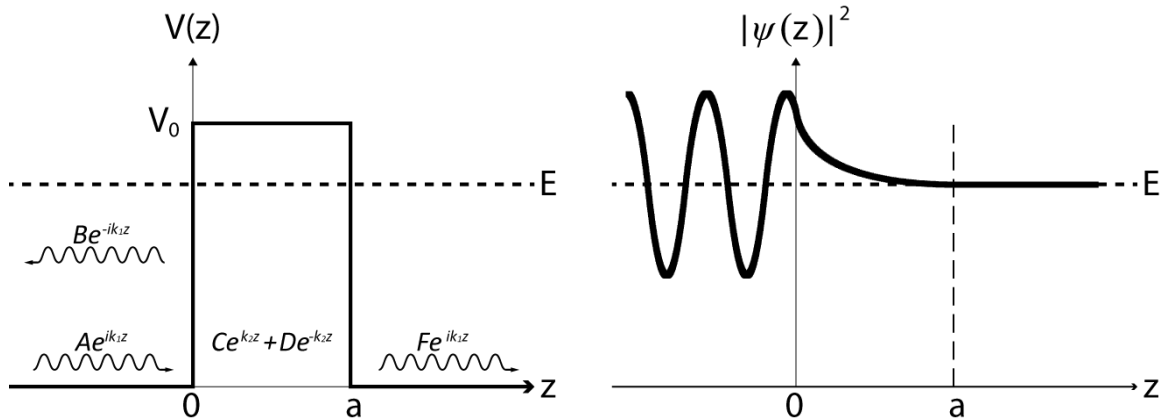
Figure 2.2. Potential barrier, wave propagation direction, and probability density $|\psi(z)|^2$ for when $E < V_0$.

2.2. Principles of Scanning Tunneling Microscopy

The models of imaging and spectroscopy with an STM are by necessity complex,[4] as tunneling is a three-dimensional phenomenon. For the sake of simplicity, I will use the theory of tunneling as proposed by Bardeen,[5] and as applied to the STM by Tersoff and Hammann.[6-7] In this framework, the tip and the sample are two separate systems, separate local density of states (LDOS), separate wavefunctions that fall exponentially to zero within the tunneling barrier and therefor only slightly overlap (when the tip and sample are separated by anything more than a few nanometers), and therefore each is only slightly influenced by the tail of the wavefunction from the other.

Using time-dependent perturbation theory the current flowing from the tip to the sample (or vice versa depending upon the sign of the bias voltage) can be calculated. If we bias the sample with positive voltage, this is basically lowering the Fermi level of the sample as compared to the tip (See Figure 2.1), and so electrons will flow from the occupied states near the Fermi level of the tip into an empty state of the sample. Assuming the tunneling process is elastic (energy is conserved), meaning that electrons are tunneling from states then into states with the same energy, the tunneling current (I) depends upon the LDOS of the tip and the LDOS of the sample, and the tunneling current from the tip to the sample for states of energy ε relative to the Fermi level of the sample is,[2]

$$I_{tip \to sample} = 2e\frac{2\pi}{\hbar}|M|^2 \left(\rho_t(E_t)f(E_t)\right)\left(\rho_s(E_s)[1-f(E_s)]\right) \qquad \text{(Equation 2.9)}$$

where e is the charge on an electron, the leading 2 is for spin, $|M|$ is the matrix element for tunneling, $\rho_s(\varepsilon)$ is the density of states of the sample, $\rho_t(\varepsilon)$ is the density of states of the tip, $f(\varepsilon)$ is the Fermi-Dirac distribution function,

$$f(\varepsilon) = \frac{1}{1 + e^{\frac{E-E_F}{k_B T}}} \qquad \text{(Equation 2.10)}$$

k_B is Boltzmann's constant, and T is the temperature in Kelvin. The overwhelming number of electrons for positive sample voltage will be tunneling from tip to the sample, however there will be a finite number of electrons tunneling from the sample to the tip and so the current flowing from the sample to the tip expression is,

$$I_{sample \to tip} = 2e\frac{2\pi}{\hbar}|M|^2 \left(\rho_s(E_s)f(E_s)\right)\left(\rho_t(E_t)[1 - f(E_s)]\right). \text{(Equation 2.11)}$$

After summing the two currents, and integrating over all energies ε, the tunneling current becomes,

$$I = I_{tip \to sample} - I_{sample \to tip}$$
$$= \frac{4\pi e}{\hbar}\int_{-\infty}^{\infty} |M|^2 \rho_t(E_t)\rho_s(E_s)\{f(E_s)[1 - f(E_t)] - f(E_t)[1 - f(E_s)]\}\, d\varepsilon\,. \text{(Equation 2.12)}$$

The equation can be further simplified, as we are assuming that the tunneling is elastic E_s and E_t are states with equal energy. If the states are written with respect to their Fermi energies (E_F) and E_F is set to zero as experiments occur at cryogenic temperatures, then $E_s = \varepsilon - eV$ and $E_t = \epsilon$ as we have separated the states due to the applied sample bias voltage V. Thus, making the current,

$$I = I_{tip \to sample} - I_{sample \to tip}$$

$$= \frac{4\pi e}{\hbar} \int_{-\infty}^{\infty} |M|^2 \rho_t(\varepsilon)\rho_s(\varepsilon - eV)[f(\varepsilon - eV) - f(\varepsilon)] \, d\varepsilon.. \qquad \text{(Equation 2.13)}$$

At very low temperatures the Fermi-Dirac distribution function is
basically a step function with a cutoff width of $k_B T$, using T=22 K (the
sample temperature used in this work, the cutoff width is 1.89 meV.
Much smaller than the energy resolution required for the measurements.
Additionally, the integral can be broken into three separate parts, $-\infty <
\epsilon < 0$, $0 < \epsilon < eV$, and $eV < \epsilon < \infty$. When we bias the sample with positive
voltage the only relevant portion of the integral is $0 < \epsilon < eV$, and the
tunneling current can be approximated as,

$$I \approx \frac{4\pi e}{\hbar} \int_0^{eV} |M|^2 \rho_t(\varepsilon)\rho_s(\varepsilon - eV) \, d\varepsilon. \qquad \text{(Equation 2.14)}$$

At this point, current is a combination of the LDOS of the sample and the
tip, weighted by $|M|^2$. So, what is $|M|^2$ and is it possible to simplify this
equation even further? $|M|^2$ is Bardeen's,[5] tunneling matrix element
between states in the tip and states in the sample,[2]

$$M = \frac{\hbar^2}{2m} \int_{z=z_0} \left[\chi^* \frac{\partial \psi}{\partial z} - \psi \frac{\partial \chi^*}{\partial z} \right] dS, \qquad \text{(Equation 2.15)}$$

where χ^* and ψ are the wavefunctions for the tip and the sample,
respectively. The integral is over the surface within the vacuum between
the tip and the sample. If we assume that the potential barrier is square,
and use a Jeffreys-Wentzel–Kramers–Brillouin approximation, $|M|^2$ can
be written as,

$$|M|^2 \approx e^{-2\int_0^s \sqrt{\frac{2m\varphi}{\hbar^2}}\,dx} = e^{-2\frac{s}{\hbar}\sqrt{2m\varphi}} = e^{-s\sqrt{\frac{8m\varphi}{\hbar^2}}}, \qquad \text{(Equation 2.16)}$$

where s is the width of the barrier (vacuum), m is the mass of the

electron, and φ is the height of the barrier.[8] The barrier height is the

work function of the tip convoluted with the work function of the sample

and is usually on the order of 5 eV or more, for example the work

function of the Au(111) surface is 5.31 eV,[9] and for polycrystalline silver

(the material used for the STM tips in this work) the work function is

4.26 eV.[9] The tunneling current can be written as,

$$I \approx \frac{4\pi e}{\hbar} e^{-s\sqrt{\frac{8m\varphi}{\hbar^2}}} \int_0^{eV} \rho_t(\varepsilon)\rho_s(\varepsilon - eV)\,d\varepsilon. \qquad \text{(Equation 2.17)}$$

As $\frac{4\pi e}{\hbar}$ is a constant, and $e^{-s\sqrt{\frac{8m\varphi}{\hbar^2}}}$ does not change appreciably over the

energy interval of interest ($0 < \epsilon < eV$), the tunneling current is really only

dependent upon the convolution of the LDOS of the tip and the sample,[2]

$$I \propto \int_0^{eV} \rho_t(\varepsilon)\rho_s(\varepsilon - eV)\,d\varepsilon. \qquad \text{(Equation 2.18)}$$

2.3. Scanning Tunneling Microscopy Measurements

2.3.1 Topography

Now that I have shown the approximate current flow between the

tip and the sample, I will describe the several operating modes for the

STM. Arguably, the most used STM mode is the constant current scan

mode. Where a feedback loop is used to maintain a constant current

while the tip raster scans. The position of the tip is recorded, and a

topographic map of the sample surface is plotted. The ability of the STM

to maintain a constant current by changing the distance between the tip and the sample is found in equation 2.17, specifically in the tunneling matrix element,

$$|M|^2 \approx e^{-s\sqrt{\frac{8m\varphi}{\hbar^2}}}. \qquad \text{(Equation 2.19)}$$

In equation 2.17 the factor s is the only factor directly tied to the tip-sample distance Z, if we assume that φ is $5\ eV$ and that the bias voltage V is much less than φ, the square root in Equation 2.19 reduces to $e^{-s*(2.05\ \text{Å}^{-1})}$ and the current will vary by approximately 9.9 per ångström. This extreme sensitivity to tip-sample separation distance is the source of the sub angstrom vertical resolution possible with STM.

2.3.2. Spectroscopy

From equation 2.17 there are three interconnected parameters that are important, the bias voltage V, the tunneling current I, and the tip-sample distance Z. Scanning tunneling spectroscopy (STS) fixes one of the three parameters to determine the dependence of the other two parameters. The three modes of spectroscopy are: $I(Z)$ where current is measured as a function of tip-sample separation distance and voltage is held constant, $Z(V)$ where tip-sample separation distance is measured as a function of voltage and current is held constant, and $I(V)$ where current is measured as a function of voltage and tip-sample separation distance is held constant.

From $I(Z)$ measurements it is possible to determine the convoluted work function for the tip-sample system. The dependance of s and the square root of the work function in equation 2.19 allows us to plot $\log I$ vs s and the slope is the work function,[10-11]

$$\varphi[eV] = \frac{\hbar^2}{8m}\left(\frac{d \ln I}{ds}\right)^2 = 0.95 \left(\frac{d \ln I}{ds[\text{Å}]}\right)^2 . \qquad \text{(Equation 2.20)}$$

Surprisingly $Z(V)$ measurements have been used to study electronic states of the sample above the vacuum level of the system, in the regime where field emission occurs (bias voltages larger than the work function of the tip).[12] $I(V)$ is the most commonly used spectroscopic technique in the STM community, it allows the researcher to obtain detailed information on the LDOS of the sample on the same scale as the topography information. In STS measurements the STM is attempting to probe the sample LDOS only without any influence from the tip LDOS. Unfortunately, equation 2.13 shows that in addition to the tip LDOS several other factors must be known in order to determine the sample LDOS from the tunneling current. During STS measurements the tip-sample distance is fixed, thus allowing us to consider the tunneling matrix element as a constant, and a small sample bias is used, making equation 2.18,

$$I \approx I_0 \int_0^{eV} \rho_t(\varepsilon)\rho_s(\varepsilon - eV)\, d\varepsilon. \qquad \text{(Equation 2.21)}$$

If the tip material is carefully chosen so that there is a flat DOS around the energy range we are interested in $\rho_t(\varepsilon)$ can be approximated as a constant $\rho_t(0)$, giving the tunneling current equation the form,

$$I \approx I_0\, \rho_t(0) \int_0^{eV} \rho_s(\varepsilon - eV)\, d\varepsilon \Rightarrow I \propto \int_0^{eV} \rho_s(\varepsilon - eV)\, d\varepsilon, \qquad \text{(Equation 2.22)}$$

allowing us to measure the integral of the LDOS (specifically empty states as we are using positive bias voltage V) of the sample from the Fermi level up to any energy $E = eV$. We however do not want the integrated local density of states we want the LDOS itself. There are a number of ways we could accomplish this, the most straight forward is once we obtain the integrated LDOS vs. V data we take a numerical derivative $\left(\frac{dI}{dV}\right)$, this would directly measure the LDOS,[6-7] however a numerical derivative is very noisy. A better method would be to somehow measure the derivative directly.

By fixing the tip-sample distance and using a lock-in amplifier to apply a sample bias voltage with a small high frequency sinusoidal modulation dV around V we can measure the first harmonic frequency which is directly proportional to $\frac{dI}{dV}$. In short, because we are modulating V at a set frequency we can measure an AC current modulation at the same frequency. The $\frac{dI}{dV}$ is sometimes called the conductance $g(V)$, and $g(V) = \frac{dI}{dV} \propto LDOS(eV)$.[2] It should be noted that the STM community will use $\frac{dI}{dV}$, STS, and LDOS spectroscopy interchangeably, the majority of

modern STMs use a lock-in amplifier to measure the conductance and as such the terms have become colloquialisms.

2.3.3. Differential Conductance Mapping

An extension of STS measurements is differential conductance mapping (LDOS maps), where rather than measure the $\frac{dI}{dV}$ at a single point we measure it at a series of points. There are two different types of LDOS maps we utilize, the first is where we take a sequence of STS spectra at regular spaces along a 1-D line (i.e. a 64 pixel linescan), the second is where we extend the line into a 2-D map with the same number of points in both directions (i.e. a 64 × 64 pixel grid). The general procedure is the tip is moved point-to-point with the feedback on (constant current mode), the feedback is disabled and a STS spectra is taken, then the feedback is re-engaged and the tip is moved to the next point, and so on. The data collected can be viewed as 3-D data sets and are a great way to visualize the LDOS in real space.

The downside to collecting LDOS maps is the time required. Assuming we want a spatial resolution of one pixel per 5 Å, a 500 Å square would require a 128 × 128 pixel grid, assuming we want 101 energy measurements per pixel, that is 1.65×10^6 total measurements, if each measurement only takes 100 milliseconds, a single map would require almost 46 hours. Note that this does not consider the time required for the DC voltage to change to each of the 101 values, the AC bias modulation to switch to the new voltage, the lock-in amplifier to lock

into the new *dI*, and the time for everything to stabilize. A more typical LDOS map is at usually a 64 × 64 pixel grid, and is at most 41 measurements at each pixel, which still takes around 17 hours (~15 seconds per pixel).

2.4. Scanning Tunneling Microscopy Instrumentation

All of the experiments presented in this dissertation were taken were carried out in a home-built ultra-high vacuum (UHV) cryogenic STM system.[13] All of the measurements were performed at temperatures between 22 and 36 K using electrochemically etched polycrystalline silver tips.

2.5. Bridge to Chapter III

In the following chapters the elementary principles of quantum tunneling as applied to STM will be applied to study several classes of low dimensional materials, and specifically atomic scale defects within those materials. The first system studied will be solution-processable silicon nanocrystals (SiNC) which are an extremely attractive material due to their non-toxicity, the maturity of silicon-based technologies, combined with the flexibility that manipulation of nanoscale properties offers.[14-16] One of the obstacles to incorporating SiNCs into devices lies with a lack of knowledge of the interplay between surface- and core-related effects on the NC electronic structure.[17-18] We will use scanning tunneling spectroscopy to study the impact of surface defects on the electronic structure of the SiNCs.

CHAPTER III

MAPPING OF DEFECTS IN INDIVIDUAL SILICON NANOCRYSTALS USING REAL-SPACE SPECTROSCOPY

From Kislitsyn, D. A.; Kocevski, V.; Mills, J. M.; Chiu, S. K.; Gervasi, C. F.; Taber, B. N.; Rosenfield, A. E.; Eriksson, O.; Rusz, J.; Goforth, A. M.; Nazin, G. V. Mapping of Defects in Individual Silicon Nanocrystals Using Real-Space Spectroscopy. *J. Phys. Chem. Lett.* **2016**, *7* (6), 1047.

3.1. Introduction

The photophysical properties of silicon semiconductor nanocrystals (SiNCs) are extremely sensitive to the presence of surface chemical defects, many of which are easily produced by oxidation in ambient conditions. The diversity of chemical structures of such defects, and the lack of tools capable of probing individual defects continue to impede understanding of the roles of these defects in SiNC photophysics. In this letter, we use scanning tunneling spectroscopy to study the impact of surface defects on the electronic structures of hydrogen-passivated SiNCs supported on the Au(111) surface. Spatial maps of the local electronic density of states (LDOS) produced by our measurements allowed us to identify locally-enhanced defect-induced states as well as quantum-confined states delocalized throughout the SiNC volume. We

use theoretical calculations to show that the LDOS spectra associated with the observed defects are attributable to Si–O–Si bridged oxygen or Si–OH surface defects.

3.2. Background

Silicon semiconductor nanocrystals (NCs) have recently emerged as a promising alternative to metal chalcogenide-based quantum dots (QDs) in a wide range of photophysical applications including light-emitting devices[1-2] and photovoltaics,[3-6] as well as in biomedical imaging and tracking.[7-8] Among the advantages of SiNCs are the lower toxicity of silicon and the potential for a more robust covalent passivation of SiNC surfaces.[9-10] For sufficiently small SiNCs, the indirect electronic bandgap of silicon, responsible for the inefficient coupling to light in larger NCs, becomes ill-defined,[11-13] which leads to a dramatic brightening of radiative transitions,[14-17] and thus enables optical and optoelectronic applications of SiNCs. Further, multiple exciton generation in ultra-small SiNCs has been considered as a potential route for increasing the efficiency of photovoltaic devices.[18-20] While beneficial for applications, the ultra-small size of SiNCs makes them extremely susceptible to the chemical structure of the NC surface. In particular, the tendency of SiNC surfaces to oxidize,[21-22] resulting in pronounced changes in optical properties, has been a major challenge not only for applications based on SiNCs, but also for the basic understanding of SiNC photophysics. The presence of oxidative defects on the SiNCs surface has been shown to

produce red-shifted photoluminescence (PL), with photon energies being considerably less sensitive to the SiNC size than predicted for emission from quantum-confined states.[23-28] The exact origin of this emission remains poorly understood, which is due, in part, to the diversity of chemical defects resulting from surface oxidation of silicon,[26, 29] and the lack of experimental techniques capable of directly identifying the chemical structures of defects responsible for the red-shifted PL. Theoretical studies suggest that Si–O–Si bridged oxygen,[30-32] as well as sufficient coverage of Si–OH surface groups may result in red-shifted PL.[13, 33] Indeed, it would be natural to expect these defects to play a role in PL of SiNCs, since both defects appear prominently in Fourier transform infrared spectroscopy (FTIR) of porous hydrogen-passivated SiNCs within minutes of exposure to ambient air.[23] Alternatively, a red shift consistent with the experimental data may be attributed to emission from individual defects associated with surface silicon-oxygen double (Si=O) bonds,[23, 30-32, 34-36] which have not, however, been observed in FTIR spectra of emissive SiNCs. Finally, completely oxidized SiNCs have also been shown to possess delocalized electronic states with calculated energies consistent with the experimentally observed PL.[37] The plurality of theoretical models explaining the origin of red-shifted emission highlights the need for experimental studies that could directly identify the chemical nature and electronic structures of individual defects in individual SiNCs. This capability is offered by scanning tunneling

spectroscopy (STS),[38] which has been used to study quantum confinement effects in individual SiNCs,[39] as well as localization of individual sub-bandgap states in PbS nanocrystals.[40-41]

3.3. Methods

Experiments were carried out in a home-built ultra-high vacuum (UHV) cryogenic STM system.[42] A Au(111)/mica substrate was prepared in situ using multiple neon sputter/anneal cycles. Hydrogen-passivated SiNCs were fabricated via thermal disproportionation in a polymeric sol–gel hydrosilicate precursor, and subsequently liberated from the resulting oxide host matrix via a wet chemical etch (i.e., with HF/EtOH/H2O) using a protocol described previously[43] (for further details see Appendix A). The SiNCs were suspended in pentane, and deposited onto the Au(111) surface in high-vacuum conditions using a solenoid pulse-valve. The deposition parameters were chosen so as to obtain monolayer NC coverage. The Au(111) substrate with deposited SiNCs was then degassed overnight in UHV at ~50 °C to remove any residual pentane from the sample surface. All STM topographies and STS measurements were obtained at a temperature of ~20 K using silver tips prepared by electrochemical etching and subsequent sputtering in UHV. All STS spectra were recorded using the lock-in technique at 570 Hz and a bias modulations varying from 10 (individual spectra and 1-D spatial scans) to 50 mV (2-D LDOS maps). 2D LDOS mapping requires tip-sample spatial registry throughout the mapping process (typically,

several hours). This capability is enabled by the unique spatial stability (better than ~0.2 Å/hour) of our STM system.[42]

Theoretical calculations were performed using DFT, as implemented in the pseudo-potential package SIESTA,[44-45] employing local density approximation (LDA) exchange and Ceperlay-Alder parameterization of the potential, as described previously.[32] Numerical atomic orbitals were used as a basis set: "single zeta with polarization" orbitals for Si and O, and "double zeta" for H. Further details of the basis sets for different elements are given in Ref. 12. For hydrogenated SiNCs smaller than 4 nm in diameter, the described approach provides a good approximation of electronic bandgaps.[12]

To simulate the experimental data, LDOS was calculated as probability density sum $LDOS(x, y, z, V) = \sum_j |\Psi_j(x, y, z)|^2 \delta(eV - E_j)$ of individual Kohn-Sham orbitals $\Psi_j(x, y, z)$ obtained from DFT. To account for finite spatial and spectral resolution of the experimental data, the contributions of individual orbitals to the total LDOS were Gaussian-broadened by 50 meV in energy, and by 0.2 nm in space. To more closely reproduce experimental conditions where the integral of each dI/dV spectrum is equal to the setpoint current, calculated LDOS spectra for each specific spatial location were normalized such as to yield integrals $I(x, y, z)$ equal to the setpoint value I_{sp}:

$$I_{sp} = I(x, y, z) = \int_0^{V_B} LDOS(x, y, z, V)\, dV \qquad (Equation\ 3.1)$$

Here $I(x, y, z)$ represents the calculated tunneling current in each spatial location, and V_B is the setpoint bias voltage (noted in the corresponding figure captions).

3.4. Results and Discussion

Here we report, for the first time, studies of defect-induced electronic states on the surfaces of individual hydrogen-terminated SiNCs using spatially–resolved STS mapping. Hydrogen-terminated SiNCs were spray-deposited onto a Au(111) substrate in vacuum and studied using an ultra-high vacuum (UHV) cryogenic scanning tunneling microscope (STM) system[42] (see Methods for further experimental details). In STM images, SiNCs deposited on Au(111) surfaces appeared as protrusions with typical dimensions in the 2-4 nm range (Figures 3.1a and 3.3a). Using STS we recorded energy-dependent local density of states (LDOS) spectra of individual SiNCs by measuring the differential tunneling conductance (dI/dV) as a function of the applied bias voltage (see Methods for details of the measurements). We focus our attention on the electronic states in the vicinity of the bandgap, since these are the states that are primarily responsible for the photophysical and electron transport properties of individual NCs and NC-based materials. In the following, we summarize our STS studies of 27 individual SiNCs.

Individual LDOS spectra measured on different SiNCs showed similar progressions of electronic states, comparable to the theoretically predicted progressions of states for hydrogen–passivated SiNCs with

similar diameters (Figure A.1). All SiNCs studied could be roughly divided into two classes: nominally "defect-free" SiNCs, which showed electronic states delocalized over the whole NC surface, and nominally "defect-containing" SiNCs exhibiting electronic states with LDOS strongly enhanced at specific locations. LDOS spectra of each "defect-free" SiNC contained a nearly identical set of electronic peaks H_n (occupied states) and E_n (unoccupied states) across the whole NC surface, as shown in Figures A.2 and 3.1a-c for one representative SiNC (NC_1 in the following). The relative intensities of electronic peaks H_n and E_n depend on the specific spatial location, as visualized in Figure 3.1b, which shows an array of LDOS spectra recorded along the line shown in Figure 3.1.

Intriguingly, the LDOS spectra (and intensities of electronic peaks) are nearly identical within specific regions on the NC_1 surface (regions R_1-R_3 in Figure 3.1b, representative LDOS spectra for each region are shown in Figure 3.1c), and change on the angstrom scale at the boundaries between the regions, a behavior that was also observed for other "defect-free" SiNCs (data not shown). To further explore the nature of peaks H_n and E_n, we recorded two-dimensional (2D) spatial LDOS maps showing the distribution of each electronic state across the NC_1 surface (Figures 3.1e-j). To ensure that we could identify all of the
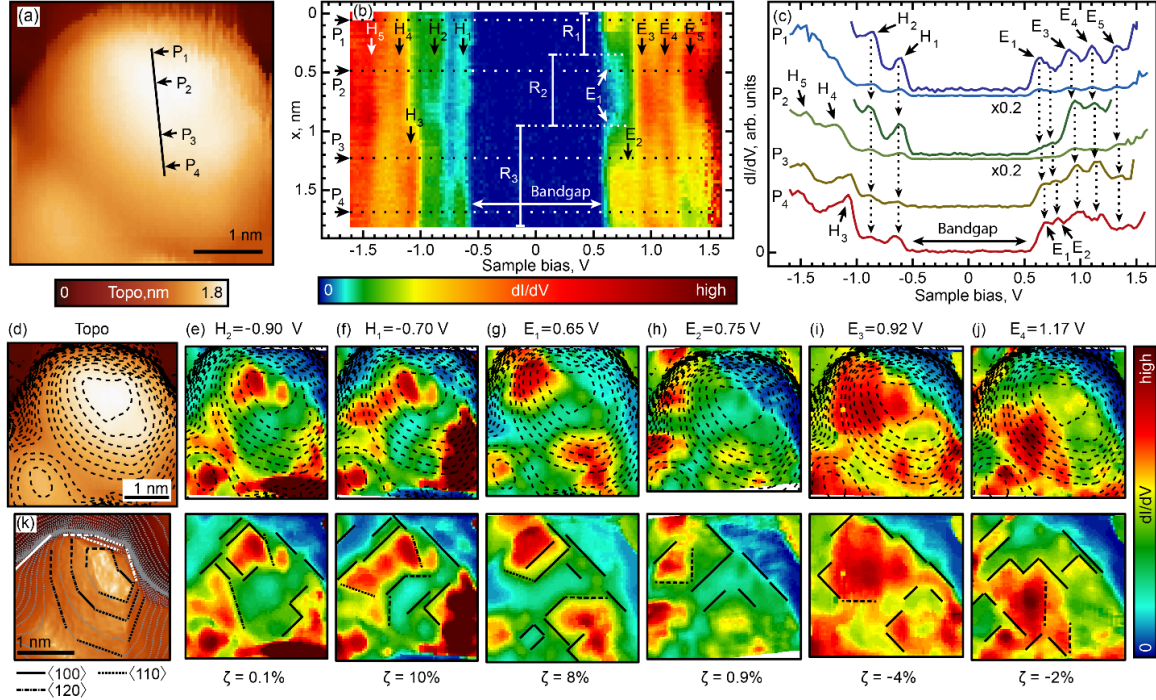
Figure 3.1. Spatial mapping of LDOS for NC_1. (a) STM topographic image. (b) LDOS (measured as dI/dV) as a function of the bias voltage and position x along the path shown in (a). R_1-R_3 indicate regions with specific patterns of LDOS spectra. In (b), the individual unoccupied and occupied LDOS spectra were normalized separately, for clarity. (c) Individual LDOS spectra from (b) measured at points P_1 through P_4. Spectra are offset for clarity. Identical spectra for P_1 and P_2 scaled by ×0.2 are also shown. Occupied and unoccupied states are marked "H" and "E" respectively in both (b) and (c). Individual LDOS peaks are observed at slightly different voltages across the NC due to the finite location-dependent voltage drop inside the NC. (d) Topography from (a) overlaid with its contour plot. Contours correspond to vertical separation of 0.68 Å (half of one Si(100) atomic step). (e-j) 2D LDOS maps for voltages corresponding to the peaks indicated in (c). Upper row shows the LDOS maps overlaid with contour lines from (d). Lower row of LDOS maps shows Si(100) lattice directions identified in the spatial LDOS intensity distributions. Solid lines are ⟨100⟩ and ⟨010⟩ directions (perpendicular to each other), dashed lines are ⟨110⟩ and ⟨$\bar{1}$10⟩, dotted lines are ⟨210⟩ and ⟨$\bar{1}$20⟩, dash-dotted lines are ⟨120⟩ and ⟨$\bar{2}$10⟩. [Assignment of the primary directions ⟨100⟩ and ⟨010⟩ is made using the predominant orientation of linear features in the LDOS patterns.] Measure of localization ζ is calculated for every 2D map, as explained in the main text. (k) Calculated representation of NC_1 shape (see Appendix A for details) with its contour plot overlaid. Black and white lines on top of the contours correspond to Si(100) directions.

28

(possibly localized) electronic states in SiNCs, we recorded LDOS spectra on a two-dimensional grid of points covering the spatial range corresponding to Figure 3.1d. The 2D maps in Figures 3.1e-j were then generated by taking subsections of this LDOS dataset corresponding to specific energies (voltages). Thus obtained 2D LDOS maps show that the main states of NC_1 are completely delocalized (showing non-zero LDOS) on the observable part of the NC_1 surface, even though 2D-regions of varied intensities (similar to 1D-regions R_1-R_3 in Figure 3.1b) are present. Strikingly, the boundaries of these regions are aligned along specific directions attributable to a {100} crystallographic facet (bottom Figures 3.1e-j, see caption for details), an observation that was common for the majority of SiNCs studied (in addition to SiNCs showing crystallographic directions attributable to {100} facets, SiNCs showing directions consistent with {111} facets were also observed).

A crystallographic origin of directional order in the 2D LDOS maps is further supported by our analysis of the STM images of the corresponding SiNCs. In this analysis, we attempted to de-convolute the effects of STM tip-shape and finite tip-NC distance (~0.8 nm), which both lead to broadening and rounding of the apparent NC shapes observed in the STM images (see Figure A.3 for details). Thus deconvoluted images show sharply-defined facets (see Figure 3.1k for NC_1) with directions identical to those found in the LDOS maps (these directions are also present in as-recorded STM images – see Figure 3.1d), which strongly

suggests that the observed directional order in both 2D maps and recalculated STM images originates from the crystallographic structures of the SiNCs.
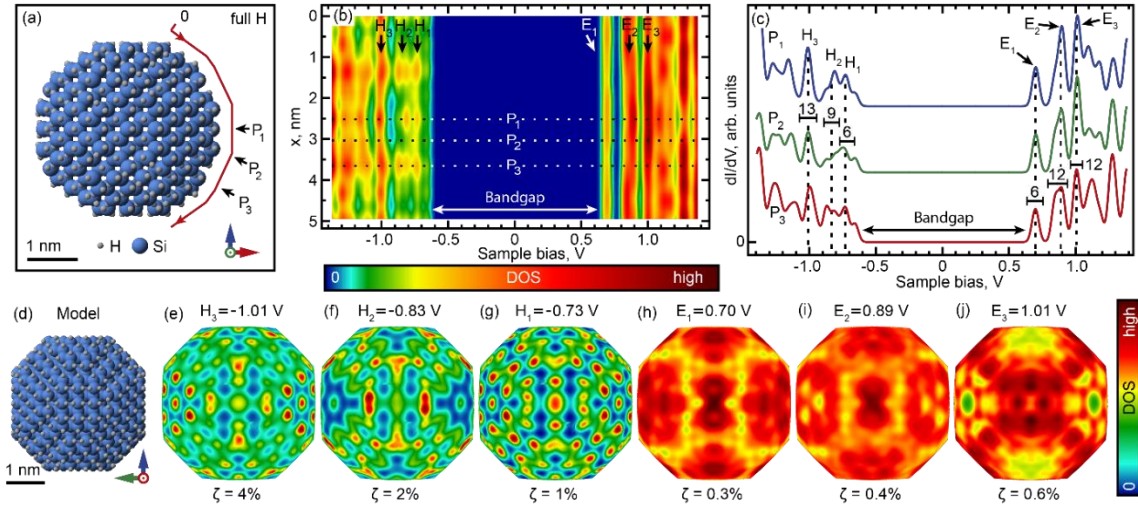
Figure 3.2. Theoretical LDOS for a model near-spherical (diameter ~3.5 nm) SiNC (with composition $H_{412}Si_{1087}$). (a) NC geometry. (b) Calculated 1D LDOS map as a function of the bias voltage and position x along the path shown in (a). (c) Individual LDOS spectra from (b) measured at points P_1 through P_3. Spectra are offset for clarity. The number of discrete states in each peak is indicated. (d) NC geometry rotated by 90° around the vertical axis and exposing facets mapped in (b) as well as in (e-j). (e-j) 2D maps of LDOS for selected states near the electronic bandgap. LDOS intensities were calculated on a 3D surface equidistantly offset from the NC surface by 3 Å, similarly to the path shown in (a). In order to more closely reproduce experimental conditions, all spectra were normalized to give the same total current at 1.35 V (see Methods for details). Measure of localization ζ is calculated for every 2D map, as explained in the main text.

The correlation with the crystallographic directions and the delocalized nature of electronic states in "defect-free" SiNCs together suggest that these states correspond to quantum-confined states delocalized throughout the bulk of NC_1 rather than defect states (the latter, in contrast, can be expected to show LDOS enhanced at the defect

30

locations). To test this hypothesis, we carried out density-functional theory (DFT) calculations (see Methods for details) for a set of model NCs of different sizes. For the simulations, we chose approximately spherical NC shapes (Figure 3.2a), as expected for SiNCs with sizes below ~6 nm.[46-47]

In agreement with the measured 2D LDOS maps, our calculations for defect-free SiNCs (see Figure 3.2 for a SiNC with a size of ~3.5 nm, similar to that of NC_1) reproduce the progressions of electronic peaks H_n and E_n observed in LDOS of studied SiNCs. We note that each peak in Figures 3.2b-c is comprised of several closely-spaced distinct electronic states formed from states associated with different electronic valleys in the Brillouin zone of bulk Si.[13] These states are not completely resolved in our measurements, even though their presence is suggested by the fine structure of LDOS spectra (Figures A.2c,d). Finer spectral structure could not be observed due to the intrinsic broadening of STS spectra associated with coupling of tunneling electrons to vibrational excitations,[48] which exceeds the inter-valley splitting for simulated SiNCs (~50 meV).

Significantly, our calculations reproduce the existence of distinct surface regions with specific LDOS spectra (Figures 3.2b-c), and the presence of directional order in the spatial LDOS distributions (Figures 3.2e-j), even though the precise spatial patterns for experimental and theoretical 2D maps are not identical. The differences in the two datasets

31

are attributable to the fact that the precise shape of NC_1, which has a profound impact on the electronic LDOS spatial distribution, is not known (since a large part of the NC_1 surface is not observable in STM imaging) and thus could not be modeled directly. The close similarity between the theoretical and experimental results in Figures 3.1 and 3.2 reinforces the interpretation of states in Figure 3.1 as those of quantum-confined nature, and delocalized in the interior of the NC, analogously to the calculated three-dimensional LDOS distributions shown in Figures A.4 and A.5.

In addition to "defect-free" SiNCs with delocalized electronic states, we have also observed SiNCs (6 out of 27 SiNCs studied in our experiments) showing localized areas with strongly enhanced LDOS. An example of this behavior is shown in Figures 3.3 and A.6 for a representative SiNC (NC_2 in the following). For example, a one-dimensional LDOS map (Figure 3.3b) of NC_2 shows peaks E_2 and H_2 delocalized over the entire spatial range of the scan, while peaks H_1^* and H_1^{**} (corresponding to a smaller bandgap) are primarily concentrated in regions R_1 and R_3, respectively. Closer inspection reveals peaks E_1 and H_1 with lower intensities everywhere along the mapping path (Figure 3.3c). The 2D LDOS maps of these electronic states (Figures 3.3e-j) give a more complete picture: states E_n and H_n of NC_2 appear over the entire observable part of NC_2, showing 2D-regions of varied intensities. Similarly to the directional order in 2D LDOS maps of NC_1, the

boundaries of some of these regions are aligned along the main crystallographic directions of NC_2 (bottom Figures 3.3e-j). Importantly, spatial distributions of several LDOS features appear very different from those of NC_1. In particular, pronounced spatially–confined maxima H_1^*, H_1^{**} and H_2^* are observed in Figures 3.3e and f, with the spatial LDOS concentration in the corresponding maps being significantly higher than that in the other maps for NC_1 and NC_2. To analyze this localization quantitatively, we implemented a comparison of average and median values for a particular LDOS map, which is sensitive to the presence of sharp intense peaks in DOS maps. We constructed a measure of localization of the form: $\zeta = \frac{\overline{DOS} - \widetilde{DOS}}{\overline{DOS} + \widetilde{DOS}} \times 100\%$ (where $\overline{DOS}$ and $\widetilde{DOS}$ are the average and median values, respectively), which for more spatially-concentrated peaks H_1^*, H_1^{**} and H_2^* gives values $\zeta \geq 20\%$ (bottom Figures 3.3e and f), while the rest of the maps shows $|\zeta| \leq 10\%$ (as listed in the respective figures), which we consider to be representative of "delocalized" states. The spatial concentration of peaks H_1^*, H_1^{**} and H_2^* suggests that they may correspond to defect-related states (because H_1^* and H_1^{**} are spatially well-separated, they likely correspond to two different defects).

To investigate the nature of observed locally-enhanced peaks H_1^* and H_1^{**}, we carried out DFT calculations of the electronic structures of SiNCs containing individual chemical defects.[32] Because a substantial fraction (~22%) of studied SiNCs showed defects of the type shown
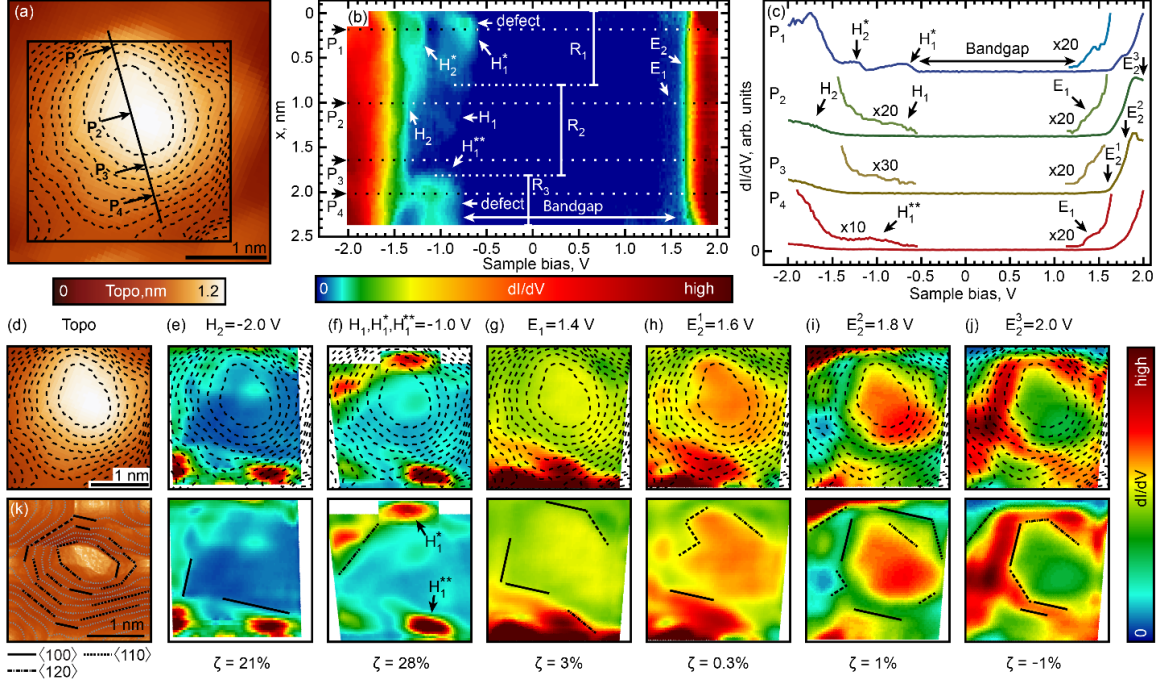
Figure 3.3. Spatial mapping of LDOS for NC_2. Data arrangement and markings are the same as in Figure 3.1. In (b), the individual unoccupied and occupied LDOS spectra were normalized separately, for clarity. Peak E_2 is measured at three voltages E_2^n.

in Figure 3.3, these are likely to be of the same chemical nature, and must be very common for the hydrogen-passivated SiNCs used in our study. Surface oxidation is particularly common for such SiNCs, and is known to produce a variety of oxygen-containing bonds on the SiNC surfaces often leading to formation of intra-gap states.[23, 30, 34] We thus restrict our consideration to elementary defects caused by oxidation, which include three main classes: Si–O–Si bridged oxygen, Si–OH groups, and Si = O bonds. For SiNCs studied in our experiments, the

34

most likely candidate is the Si–O–Si bridged oxygen defect, which is the only type of defect identifiable in the FTIR spectra of as-synthesized hydrogen-passivated SiNCs used in our study.[43, 49] Another possible candidate are the Si–OH surface groups, which have been identified in FTIR spectra of SiNCs synthesized using a similar technique.[29] However, the presence of these defects in our SiNCs may be somewhat less likely due to their instability under vacuum conditions.[50] Surface $Si = O$ defects have been implicated as a possible source of the red-shifted defect-induced PL,[23, 30, 34] and have been observed on the SiNC surfaces under vacuum conditions.[50]

Theoretical simulations of one-dimensional LDOS maps for the $Si = O$ defect on the surface of a model SiNC with a size of ~2 nm, similar to that of NC_2, show two peaks enhanced at the defect location: the highest-occupied peak H_1^* and the lowest-unoccupied peak E_1^* (Figure A.7b, see also Figures A.7g and h). Comparison of a one-dimensional LDOS map of this NC (Figure A.7b) to those of its defect-free variant (Figure A.8b), shows that the bandgap of the defective NC is reduced at the defect location by ~300 meV. However, the energy differences between the delocalized peaks H_1 and E_1 are nearly identical for both NCs, suggesting that the defect-induced peaks H_1^* and E_1^* effectively correspond to trap states within the defect-free bandgap. In contrast, bandgaps obtained from theoretical LDOS of both Si–O–Si and Si–OH defects (Figures 3.4b and A.9b, respectively) are quite similar to that of

the defect-free SiNC (Figure A.8b), consistent with previous theoretical results.[23, 30, 32, 34] The impact of these defects is primarily in the redistribution of the SiNC LDOS, resulting in enhanced LDOS at the location of the corresponding defect (compare peaks H_1 with maxima H_1^* in Figures 3.4e-g and A.9e-g to Figure A.8e-g). The varied impacts of the different types of defects on the SiNC LDOS are directly related to the specific spatial distributions of the corresponding electronic states (Figures A.10-15). Indeed, in the case of the $Si = O$ defect, the bandgap-forming states H_1^* and E_1^* are tightly localized (in three dimensions) within the immediate vicinity of the defect (Figure A.11), while the bandgap-forming states for the Si–O–Si and Si–OH defects are delocalized within the NC interiors, with only a small fraction of the total DOS found in the defect vicinity (Figures A.12-15), reminiscent of the LDOS distributions for the defect-free NC (Figures A.16-17).

Analysis of the specific spatial LDOS distributions expected for the different oxidative defects discussed above (Figures 3.4, A.7 and A.9) allows us to shed light into the nature of the defect-induced states shown in Figure 3.3. In particular, the presence of the locally–enhanced peak E_1^* in the theoretical LDOS is incompatible with the experimental LDOS for the lowest unoccupied state E_1 of NC_2 (Figure 3.3g), where only a small local maximum, instead of a strongly locally-enhanced peak is observed at the defect location corresponding to peak H_1^{**} in Figure 3.3f and no maximum is found at the location of peak H_1^* in Figure 3.3f. The

same conclusion is suggested by the fact that in Figure 3.3g, the localization parameter ζ is dramatically smaller than those found for Figure A.7h or Figure 3.3f (3% versus 32% and 28%, respectively). The absence of strong local DOS maxima in Figure 3.3g thus suggests that the Si$=$O defects are unlikely to be responsible for the locally–enhanced states observed in Figure 3.3. In contrast, we find that for the Si–O–Si and Si–OH defects, the agreement between the experimental and theoretical DOS is significantly better: the redistributions of the SiNC LDOS, resulting in enhanced occupied LDOS at the location of the corresponding defect (peaks H_1 with local maxima H_1^* in Figures 3.4 and A.9), are analogous to that found in the experimental LDOS for NC$_2$ (peak H_1 with maxima H_1^* and H_1^{**} in Figure 3.3). Further, in both experimental and theoretical data, the highest occupied states are not completely localized at the defect locations, but persist over the whole NC surface (compare, for example, Figures 3.3f to 3.4g and 3.9g). The unoccupied states in the theoretical LDOS remain relatively uniform across the NC surface, which is also consistent with the unoccupied states in the experimental LDOS of NC$_2$ (compare, for example, Figures 3.3g-j to 3.4h,j and A.9h,i). The unoccupied states in the theoretical LDOS are not significantly modified as compared to a completely hydrogen-passivated SiNC (Figure A.8, A.16 and A.17), except for some band splitting in E_2 (Figures 3.4b and A.9b), which is more noticeable for Si–O–Si, a consequence of a stronger geometric perturbation resulting

from this type of defect.[30] In addition, in the case of Si–O–Si, this splitting produces an orbital E^* concentrated around the defect (Figure 4i). This orbital, however, is not resolved in the experimental LDOS, which is likely due to the electron-vibrational band broadening effect discussed above. Significantly, the trends found for the localization parameter ζ in Figures 3.4 and A.9 are similar to those found in Figure 3.3 (we note that we do not expect the theoretical and experimental values of ζ to be in precise quantitative agreement since the corresponding NC structures and surfaces used for calculation of ζ are different). The close qualitative similarities between the theoretical and experimental LDOS suggest that the defects of the type corresponding to peaks H_1^* and H_1^{**} in Figure 3.3b may be associated with either Si–OH or Si–O–Si defects (the latter is more likely, as mentioned earlier).

Defects of the type found for NC_2 were observed only on SiNCs with relatively small diameters (less than ~2.5 nm). In contrast, nominally "defect-free" SiNCs (with electronic states delocalized) similarly to those found for NC_1 were typically larger. The lack of clearly identifiable defects on larger SiNCs does not mean that these SiNCs were entirely defect-free: our calculations show that the impact of elementary defects on the spatial LDOS patterns of such SiNCs is minimal and nearly nonexistent (for states close to the electronic bandgap) for sufficiently large SiNCs (Figure A.18), which suggests that the LDOS in Figure 3.1 may be

38

spatially modulated by defects, even though the presence of such defects could not be unequivocally established from our measurements.
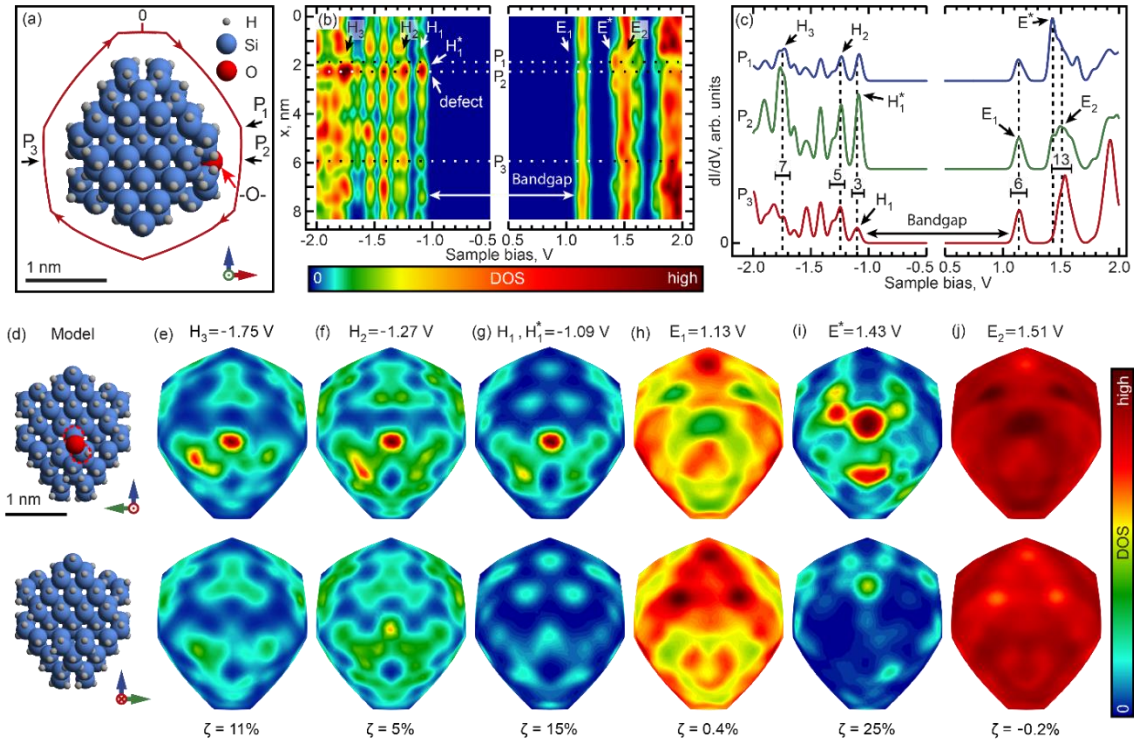
Figure 3.4. Theoretical LDOS for a model near-spherical (diameter ~2 nm) SiNC with a bridged oxygen (Si−O−Si) impurity, and composition $H_{114}Si_{175}O$. Data arrangement and markings are the same as in Figure 3.2. In (c), P_1 corresponds to the maximum of orbital E^* LDOS, P_2 corresponds to the defect location, and P_3 is positioned on the opposite side of NC with respect to P_2. The top and bottom rows in (d-j) show two opposite sides of the NC, respectively. To more closely reproduce experimental conditions, all spectra were normalized to give the same total current at 1.7 V.

3.5. Conclusions

Spatial mapping of the LDOS of individual SiNCs and theoretical calculations reported in this work show that oxidative defects spatially modulate the LDOS on SiNC surfaces producing LDOS patterns of varied

degrees of inhomogeneity that depend on the NC size. For sufficiently small SiNCs, locally-enhanced LDOS attributable to either Si–OH or Si–O–Si defects are observed in LDOS mapping and reproduced in theoretical calculations. In contrast, spatial LDOS distributions (and, consequently, the photophysical properties) of larger SiNCs are relatively insensitive to the presence of such defects. The present work was carried out using an ultra-stable closed–cycle cryogenic STM system,[42] which uniquely enables detailed STS mapping of statistically-significant quantities of individual NCs. We anticipate that further STS studies of NCs using our approach will contribute to building a more complete picture of the diverse types of defect states, in particular dangling bond defects, which are known to significantly affect the photophysical processes in SiNCs.[51-52]

3.6. Bridge to Chapter IV

In the next chapter the focus on individual atomic defects in the surface of SiNCs will shift from oxidative defects to defects caused by selectively removing individual hydrogen from the SiNC's hydrogen ligand passivation shell. We are interested in the process of dangling bond creation in individual SiNCs, and the impact of dangling bonds on the SiNCs electronic structure. We will use STS to monitor the changes in the SiNC electronic structure, which shows that the removal of hydrogen ligands causes a shrinking of the electronic bandgap, and eventually creates midgap electronic states.

CHAPTER IV

VISUALIZATION AND SPECTROSCOPY OF DEFECTS INDUCED BY DEHYDROGENATION IN INDIVIDUAL SILICON NANOCRYSTALS

From Kislitsyn, D. A.; Mills, J. M.; Kocevski, V.; Chiu, S. K.; DeBenedetti, W. J. I.; Gervasi, C. F.; Taber, B. N.; Rosenfield, A. E.; Eriksson, O.; Rusz, J.; Goforth, A. M.; Nazin, G. V. Communication: Visualization and Spectroscopy of Defects Induced by Dehydrogenation in Individual Silicon Nanocrystals. *J. Chem. Phys.* **2016**, *144* (24), 241102.

4.1. Introduction

We present results of a scanning tunneling spectroscopy (STS) study of the impact of dehydrogenation on the electronic structures of hydrogen-passivated silicon nanocrystals (SiNCs) supported on the Au(111) surface. Gradual dehydrogenation is achieved by injecting high-energy electrons into individual SiNCs, which results, initially, in reduction of the electronic bandgap, and eventually produces midgap electronic states. We use theoretical calculations to show that the STS spectra of midgap states are consistent with the presence of silicon dangling bonds, which are found in different charge states. Our

calculations also suggest that the observed initial reduction of the electronic bandgap is attributable to the SiNC surface reconstruction induced by conversion of surface dihydrides to monohydrides due to hydrogen desorption. Our results thus provide the first visualization of the SiNC electronic structure evolution induced by dehydrogenation, and provide direct evidence for the existence of diverse dangling bond states on the SiNC surfaces.

4.2. Background

Silicon nanocrystals (SiNCs) have recently attracted a great deal of attention as a promising photophysical material with applications in photovoltaics,[1-4] light-emitting devices,[5-6] and biological tagging.[7-8] SiNCs offer the advantages of low toxicity and robust surface passivation involving, for example, formation of covalent Si-C bonds.[9-10] Importantly, the optical properties of SiNCs are strongly dependent on their dimensions, with a dramatic brightening of radiative transitions observed for sufficiently small SiNCs,[11-14] a consequence of changes in the electronic structure leading to the relaxation of the momentum conservation rules known to suppress radiative transitions in bulk silicon.[15-17] While the ultra-small size of SiNCs is essential for optical applications, the resulting large surface to volume ratio means that SiNCs are very susceptible to their chemical environment and the presence of defects on their surfaces.

A wide variety of approaches for controlling the SiNC surface chemistry have been developed, including passivation with organic

molecules[18-20] as well as oxidation.[21-23] One of the most common defects found at SiNC surfaces, regardless of the surface passivation technique, is the silicon dangling bond (DB). For example, DBs exist at Si-SiO$_2$ interfaces[24-25] and at the surfaces of alkyl-passivated SiNCs.[26] DBs can also be produced by mild oxidation of hydrogenated SiNCs,[27] and by exposure to ultra-violet radiation.[28-29] DBs are known to act as non-radiative recombination centers leading to de-excitation of electronically excited states.[30] In contrast, charged DBs have been found to serve as radiative recombination centers in SiNCs with sufficiently large gap energies.[31] Further, depending on their charge and local stress, DBs at the surface of oxidized SiNCs were predicted to be capable of inducing intermittency in the SiNC photo-luminescence.[32] However, the varied impact of the different DB charge states on the SiNC photophysics, especially in the context of the different possible surface passivations, remains to be fully addressed.

While the DB-induced electronic states in SiNCs have received a great deal of attention,[33-34] conventional experimental techniques are often limited to ensemble-level measurements, where the variations in DBs structures and local environments are averaged out.[32] A promising approach for addressing individual defects on SiNC surfaces is scanning tunneling microscopy (STM), which has proven to be uniquely suited for studies of individual DBs on silicon single-crystal surfaces.[35-38] Further, STM enables scanning tunneling spectroscopy (STS),[39] a technique that

has been used to visualize the electronic structures of individual DBs,[36] as well as complex structures composed of many DBs.[38, 40-42] However, until now, no STM/STS results describing DBs on SiNC surfaces have been reported, even though STS has been used to study quantum-confined,[43] as well as defect-induced,[44] electronic states in individual SiNCs.

4.3. Methods

Using previously published protocols,[44] experiments were performed in a home-built ultra-high vacuum (UHV) cryogenic (closed-cycle cryostat-based) STM system.[45] A Au(111)/mica substrate was prepared in situ using multiple neon sputter/anneal cycles. Hydrogen-passivated SiNCs were fabricated using a protocol described previously.[46] The SiNCs were suspended in pentane, and using a solenoid pulse-valve were deposited onto the Au(111) surface in high-vacuum conditions, parameters were chosen so as to obtain monolayer NC coverage. The SiNC covered Au(111) substrate was subsequently annealed overnight in UHV at ~50 °C to remove any residual pentane from the sample surface. All STM topographies and STS measurements were obtained at a temperature of ~20 K using silver tips prepared by electrochemical etching and subsequent sputtering in UHV. All STS spectra were recorded using the lock-in technique at 570 Hz and bias modulations varying from 10 (individual spectra and 1-D spatial scans) to 50 mV (2-D DOS maps). Thermal drift must be carefully monitored during the STS

measurements in order to maintain tip-sample spatial registry. Typical lateral drift values during the reported STS measurements were <0.2 Å for single-point spectra, ~1.7 Å for 1-D STS maps, and ~2.7 Å for 2-D maps (the numbers are different due to the different acquisition times used for each type of measurement). While displacements during single-point STS were negligible, locations of individual data points in STS maps were drift-corrected by using an appropriate constant drift rate for each measurement (as determined from STM imaging). To ensure constant drift rates, the piezo creep associated with spatial repositioning was minimized by allowing the STM piezos to equilibrate for more than ~15 hours, after which the drift rates were found to be nearly constant within the time frame required for acquisition of a STS map.[45] Theoretical calculations were performed using DFT, as implemented in the pseudo-potential package SIESTA,[47-48] employing local density approximation (LDA) exchange, as described previously,[49] which, for hydrogenated SiNCs smaller than 4 nm in diameter, provides a good approximation of electronic bandgaps.[16]

4.4. Results and Discussion

In this report, we describe, for the first time, spatially–resolved STS mapping of charged and neutral DB defects created by current-induced dehydrogenation of individual hydrogen-terminated SiNCs. SiNCs were sprayed onto a Au(111) substrate held in high-vacuum conditions, and studied using an ultra-high vacuum (UHV) cryogenic scanning tunneling

microscope (STM)[45] (see supplementary material for further experimental details). The deposited SiNCs formed a near-monolayer film on Au(111), with individual SiNCs appearing as protrusions with lateral dimensions of 2 to 4 nm, as shown in Figure 4.1(a). To characterize the electronic structures of individual SiNCs, we recorded the differential tunneling conductance (dI/dV) as a function of the applied bias voltage and location. Thus produced dI/dV (STS) spectra are interpreted as

---

Figure 4.1. STM/STS characterization and theoretical modeling of SiNCs. (a) Topography of an area showing several SiNCs. (b) Enlarged topography corresponding to the dashed square in (a). (c) STS spectra measured at locations A and B marked in (b). Curves A_1 through A_7 show transformations of the LDOS spectra in location A with successive application of bias voltage pulses (see text for details). States marked 'H' and 'E' correspond to occupied and unoccupied states, respectively, except for features caused by "reverse" tunneling, as described in the text. Spectra are offset for clarity. (d) Model of fully hydrogen–passivated SiNC (composition $H_{172}Si_{239}$). (e) Theoretical LDOS spectra averaged over the entire NC surface. Spectra FH and R correspond to the fully hydrogen–passivated SiNC in (d), and to the completely reconstructed SiNC in (f), respectively. Spectrum PR corresponds to a partially reconstructed version of SiNC from (d), with 33% of dihydrides converted to monohydride dimers. DB^0, DB^+, and DB^- are spectra of the completely reconstructed model with an additional DB and charges 0, $+e$, and $-e$, correspondingly. Spectrum SDB^- illustrates the effect of "bipolar" tunneling on STS of electronic states with LDOS described by curve DB^-. Spectra were Gaussian–broadened by 100 mV, with onsets corresponding to the discrete energy levels obtained from DFT calculations. All spectra were modeled assuming a finite bias voltage drop inside the SiNC (see text). (f) Model of a monohydride–passivated SiNC (composition $H_{100}Si_{239}$) with 2×1:H surface reconstruction, and silicon core identical to that of (d). Location of the DB is also indicated. For further details of the measurements including spatial drift estimates, see supplementary material.

EXPERIMENT

(a)

1 nm

(b)

B

A_n

1 nm

Topo, nm

0 — 1.1

THEORY

(d) full H

(f) reconstructed

DB

1 nm

(c) Occupied states   Unoccupied states

H_2^{A1} H_1^{A1} E_1^{A1} E_2^{A1}

Bandgap

A_1

x5 H_1^{A2} E_1^{A2} E_2^{A1}

A_2

E_1^{A3} E_2^{A3} E_3^{A3} x5

H_1^{A3} A_3

x5 H_D^B E_D^B E_1^B x5

B

H_D^{A4} E_D^{A4} E_1^{A4} E_2^{A4} x5

A_4

x5 H_D^{A5} E_D^{A5}

A_5

H_D^{A6} A_6 E_D^{A6}

H_D^{A7} E_D^{A7}

x5 A_7

dI/dV, arb. units (~ LDOS)

0

-2.0   -1.0   0   1.0   2.0
Sample bias, V

(e) Occupied states   Unoccupied states

H_1^{FH} E_2^{FH}

E_1^{FH}

FH

H_1^{PR} E_3^{PR}

E_2^{PR}

E_1^{PR}

PR

H_1^R E_3^R

E_2^R

E_1^R

R

H^{D0} E^{D0}

DB^0

E^{D+}

DB^+

H^{D-}

DB^-

SDB^- E^{SD-}

H^{SD-}

LDOS, arb. units

0

-2.0   -1.0   0   1.0   2.0
Sample bias, V

48

energy-dependent local density of states (LDOS) spectra with the bias voltage giving the energy scale. Thirty individual SiNCs were studied in this fashion, as detailed in the following for one representative SiNC [Figure 4.1(b)].

STM–induced dehydrogenation of single-crystal silicon surfaces has been studied in detail in the past two decades, with significant insights achieved into the physical mechanisms of hydrogen desorption[50] and the electronic structures of dehydrogenated areas.[51-52] Generally, elevated bias voltages are required, with the exact magnitude of the bias voltage and tunneling current strongly affecting the mode of desorption, which can involve either direct electronic or multiple-vibrational excitation of the Si-H bond via tunneling electrons.[53] This process is thus referred to as electron-stimulated desorption (ESD).[54] Depending on the chosen parameters of the voltage pulse, hydrogen desorption can either occur one atom at a time, or involve several atoms.[55] In our experiments, in order to induce desorption of hydrogen, we applied voltages in the range of ~ 2.5 – 3 V, chosen to be sufficiently low to prevent extensive changes to the SiNC surfaces. For single-crystal silicon surfaces, the desorption of hydrogen at such bias voltages was previously attributed to multiple vibrational excitation via electrons tunneling through the σ^* (Si-H) unoccupied orbital.[50, 53, 56]

Before ESD was induced by STM, LDOS spectra measured at different locations of "pristine" SiNCs showed progressions of electronic

states with electronic bandgaps closely matching those predicted by theoretical calculations.[44] For example, in the case of the chosen representative SiNC from Figure 4.1(b), the apparent bandgap of ~2.5 eV was found, formed by an occupied state H_1^{A1} and an unoccupied state E_1^{A1} in curve A1 of Figure 4.1(c) [we define the bandgap as the voltage difference between the onsets of conduction]. This bandgap value is expected to be larger than the real bandgap due to the finite bias voltage drop inside the NC: in a biased tunnel junction involving a NC, a finite voltage drop occurs across the NC volume shifting the energy of all electronic states by $\alpha e V_B$ (where V_B is the bias voltage, and $\alpha < 1$ is a function of the NC dimensions and dielectric susceptibility). This means that the voltage corresponding to the onset of tunneling for a state with energy E_S (this energy is measured with respect to the Fermi level of the sample, and can be positive or negative) can be then calculated as $E_S/(1 - \alpha)$.[57-58] Here, we roughly estimate α to be ~0.2 (as explained further in the supplementary material, Figure B.1-B.2), which gives a real bandgap of 2.5 eV × 0.8 = 2 eV. This value is consistent with that obtained from density functional theory calculations,[49] as illustrated by the LDOS spectrum FH in Figure 4.1(e),[16] calculated (taking into account the finite value of α) for a model hydrogen-passivated SiNC shown in Figure 4.1(d). (The diameter of this SiNC is ~2.2 nm, which matches that extracted from Figure 4.1(b) after correcting for the tip convolution effects, as explained in Ref. 44.) Our calculations show that each one of

the LDOS peaks is comprised of several quantum-confined electronic states formed from Bloch states associated with different electronic valleys in the Brillouin zone of bulk silicon.[16-17, 44] Due to their close energy spacing, these states are not completely resolved in our LDOS spectra, where electronic peaks are significantly broadened (typical peak width of ~200 mV) by coupling of tunneling electrons to vibrational excitations.[59]

For each "pristine" SiNC, after recording LDOS spectra at several representative locations, we attempted to induce ESD by applying higher bias voltages (2.5 - 3 V), and quantified the results at each step by detailed mapping of LDOS in order to establish the presence of DBs. For the SiNC from Figure 4.1(b), application of higher bias voltages resulted in formation of new peaks H_n^{A2} and E_n^{A2} [curve A_2 of Figure 4.1(c)], and a notable reduction in the apparent bandgap. Importantly, peaks H_n^{A2} and E_n^{A2} are delocalized over the entire SiNC surface (Figure B.3) suggesting that they do not correspond to localized defects. This behaviour can be explained by reconstruction of the SiNC surface induced by the hydrogen desorption. Specifically, while a significant portion of Si surface atoms in the as-synthesized SiNCs are passivated with dihydride groups (Figure B.4), hydrogen desorption from neighbouring SiH_2 can lead to their dimerization analogous to the 2×1:H reconstruction observed on the Si(100) surfaces [see Figure 4.1(f) for a model of a fully reconstructed monohydride-only SiNC with the same Si core as in Figure 4.1(e)]. The

DBs at the neighbouring Si atoms form π-electronic bonds producing delocalized states with an electronic bandgap reduced by an amount dependent on the extent of surface reconstruction, as shown by curves PR and R in Figure 4.1(e) for the partially- and fully reconstructed models of the SiNC. Indeed, curve A_2 of Figure 4.1(c) likely corresponds to a partially reconstructed SiNC because further ESD pulses on this SiNC resulted in additional reduction of the bandgap [curve A_3 of Figure 4.1(c)], with electronic peaks H_n^{A3} and E_n^{A3} delocalized across the SiNC surface (Figure 4.2).
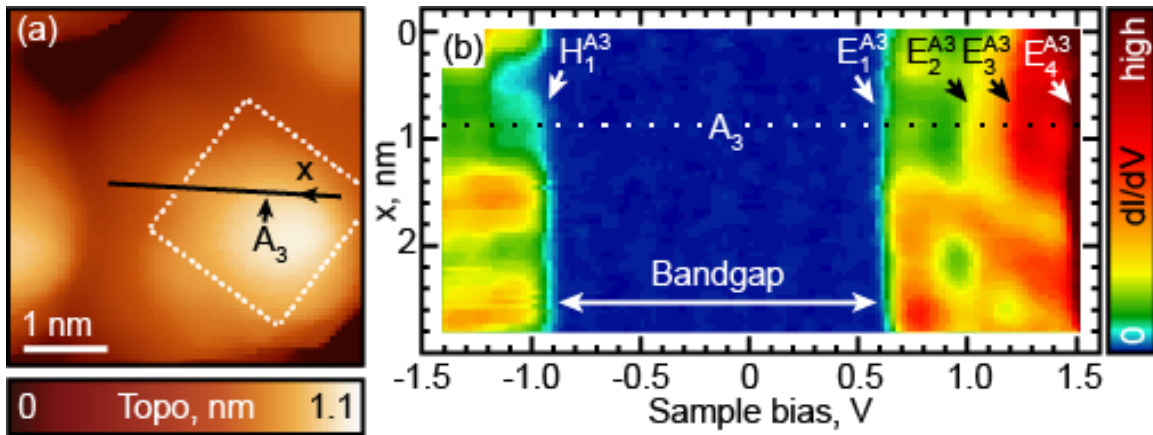
Figure 4.2. Spatial mapping of LDOS for the SiNC from Figure 4.1(b) after (partial) dehydrogenation, but before DBs were generated. (a) Topography of the SiNC. (b) LDOS as a function of the bias voltage and position x along the path (solid line) shown in (a).

With additional ESD pulses, however, spatially localized midgap LDOS features, attributable to defects, appear on the SiNC surface, with three representative examples demonstrated by curves B, A_4 and A_5 in Figure 4.1(c). Specifically, curves B and A_5 show pairs of midgap peaks (H_D^B and E_D^B, as well as H_D^{A5} and E_D^{A5}, respectively), while curve A_4 shows

52

only one midgap peak E_D^{A4}. Intriguingly, we found that inter-conversion between the different defect types was possible. In particular, defects B and A4 in Fig 1(c) could be spontaneously converted to defects of type A5 under typical tunneling conditions (bias voltage ~2 V). For example, curve A5 was recorded at the same location as A4 immediately after a positive bias voltage of 2.4 V was applied. Further transformation could be induced by applying voltages of ~−1.5 V with the resulting LDOS spectrum corresponding to curve A6, which is very similar to that of defect B measured earlier at location B [Figure 4.1(b), and curve B in Figure 4.1(c)]. Finally, the local spectrum at location A was converted from A6 to A7 [Figure 4.1(c)] showing a shape qualitatively similar to that of A5 (the origin of peak shifts in curve A7 versus A5 is explained in the following).

The spectral characteristics of the observed midgap states, as well as the possibility for their inter-conversion, can be explained in the most straightforward manner by attributing these midgap states to DB defects, as discussed further below. Some of the described peaks, however, are produced by different tunneling processes rather than distinctly different electronic states, as can be seen from the dramatically different spatial behaviors of these peaks. For example, for curve A7 in Figure 4.1(c), peak E_D^{A7} shows substantial onset voltage variations across the NC, while peak H_D^{A7} and other unoccupied states appear at nearly the same voltages in all locations, as illustrated in Figure 4.3(b). This is despite the fact that

peaks E_D^{A7} and H_D^{A7} are closely co-localized in the vicinity of location A

[Figure 4.1(b)], as shown by LDOS maps of Figure 4.3(b) and Figure

4.3(d)-(e), and should therefore correspond to the same defect. The

described asymmetry in onset voltage variations are analogous to those

reported for the "bipolar" tunneling investigated previously for a variety of

molecular systems.[57-58, 60] Bipolar tunneling is a consequence of the fact

that in a biased tunnel junction involving a NC, a finite voltage drop

occurs across the NC volume, which, in addition to the "direct" type of

tunneling described earlier [Figure B.1(a)] with the onset voltage of

$E_S/(1 - \alpha)$, also leads to "reverse" tunneling [Figure B.1(b)] with the onset

voltage of $-E_S/\alpha$ (where E_S and α were defined previously).[57-58] Voltage

onsets for both "direct" and "reverse" tunneling (at opposite bias

polarities) vary with tip position on the NC surface due to the sensitivity

of α to the geometry of the junction,[57] as shown in Figure B.2.

Nevertheless, because α is typically small [$\alpha \approx 0.2$ for peaks E_D^{A7} and H_D^{A7}],

expression $E_S/(1 - \alpha)$ varies significantly less than E_S/α, which explains

the differences in the onset voltage variations for peaks E_D^{A7} and H_D^{A7} in

Figure 4.3(b). In addition, the spectral lineshapes of the two types of

bipolar peaks are affected by the asymmetry in the tip-NC and NC-

substrate tunneling rates (the former is lower than the latter), which

tends to produce notably more intense and sharper peaks at the onset of

conduction for the "reverse" tunneling process.[57, 61] This is indeed

observed for peak E_D^{A7}, which, together with its spatial voltage onset

variations, suggests that this peak corresponds to the "reverse" tunneling process, while peak H_D^{A7} corresponds to "direct" tunneling. The effect of "bipolar" tunneling on the dI/dV curves is illustrated by curve SDB$^-$ in Figure 4.1(e) [obtained from curve DB$^-$ by assuming $\alpha \approx 0.2$, and a finite rate for tunneling between SiNC and substrate], where peaks E_D^{SD-} and H_D^{SD-} correspond to the "reverse" and "direct" tunneling processes, respectively, analogously to peaks E_D^{A7} and H_D^{A7} (we note that the overtone structures of peaks E_D^{A7} and H_D^{A7} were not included in the modelling).
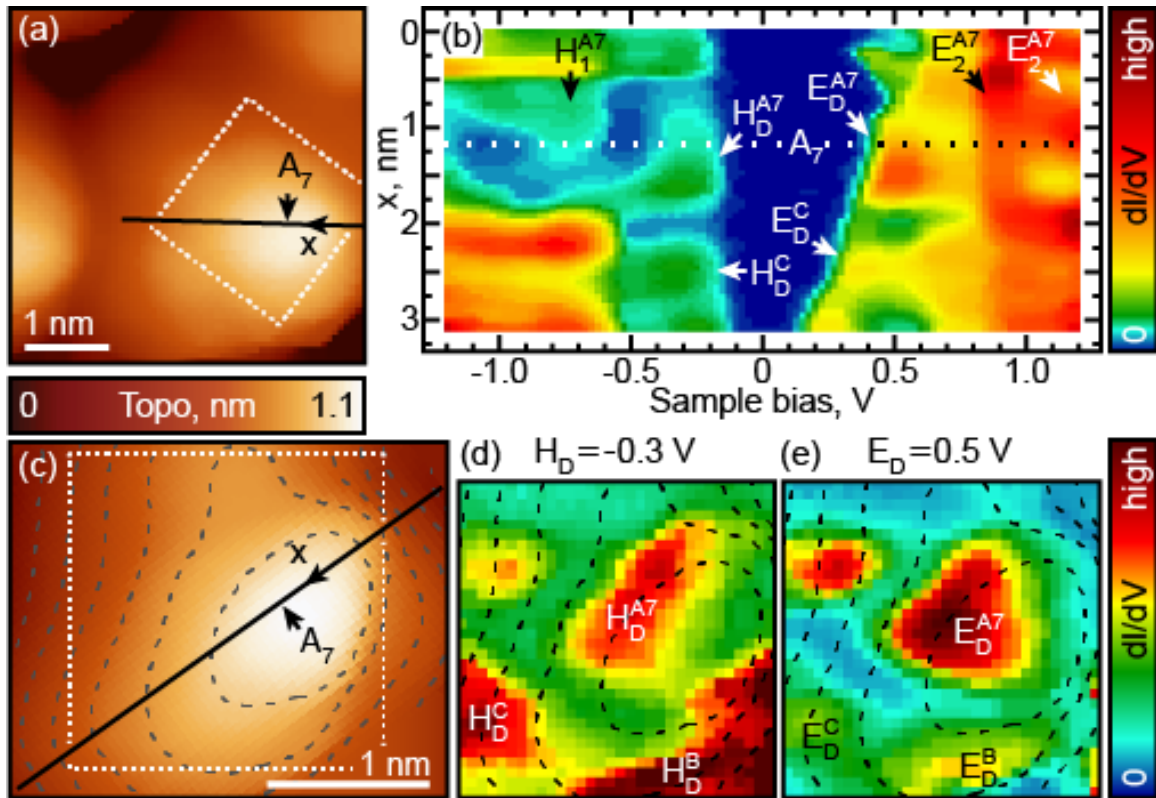
Figure 4.3. Spatial mapping of LDOS for the SiNC from Figure 4.1(b) after DBs were generated. (a,c) STM topographic images of the SiNC. (b) LDOS as a function of the bias voltage and position x along the path (solid line) shown in (a,c). (d,e) 2-D LDOS maps for voltages corresponding to H_D, E_D LDOS peaks marked in (b). Mapping area corresponds to the dotted squares in (a,c). Dashed lines are topographic contours from (c).

Analysis similar to that presented above for peaks E_D^{A7} and H_D^{A7}, when applied to the rest of the spectra in Figure 4.1(c), suggests that peaks E_D^B, E_D^{A4}, H_D^{A5}, E_D^{A6} and H_D^{A7} are all produced by "direct" tunneling, while peaks H_D^B, H_D^{A4}, E_D^{A5}, H_D^{A6} and E_D^{A7} should correspond to "reverse" tunneling. This assignment results in a clear distinction between curves B, A_4, A_6 versus the curves A_5 and A_7: while only unoccupied midgap states are distinguishable in curves B, A_4, and A_6, in curves A_5 and A_7, only occupied midgap states are clearly observable. This assignment offers an explanation for the inter-conversion between the different types of spectra in Figure 4.1(c). For example, the transitions from spectrum A_4 to spectrum A_5, and spectrum A_6 to spectrum A_7 were induced with positive voltages (this corresponds to electrons being added to the SiNC), and resulted in disappearance of unoccupied midgap states E_D^{A4} and E_D^{A6}, as well as appearance of occupied midgap states H_D^{A5} and H_D^{A7}. Similar spectral transformations in individual atoms[62] and molecules[63] have been attributed to electron trapping. This suggests that individual electrons are likely being trapped in states E_D^{A4} and E_D^{A6}, which results in appearance of trap states H_D^{A5} and H_D^{A7}. On the other hand, transition from A_5 to A_6 occurred when negative voltage was applied, and the corresponding spectral changes may be attributed to extraction of an electron from state H_D^{A5}, which is thereby converted to state E_D^{A6}, similarly to the de-trapping process described for molecules.[63]

The local charging of SiNC described above is consistent with the presence of DBs, which have been shown to exist in different charge states on silicon surfaces,[36, 38, 64] and is also consistent with the expectation that desorption of hydrogen atoms should lead to the creation of DBs. In addition, DBs appear deep in the silicon electronic bandgap, similarly to the states appearing near zero bias in Figure 4.1(c). This similarity is illustrated by the theoretically calculated LDOS for DBs in different charge states on the surfaces of model SiNCs [curves DB^0, DB^+, and DB^- in Figure 4.1(e)]. For example, curve A_4 only shows an unoccupied midgap state, consistent with curve DB^+, while curve A_5 only shows an occupied state, consistent with curve DB^-. Assignment of spectra B, A_6 and A_7 is less certain because the "reverse" tunneling LDOS features seen in these curves may be obscuring "direct" tunneling features that would be expected for the neutral DB (curve DB^0). The similarity of spectra A_5 and A_7, however, suggests that A_7 may also be associated with DB^-. Curves B and A_6 are relatively similar, and given their distinct spectral shapes, may be attributed to a neutral state, even though they may also be variants of A_4 (DB^+ state) corresponding to slightly different local surface structures. We note that similar spectral features attributable to charged and neutral DBs were found in other studied SiNCs (Figure B.5).

4.5. Conclusions

In conclusion, our work shows that when sufficiently high-energy electrons are injected into SiNCs, dramatic changes in the SiNC electronic structures are observed: gradual shrinking of the SiNC electronic bandgap occurs initially, and is eventually followed by the appearance of localized states deep in the electronic bandgap. We find that these midgap states can exist in different inter-convertible charge configurations. These observations are consistent with the hypothesis that high-energy electron injection can lead to dehydrogenation of the SiNC surfaces, resulting in surface reconstruction driven by conversion of surface dihydride species to monohydride groups, and creation of dangling bonds in different charge states. These findings provide a direct visualization of possible scenarios for defect generation in SiNC-based optical and opto-electronic applications, where photo-generated charge carriers with sufficient energies could induce creation of surface defects.

4.6. Bridge to Chapter V

In the next chapter we will focus on self-trapping of charge carriers in SiNCs with an amorphous silicon shell. A surprisingly common type of structural irregularity found in SiNCs is a thin (angstrom-scale) amorphous silicon layer found at the SiNC surface. We report STS-based real-space observations of the reversible creation of intragap states in individual hydrogenated SiNCs.

CHAPTER V

CREATION AND ANNIHILATION OF CHARGE TRAPS IN SILICON NANOCRYSTALS: EXPERIMENTAL VISUALIZATION AND SPECTROSCOPY

5.1. Introduction

Recent studies have shown the presence of an amorphous surface layer in nominally crystalline silicon nanocrystals (SiNCs) produced by some of the most common synthetic techniques. The amorphous surface layer can serve as a source of deep charge traps, which can dramatically affect the electronic and photophysical properties of SiNCs. We present results of a scanning tunneling microscopy/scanning tunneling spectroscopy (STM/STS) study of individual intragap states observed on the surfaces of hydrogen- passivated SiNCs deposited on the Au(111) surface. STS measurements show that intragap states can be formed reversibly when appropriate voltage–current pulses are applied to individual SiNCs. Analysis of STS spectra suggests that the observed intragap states are formed via self-trapping of charge carriers injected into SiNCs from the STM tip. Our results provide a direct visualization of

the charge trap formation in individual SiNCs, a level of detail which

until now had been achieved only in theoretical studies.

5.2. Background

Silicon nanocrystals (SiNCs) have recently emerged as a promising

electronic material with potential applications in photovoltaics,[1-4]light-

emitting diodes,[5-6] sensing,[7] and thermo-electric devices.[8] Important

advantages of SiNCs are their efficient light emission and low toxicity,

which make SiNCs particularly suitable for biological tagging.[9-10] One of

the fundamental challenges in realizing these applications lies in

achieving precise control of the SiNC properties, in particular, control of

the SiNC surface chemistry, a difficult task due to the inherent variation

in SiNC surface structures and their susceptibility to interaction with

their environment.[11] While the impact of specific defects and impurities

on the electronic structure and photophysical properties of SiNCs has

been addressed in numerous theoretical studies, progress is hampered

by the lack of experimental techniques capable of targeting and

identifying individual defects, an essential requirement due to the highly

varied local structures, and, consequently, properties of different possible

defects. This capability was recently demonstrated with a high-stability

variant of scanning tunneling spectroscopy (STS),[12] which, in addition to

providing the local electronic spectra of quantum-confined states,[13] has

produced complete surface maps of the electronic structures of

individual SiNCs containing oxidative defects[14] and silicon dangling

bonds (DBs).[15] In addition to oxidative and DB defects, another surprisingly common type of structural irregularity found in SiNCs is a thin (angstrom-scale) amorphous silicon layer found at the SiNC surface.[16] Such amorphous layers have been found even in SiNCs synthesized at high (>1100 °C) temperatures[16] and have been argued to cause trapping of photoexcited holes and nonradiative relaxation of photoexcitation.[17] Despite their likely ubiquity, the nature of such charge traps has not been investigated experimentally, and only a limited body of relevant theoretical work is available.[18-20]

5.3. Methods

Experiments were carried out in a home-built ultrahigh vacuum (UHV) cryogenic STM system.[21] A Au(111)/mica substrate was prepared in situ using multiple neon sputter–anneal cycles. Hydrogen-passivated SiNCs were fabricated via thermal disproportionation in a polymeric sol–gel hydrosilicate precursor and subsequently liberated from the resulting oxide host matrix via a wet chemical etch (i.e., with HF/EtOH/H2O) using a protocol described previously.[22] The SiNCs were suspended in pentane and deposited onto the Au(111) surface in high-vacuum conditions using a solenoid pulse-valve. The deposition parameters were chosen so as to obtain monolayer NC coverage. The Au(111) substrate with deposited SiNCs was then degassed overnight in UHV at ~50 °C to remove any residual pentane from the sample surface. All STM topographies and STS measurements were obtained at a

temperature of~20 K using silver tips prepared by electrochemical etching and subsequent sputtering in UHV. All STS spectra were recorded using the lock-in technique at 570 Hz and a bias modulation varying from 10 (individual spectra and 1-D spatial scans) to 50 mV (2-D LDOS maps). 2-D LDOS mapping requires tip– sample spatial registry throughout the mapping process (typically, several hours). This capability is enabled by the unique spatial stability (better than ~0.2 Å/hour) of our STM system.[21]

5.4. Results and Discussion

In this Letter, we report STS-based real-space observations of the reversible creation of intragap states in individual hydrogenated SiNCs. Existence of these states is attributable to structural changes expected in amorphous silicon systems.[23] Hydrogen-passivated SiNCs were spray– deposited onto a Au(111) substrate in high-vacuum conditions and investigated using an ultrahigh vacuum cryogenic scanning tunneling microscopy (STM) instrument (see Methods for further experimental details). The deposited SiNCs formed a near- monolayer, with individual SiNCs appearing as protrusions with heights in the 2–4 nm range. Characterization of the electronic structures of individual SiNCs was performed by recording the derivative of the tunneling current dI/dV (differential conductance) as a function of the applied bias voltage (V) and the tip location. Obtained dI/dV spectra represent the local density of electronic states (LDOS), with the bias voltage giving the energy scale.

Studied SiNCs (~30 in total) typically displayed reproducible current–voltage characteristics and dI/dV spectra when sufficiently low bias voltages and tunneling currents were used in the measurements. Irreversible changes attributable to dehydrogenation of the SiNC surfaces were observed at higher voltages,[15] while higher currents often led to motion and/or repositioning of SiNCs on the Au surface. Intriguingly, in five of the studied SiNCs, we found that, in contrast to such irreversible changes, the current–voltage characteristics could be altered reversibly by applying relatively low (<1 V) bias voltages. We illustrate this behavior using a representative SiNC (Figure 5.1).

Figure 5.1. STM/STS characterization of a SiNC with bistable LDOS spectra. (a) Topographic image. (b) Three-dimensional rendering of topography from panel a. (c, d) I(V) and dI/dV curves measured at the locations marked in panel a. Each measurement is composed of a blue and red curve corresponding to the "forward" and "backward" bias ramps, respectively (see curves D for illustration). Switching events are seen as discontinuities in I(V) and dI/dV curves and are each marked with an asterisk "*". Each dI/dV curve serves as an estimate of the energy-dependent LDOS. An exception to this rule is peak E_F^f, which is caused by "reverse" tunneling through the same state as that of H_F^f (see text). Dashed lines H_E^b and E_F^f show the voltages corresponding to the band edge states, defined as states with LDOS delocalized over the entire SiNC surface.
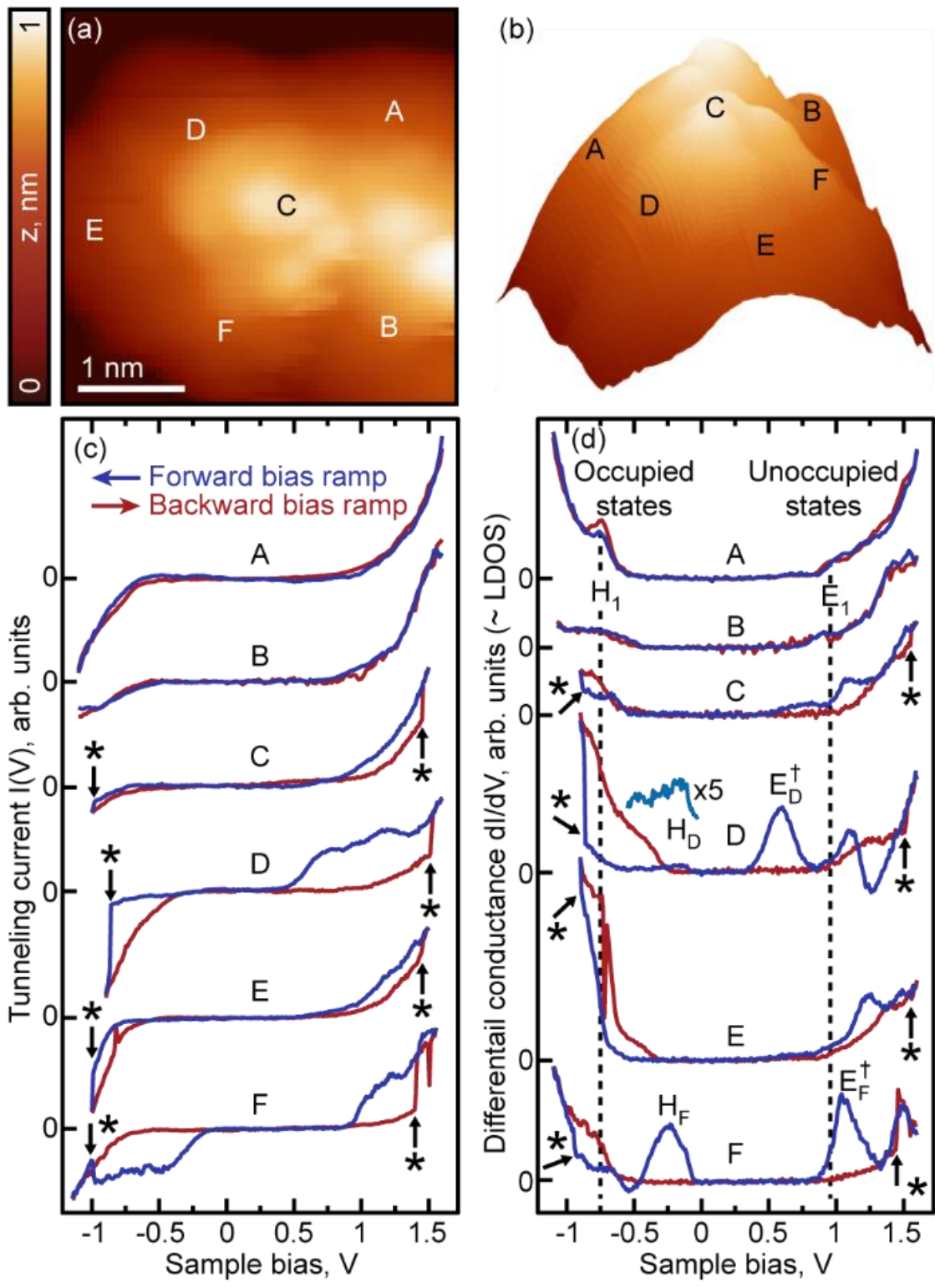
To establish the presence of bistability, we recorded the tunneling current by first ramping the bias voltage from 1.6 to −1.1 V (this will be referred to as the "forward" bias ramp, with the bounding bias voltages set sufficiently low to prevent irreversible changes in the chosen SiNC) and back to 1.6 V (the "backward" bias ramp). While for stable SiNCs, the current− voltage curves corresponding to the forward and backward bias ramps always overlapped, for the SiNC in Figure 5.1 we find that for some locations there are considerable discrepancies between the forward and backward curves (Figure 5.1c). For locations showing bistability (curves C−F in Figure 5.1c), each forward I(V) curve shows a discontinuity in current at approximately −1.0 V, while each backward I(V) curve shows a discontinuity at approximately +1.5 V. Thus, in the course of each measurement, the SiNC changed its state at a sufficiently high negative bias and switched back to the original state when a sufficiently large positive bias was applied. Importantly, the shapes of forward and backward I(V) curves remained nearly unchanged upon subsequent measurements, with only slight (±100 mV) variations in the voltages corresponding to transitions between the states. Despite this highly reproducible and robust behavior, I(V) curves measured at different locations showed considerable differences, which become more apparent in the corresponding dI/dV curves (Figure 5.1d). The dI/dV curves in Figure 5.1d show highly location-sensitive patterns of peaks attributable to (vibronically broadened[24]) electronic states. Further,

individual peaks E_C^f, E_D^f, E_E^f, and E_F^f (these nominally correspond to unoccupied states) as well as peak H_F^f (caused by an occupied state) are found in the forward curves C–F of Figure 5.1d but not in the corresponding backward dI/dV curves, which instead show new occupied states H_C^b, H_D^b, H_E^b, and H_F^b.

The sensitivity of the LDOS to the specific location of the measurement observed in Figure 5.1d suggests the presence of localized states. To better understand the nature of LDOS peaks observed in Figure 5.1d, we focus on their spatial variation across the SiNC surface. By recording a progression of forward and backward LDOS spectra along a path defined on the SiNC surface, we obtained two data sets corresponding to one- dimensional (1-D) spatial cross sections of the SiNC electronic "landscape" (Figure 5.2). The forward data set (Figure 5.2c) shows spatially colocalized peaks H_F^f and E_F^f, previously observed in curve F of Figure 5.1d. These peaks are both entirely absent in the backward data set (Figure 5.2d). Instead, a pair of colocalized peaks H_F^b and E_F^b appear in Figure 5.2d. The localized nature of the observed peaks suggests that they are not associated with band- edge states but are rather associated with structural defects. The different localizations of peaks in the forward and backward data sets suggest that they originate from different structural defects, i.e., the SiNC structure changes in transition from forward to backward scan.

In addition to the structure-based interpretation of LDOS bistability, Figure 5.2 offers the opportunity to clarify the origin of the observed peaks: defect-related states localized on the top surface of the SiNC can be expected to produce LDOS peaks at both bias polarities, a consequence of the existence of two tunneling barriers (tip to SiNC gap, and SiNC itself) separating the state in question from the tunneling contacts.[15] The asymmetric distribution of the applied bias voltage across the two barriers leads to asymmetric onsets of tunneling for the two bias polarities, which manifests itself in Figure 5.2c as a noticeable location-dependent onset voltage variation of peak E_F^f, in contrast to peak H_F^f which, despite being closely colocalized with peak E_F^f, does not show any distinguishable onset voltage variation. The spatially dependent onset voltage variation identifies peak E_F^f as being due to "reverse tunneling" through the same state as that of H_F^f, which (as all other LDOS peaks in Figure 5.2) is caused by "direct tunneling" (see the Appendix C for further details). In the following, we focus on the dI/dV features associated with "direct tunneling" because they are more representative of the SiNC LDOS features.

To obtain a more complete LDOS map of the SiNC and identify areas of bistability, we recorded the forward and backward pairs of LDOS spectra on a square grid of points across the SiNC surface (Figure 5.3). Cross sections of these forward and backward data corresponding to specific bias voltages are presented in Figure 5.3b, where three main

bistable areas enclosing points D, E, and F are identified. For example, in the vicinity of point D, forward maps for bias voltages ranging from 0.4 to 0.9 V show the presence of states E_D^f and E_E^f, which are not observed in the backward maps corresponding to the same voltages.
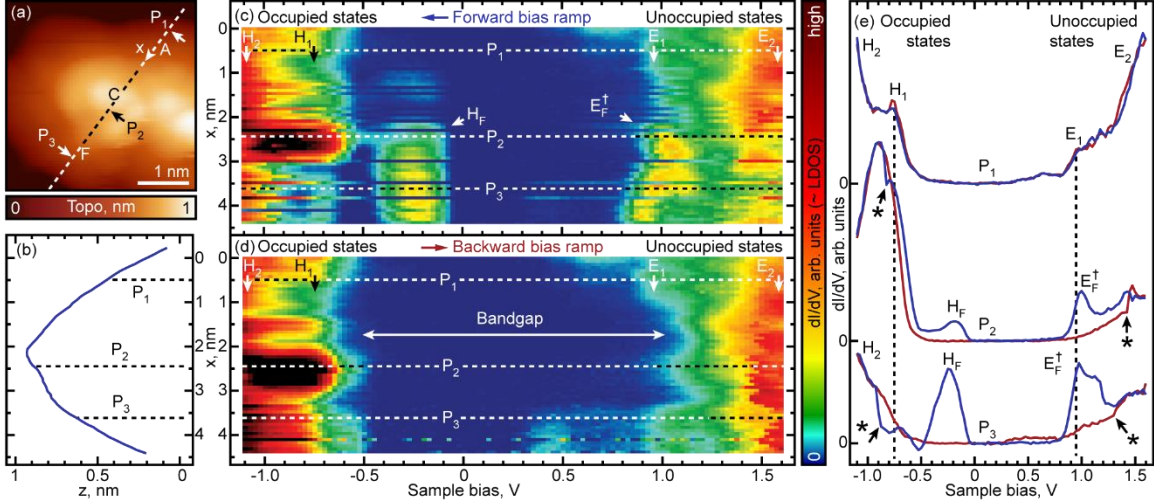
Figure 5.2. Spatial cross section of LDOS across the SiNC from Figure 5.1. (a) STM topographic image of the SiNC. (b) Topography profile along the path x shown in panel a with a dashed line. (c, d) "Forward" and "backward" bias ramp LDOS as a function of the bias voltage and position x along the path shown in panel a. (e) Individual LDOS spectra from panels c and d measured at points P1 through P3. Spectra are offset for clarity. Switching events are marked with an asterisk "*". Horizontal lines of data that appear "discontinuous" in panel c are identical to those found in panel d: the switch that typically occurs at negative voltages occurs at positive voltages for these lines. The spatial continuity of data assembled from different forward and backward LDOS spectra in panels c and d points to the extremely robust nature of the observed switching behavior.

Instead, similarly localized states H_D^b and H_E^b appear in the backward maps at bias voltages from −1.0 to −0.3 V (no such peaks can be seen in the corresponding forward maps). The fact that LDOS in areas E and D appears and disappears at nearly the same voltages suggests

68

that bistability in both areas has a similar origin, even though the corresponding LDOS spectra (see curves E and D in Figure 5.1d) are not identical. The third bistable area is associated with state H_F^f localized in the vicinity of point F and is visible from −0.4 to −0.1 V (its "reverse tunneling" counterpart is also visible at 0.8 to 1.3 V) only in the forward maps, but not in the backward maps. Instead, the backward maps show state E_F^b from 0.4 to 0.6 V. Significantly, in contrast to the areas of bistability described above, outside of these areas, forward and backward maps are nearly identical for all voltages in the scanned range.

The spectroscopic data of Figures 5.1−3 demonstrate that the described bistable electronic states are intragap in nature, which, together with their localized character, suggests that these states must be associated with structural defects on the SiNC surface. Some of the most common defects capable of producing intragap states on the SiNC surface are oxidative defects.[25-28] However, elementary defects of this type do not produce deep intragap states such as the ones described above,[14] even though oxidative defects may possibly be contributing to the location-dependent voltage onsets of the band edge states observed, for example, in Figure 5.3. A potential source of deep intragap states showing bistable behavior (e.g., "blinking"[29]) are DBs, which could be created, for example, via dehydrogenation induced by the tunneling current.[15] Previous STS work has shown that DBs can be found in different charge states leading to LDOS spectra showing deep intragap peaks.[15]
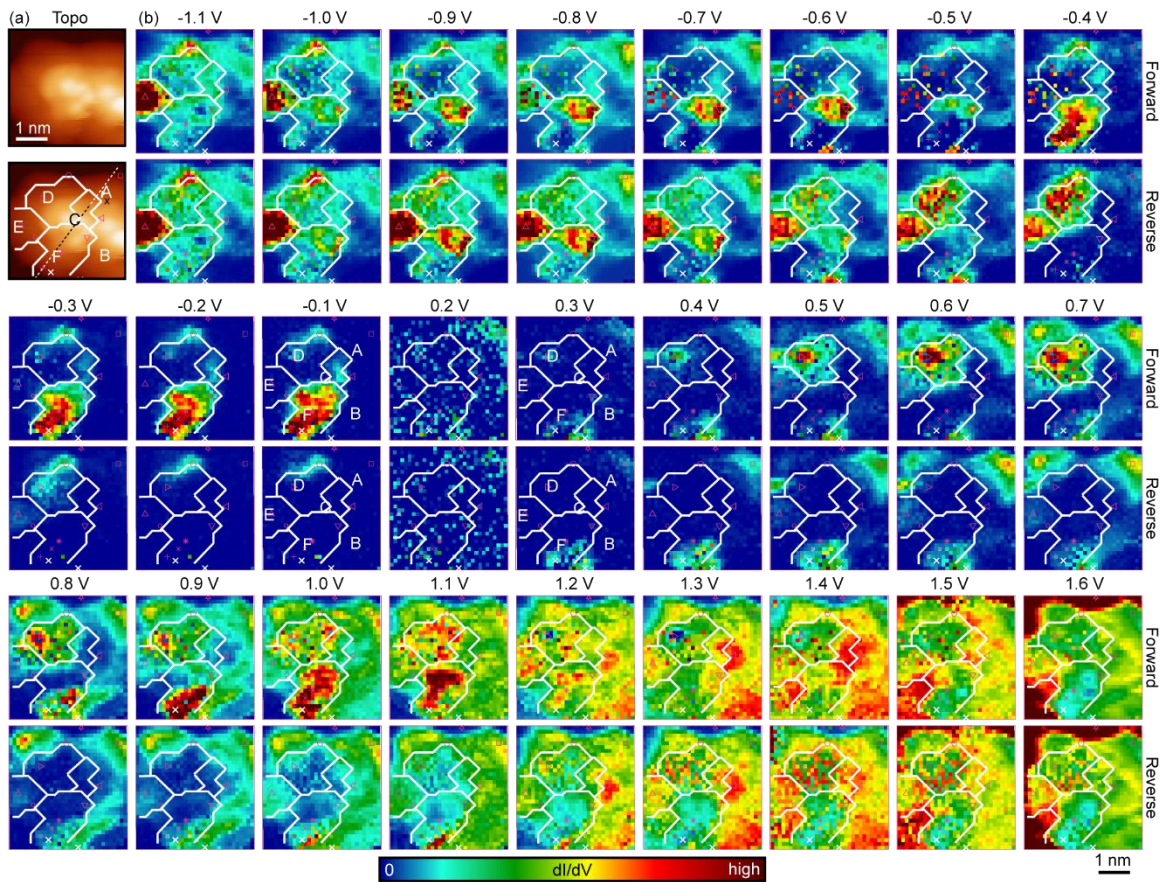
Figure 5.3. Spatial mapping of LDOS across the SiNC from Figure 5.1. (a) STM topographic image of the SiNC. (b) LDOS maps for selected bias voltage values (band gap omitted). LDOS data was collected by recording the "forward" and "backward" pairs of spectra on a square grid of points across the SiNC surface. LDOS maps shown here are "cross sections" of these forward and backward data sets corresponding to specific bias voltages. For each bias voltage value, the upper (lower) map corresponds to the forward (backward) bias ramps. Individual pixels that appear to contain discontinuous data points correspond to points where conversion between forward and backward occurred at different voltages. Contour lines outline boundaries of distinctive features in LDOS maps (maps corresponding to 0.5, −0.1, and −0.4 V were used to define the boundaries). Locations from Figure 5.1a are also shown in panel a and the 0.3 V map in panel b.

Furthermore, similar to the present experiment, transitions between the different charge states could be effected by application of sufficiently high bias voltages: electrons could be extracted from negatively charged or

neutral DBs at negative bias voltages (when electrons tunnel from SiNC to the STM tip), or, alternatively, electrons could be added to a positively charged or neutral DBs at positive bias voltages (when electrons tunnel from the STM tip to SiNC).[15] At first glance, this charge-related bistability of DBs may appear to be consistent with the bistable behavior in point F (curves F in Figure 5.1d): occupied state H_F^f indeed disappears after a switching event at a negative voltage possibly leading to extraction of an electron. However, the backward spectrum does not contain any identifiable intragap states, which is inconsistent with LDOS expected for a DB in any charge state.[15] Bistability of states E_D^f and E_E^f is also unlikely to be produced by transitions between the different charge states of a DB because one would expect the unoccupied states E_D^f and E_E^f to disappear at a positive voltage (upon trapping of an electron), rather than negative voltages, as observed in the forward curves D and E of Figure 5.1d.

Another possible mechanism for the observed bistability of intragap states could involve reversible tunneling-induced motion of DBs on the SiNC surface, analogous to that observed on a hydrogen-passivated Si(100)-(2 × 1) surface (with one hydrogen atom passivating each Si dimer atom).[30-31] The motion of DBs in this system is confined, however, to individual Si dimers, while the spatial delocalization of the observed bistable states (areas E, D, and F in Figure 5.3) is considerably larger than the corresponding Si−Si interdimer distance (2.41 Å[30]), which means that this type of DB motion would not lead to a complete

disappearance of intragap states from LDOS spectra, contrary to the observations of Figure 5.1d. In principle, one could consider the possibility that motion of DBs over greater distances may be involved. However, the energetic barriers associated with such motion are in excess of the tunneling electron energies found to induce switching in our experiments.[32]

Common types of defects discussed above are thus unlikely to be the source of the observed bistable intragap states. However, in our consideration of the possible types of SiNC defects, we have so far ignored the fact that nominally crystalline SiNCs can contain a thin surface layer of amorphous silicon. This is true even for high-temperature synthetic methods, such as the one used in the present work: thermal disproportionation in a sol–gel hydrosilicate precursor and subsequent hydrofluoric chemical etch (see Methods for further details).[22] The presence of such amorphous layers in similarly synthesized SiNCs has been observed directly by using advanced transmission electron microscopy techniques,[16, 33] as well as indirectly by using high-energy X-ray diffraction coupled with atomic pair distribution function analysis[34] and by using near edge X-ray absorption fine structure spectroscopy.[35] Raman spectroscopy has been shown to be a particularly sensitive tool for identifying the local bond order in nanostructured silicon and has been used to quantify the relative amounts of the nanocrystalline and amorphous phases in mixed-phase

silicon nanoparticles.[36] Consistent with findings for such nanoparticles, Raman measurements on SiNCs synthesized in our work showed the presence of spectral peaks attributable to both nanocrystalline and amorphous phases of silicon (Figure 5.4). In accordance with these results, our STM and STS data also suggest the presence of amorphous shells on the bistable SiNCs. For example, close inspection of the dI/dV maps in Figure 5.3 shows that the intragap states appear to have filament-like structures, contrary to the expected quantum-confined states in crystalline SiNCs,[37-39] but in-line with expectations for amorphous silicon.[40-41] Another line of evidence for the presence of amorphous silicon is provided by LDOS mapping: the band edges for bistable SiNCs typically show onsets that fluctuate noticeably across the SiNC surface (Figure 5.2), while crystalline SiNCs show band onsets that are independent of location.[14]

Consistent with these findings, STM images of bistable SiNCs did not show any obvious crystallographic features, in contrast to SiNCs without bistable states, where evidence of faceting was found in STM imaging.[14] These observations suggest that different SiNCs may have amorphous surface layers of varied thicknesses resulting in varied electronic structures. Nevertheless, the bistable SiNCs are likely not entirely amorphous because two-dimensional (2-D) LDOS maps (such as the ones shown in Figure 5.3) show features that appear to have specific orientations (as can be seen, for example, from the boundaries of the

bistable areas), which could be explained only by the presence of a substantial amount of crystalline material.
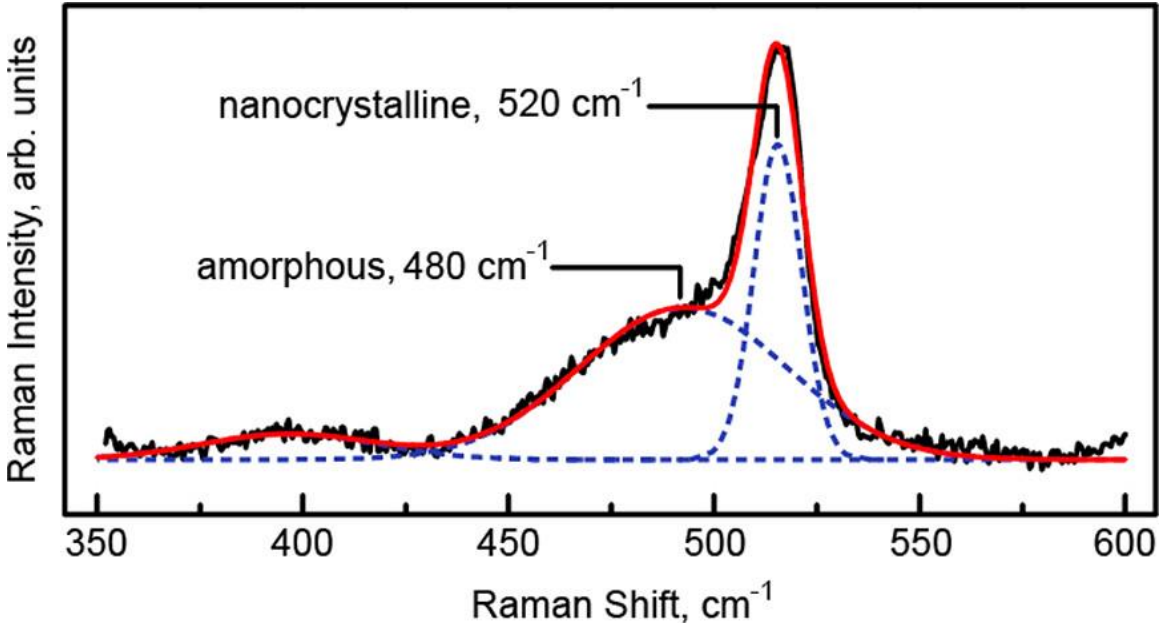
Figure 5.4. Representative Raman spectrum of SiNCs used in the present study (black curve). The spectrum is composed of three main spectral peaks (blue dashed curves; red curve shows the sum of components) attributable to different phonon bands. Peaks at 520 and 480 cm⁻¹ are attributed to optical phonon modes associated with the nanocrystalline and amorphous phases of silicon, respectively (see the Appendix C for further details).

Given the high likelihood that the bistable SiNCs could contain amorphous silicon, to explain the bistable behavior observed in our experiments we invoke the physical picture developed in recent theoretical studies of reversible light-induced changes in hydrogenated amorphous silicon, known as the Staebler–Wronski effect.[42] This work has shown that the inherently disordered nature of amorphous silicon can serve as a source of intragap states that arise entirely from the

presence of strained silicon bonds.[20, 23, 40-41] The part of the developed

theoretical model that is particularly relevant to our results is the self-

trapping of holes accompanied by structural deformations of the silicon

bonds leading to locally bistable behavior.[20, 23, 43] Indeed, the appearance

of intragap peaks H_D^b and H_E^b in the reverse spectra of Figure 5.1d could

be attributed to self-trapping of holes created at −0.9 V. The local

deformation of the SiNC surface created after this self-trapping (and the

resulting metastable states H_D^b and H_E^b) could persist unaltered until a

reverse transition is induced at positive voltages (at ∼1.5 V). The reverse

transitions result in the appearance of intragap peaks E_D^f and E_E^f, which

can also be attributed to self-trapping, but in this case self-trapping of

electrons rather than holes. The two types of structural deformations

associated with self-trapping of holes and electrons thus must have a

mutually opposing nature, which is in accordance with recent electronic

structure calculations showing that in amorphous silicon, intragap

occupied (unoccupied) states are localized on connected subnetworks of

short (long) bonds.[41]

In contrast to self-trapping in locations D and E, observed as the

appearance of intragap peaks H_D^b and H_E^b, intragap peak H_F^f observed at

location F disappears rather than appears at negative voltages when

tunneling produces (individual) transient holes in the SiNC. In addition,

peak H_F^f is created when positive (rather than negative) voltage is applied.

Because positive voltage polarity corresponds to addition of electrons to

the SiNC, and peak H_F^f corresponds to an occupied state, the above observations suggest that H_F^f corresponds to an electron trap state created in a fashion similar to that of peaks E_D^f and E_E^f, but with a larger self-trapping energy, such that H_F^f ends up below the Fermi level of the sample. The disappearance of peak H_F^f at -1.0 V can then be explained as extraction of the trapped electron from the SiNC, with the overall physical picture being analogous to that described previously for charging and discharging of individual atomic[44] and molecular charge traps.[45]

Thus, following the theoretical model developed for amorphous silicon,[20, 23, 40-41] the bistable LDOS spectra observed in all of the principal areas of Figure 5.3 can be attributed to charge carrier self-trapping in the surface amorphous silicon layer. Similar types of hysteresis in I(V) and dI/dV spectra were observed in other bistable SiNCs, even though the precise energetics of the corresponding electronic states varied by a few hundreds of millielectronvolts (Figures C.2−C.4). The varied energetics of bistable LDOS, together with the varied spatial morphologies of the bistable intragap states, further support our interpretation of the observed bistability as a consequence of charge carrier self-trapping in the amorphous silicon shells of the studied SiNCs. We note that the percentage of bistable SiNC in our experiments

is likely to be higher than that found via STS measurements because these probe only the very top surfaces of SiNCs.

5.5. Conclusions

By using a combination of LDOS spectroscopy (STS) and LDOS real-space mapping we have shown that SiNCs can exhibit electronic structure bistabilities attributable to charge carrier self-trapping in their amorphous silicon shells. Our results serve as a direct visualization of pathways available to excited charge carriers in SiNCs, where the extra energy associated with electronic excitation can facilitate a local structural change leading to self-trapping. We hope that our approach will prove beneficial in helping establish the role of similar surface trap states in the photophysics of SiNCs, where charge carrier self-trapping has been strongly implicated as a major source of nonradiative decay in photoexcited SiNCs.[17] Significantly, our results are applicable to SiNCs synthesized by other methods, in particular plasma-assisted and solution-based syntheses, where the presence of amorphous silicon is also expected.[17]

5.6. Bridge to Chapter VI

Now let us turn our attention from zero-dimensional quantum dots to a two-dimensional ultra-thin film of a dielectric. As shown in chapter II, STM require substrates with a nonzero conductance. This means any sample of interest will need to be adsorbed on the conducting metal substrate, which unfortunately causes the electronic states of the sample

and metal to strongly hybridize. An ultra-thin film of a wide bandgap dielectric, meaning only a few atoms thick, still allows for electrons to tunnel through the insulating layer, but the sample of interest is electronically decoupled from the substrate. We will use STM and STS to show, for the first time, the existence two distinct crystal structures existing simultaneously, one an exotic crystal structure not found in bulk crystals, and the second equivalent to the (100) face.

CHAPTER VI

DENSITY DEPENDENT SURFACE RECONSTRUCTION IN MONOLAYERS OF RUBIDIUM IODIDE

The experimental work described in this chapter was conducted by Benjamin W. Mcdowell, Motoaki Honda, and myself. Benjamin Mcdowell and I conducted the density functional theory calculations. Benjamin Mcdowell, Motoaki Honda, and I analyzed experimental data. Benjamin Mcdowell and I analyzed theoretical data. I was the primary author of the paper that has not yet been submitted (as of November 1, 2021) and upon which this chapter is based, with assistance and guidance from George V. Nazin

6.1. Introduction

The interactions between a surface and adsorbate play a fundamental role in determining the electronic structure of the adsorbate. In many cases, it is desirable to decouple interactions between the adsorbate and surface in order to characterize, manipulate, or utilize material properties of the isolated adsorbate. To decouple these interactions, it is necessary to physically separate the adsorbate from the surface with an insulating layer.

The alkali metal halides are a natural choice for an insulating layer. They have a wide band gap,[1-3] sublimate in stoichiometric pairs,[4] form electrostatically neutral facets, [5] and, in the case of NaCl, readily form defect free crystals on Ag(100),[6-7] Ag(111),[6, 8-9] Al(111),[10-11]

Au(111),[12-16] Cu(100),[17] Cu(111)[18-20], Cu(311),[17, 21-22] and Cu(331).[23-24]

For these reasons, NaCl is commonly used as an insulating layer to decouple adsorbates from surface interactions. However, coupling of an adsorbate to NaCl has been shown to broaden electronic features by approximately 0.3 eV, which can completely obfuscate fine electronic features.[24] An alternative is RbI, which exhibits a decreased linewidth broadening of 0.15 eV.[24]

6.2. Background

RbI has previously been used as a dielectric in STM studies on Cu(331),[23-24] but to date no studies of RbI on Ag(111) have been reported. Furthermore, we are not aware of any study which has characterized the atomic structure of RbI in its monolayer form. It is important to characterize the atomic structure of materials in nanoscale applications, because reduced scale and dimensionality can lead to unexpected properties that may be completely different than the bulk behavior. Subtle changes in coordination may yield unexpected electronic or vibrational properties, and these changes can only be assessed at the atomic scale. It has been shown that reconstruction effects at surfaces can yield new properties, such as topological features,[25-28] localized states,[29-31] and charge redistribution,[32-35] among others. These changes can be especially impactful in the functionality of an insulating layer, since variations in electronic or vibrational structure may affect rehybridization or electron-phonon coupling processes with the

adsorbate. In turn, these may contribute to energy broadening of electronic features in the adsorbate.

To further investigate the efficacy of RbI as an insulating layer, we have characterized the atomic structure of its monolayer form. We identify the coexistence of two distinct phase types of the RbI monolayer, which differ in their coordination both within the adlayer and to the surface. Bistability of two phase types is unexpected and has not been previously reported for other alkali halide thin films. Evaluating the bistability of these two phase types yields a compelling perspective on the role of charge redistribution effects in surface/adlayer composite systems.

6.3. Methods

Experiments were carried out in a home-built ultrahigh vacuum (UHV) cryogenic STM system.[36] All imaging and spectroscopic measurements were carried out at 26 K using electrochemically etched silver tips. An Ag(111) single crystal was prepared in situ by using multiple cycles of Ne sputtering, followed by annealing. A sub-monolayer of RbI was deposited on to the Ag(111) surface (held at room temperature) via in situ sublimation in UHV conditions, then it is annealed at 40 °C for one hour and kept at this temperature until the sample has been transferred into the STM.

All computations were performed using density functional theory (DFT) as implemented in the Vienna Ab Initio Simulation Package (VASP).[37-39] a planewave code (with projector augmented wave (PAW)

scalar relativistic core potentials),[40] using periodic boundary conditions to approximate the infinite solids. To construct the Ag(111) surface, the lattice parameters of bulk Ag were optimized using the PBE functional for solids (PBE$_{sol}$),[41] with a 9 × 9 × 9 k-point mesh centered at the Γ point and a 500 eV planewave cutoff until all forces were less than 0.005 eV Å^{-1}. The resulting structure was then cut along the (111) facet, with approximately 25 Å of vacuum added to prevent interaction of periodic unit cells perpendicular to the surface. The trigonal RbI structure was optimized on three layers of Ag (with the bottom layer frozen to retain the bulk lattice constant), using a 5 × 5 × 5 k-point mesh centered at the Γ point and a 500 eV planewave cutoff until all forces were less than 0.005 eV Å^{-1}. Using the geometrically optimized structure, the HSE06 (PBEsol + 25% HF) functional,[42] was used to calculate the electronic structure at the Γ point, providing a more robust treatment of ranged interactions than PBE$_{sol}$. The size of the cubic unit cell (300 Rb,I atoms + 558 Ag atoms per layer) was prohibitive to performing calculations at the same level of accuracy, and was optimized on a single, frozen layer of Ag via the PBE$_{sol}$ functional at the Γ point with a 500 eV planewave cutoff until all forces were less than 0.05 eV Å^{-1} To allow for direct quantitative comparisons to be made between the two phase types, electronic structure optimizations were also performed via the PBE$_{sol}$ functional for the trigonal RbI monolayer on a single layer of Ag, using previously discussed parameters. All electronic structure calculations were

optimized until the change in energy between iterative steps was less than 10^{-8} eV. To characterize charge transfer between atoms, we used Bader analysis[43-46] with a vacuum cutoff of 10^{-3} electrons Å^{-3}, which kept all atomic volumes within 5% of the average for each atomic species. Visualizations of all structures were made using the VESTA package.[47]

To calculate the spatial and energy dependence of individual atomic contributions to the tunneling current, local density of states (LDOS) maps were interpolated using the Wentzel-Kramers-Brillouin[48] approximation. In this approximation the reduction in tunneling barrier height induced by the bias voltage is used to weight the LDOS of individual atoms as in Equation 6.1, where I is the tunneling current, E is an eigenenergy, r_i is the distance between the tip and an atom on the surface, V is the bias voltage, D_i is the a DOS for an atom on the surface, m is the mass of an electron, $\hbar$ is the reduced Planck's constant, and φ is the work function of the surface calculated by DFT.

$$I(E,r) \propto \sum_i \sum_E^V D_i(E) \times exp\left(-\frac{\sqrt{32mr_i}}{3\hbar V}\left[(\varphi - E + V)^{3/2} - (\varphi - E)^{3/2}\right]\right) (Equation\ 6.1)$$

6.4. Results and Discussion

Our STM results show that on Ag(111), RbI forms monolayers with a long-range order persisting over tens of nanometers (Figure 6.1a). We observe two distinct structural phases of the RbI, which are distinguished by the coordination of topographic features within the RbI monolayers (Figure 6.1b). In one of the two phases, STM images show

features locally coordinated in a "trigonal planar" fashion (left part of Figure 6.1b), while the other phase shows a "square planar" coordination (right part of Figure 6.1b). Intriguing, at high bias the STM topography is completely different for both RbI phases. The coexistence of such distinct structural phase types is surprising, since only a single phase type (analogous to the "square planar" phase observed here) has been previously reported by STM for other ultra-thin alkali halide structures. However, the existence of a NaCl structure analogous to the "trigonal planar" structure observed here has been shown to form on non-metallic substrates exhibiting a strong binding interaction.[49]
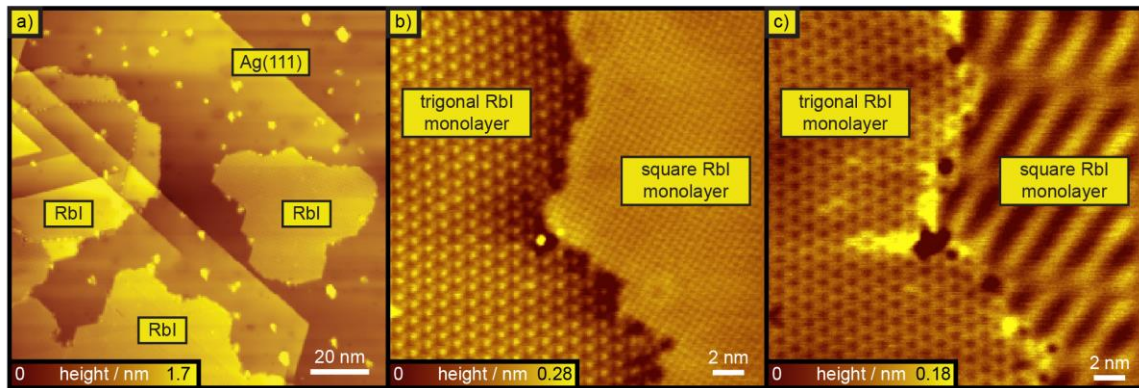
Figure 6.1: a) Large scale STM topographic image of sample surface, showing several RbI islands and Ag(111) step edges. b,c) Bias-dependent STM topography of domain boundary between square and trigonal RbI monolayers. Tunneling parameters: a) 300 mV, 10 pA, b) -200 mV, 200 pA, c) 2 V, 200 pA.

To understand the origins of the observed bistability of RbI on Ag(111), we first focus on the atomic structure of the "trigonal-planar" phase (trigonal in the following). The shortest distance between similar features is approximately 1.18 nm, allowing the trigonal monolayer to be

defined by the propagation of two lattice vectors forming an angle of 60°

(Figure 6.2a). Importantly, we find that the orientations of these vectors

are identical with different [110] crystal directions of the Ag(111) surface

(Figure 6.2b). Furthermore, the fact that the trigonal RbI islands show

regular unperturbed morphology over many unit cells of Ag(111), and

that the 1.18 nm periodicity observed for this phase is equal to four

interatomic distances of Ag, suggests that this phase has a structure

commensurate with that of Ag(111), as shown in Figure 6.2b. To further

identify the atomic structure of the trigonal phase, we turn to DFT

calculations. We have calculated a wide variety of test RbI structures

commensurate with the experimentally found supercell, with the most

common result being the calculated topography maps obtained at

voltages close to the Fermi level were always dominated by iodine atomic

orbitals, suggesting that the brightest protrusions in Figures 6.1b and

6.2a correspond to I anions. This interpretation is supported by the

changes in STM topography observed at high bias voltages, where the

contrast is inverted as seen in Figure 6.1c, in line with our DFT results

which show that at these voltages the tunneling current is dominated by

unoccupied Rb orbitals. We found it was insufficient to only have one

iodine atom and one Rb atom per unit cell in order to replicate the

trigonal RbI structures consistent with those observed in experiment. The

most energetically favorable structure calculated is that of Figure 6.2c,

where the average Rb–I distance is 5.2% longer with respect to the bulk

value of RbI (9.8% compressed with respect to lone RbI ion pairs in the

gas phase).
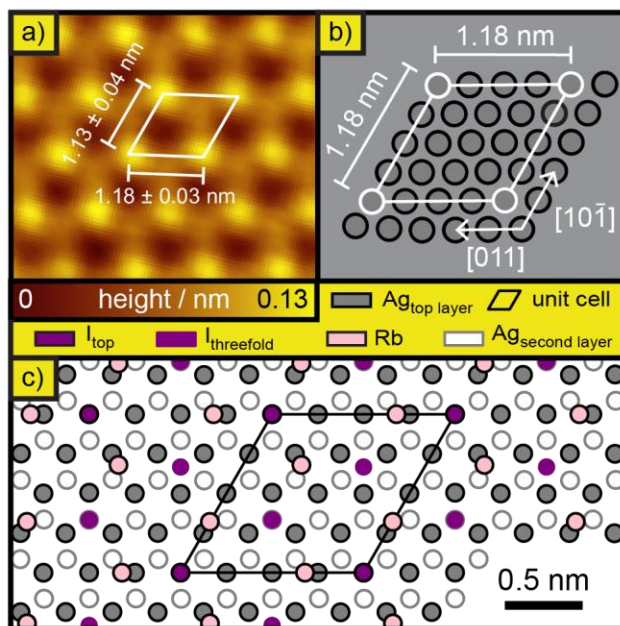
Figure 6.2: a) STM topography (100 mV, 30 pA) of a trigonal RbI monolayer. The overlaid dimensions reflect the average of 10 individual measurements. b) Atomic model of the Ag(111) surface, with the periodicity of the trigonal RbI monolayer overlaid. c) DFT calculated model of the pristine trigonal phase RbI structure.

The coordination of this RbI structure to the Ag(111) surface is

defined by the interatomic interactions at the RbI–Ag interface involving

local charge transfer and polarization. These surface charge

redistribution effects originate from the ionic character of the adlayer,

which interacts with the highly polarizable metallic surface. Charge

transfer occurs both within the adlayer and between the adlayer and the

Ag surface. Due to a larger ionic radius, the interaction of I anions with

the surface is stronger than that of Rb cations, leading, in particular, to a

greater degree of I–Ag charge transfer (as compared to that of Rb–Ag).

This is clear from the average net electron counts for each adlayer ion type: +0.659 electrons for iodide and -0.830 electrons for rubidium. In bulk RbI, the average net electron counts are +0.813 electrons for iodide and -0.813 electrons for rubidium, which indicates that iodide transfers 0.137 more electrons to the surface than rubidium on average. This can be visually illustrated by plotting the spatial electron density distribution (Figure 6.3a), which shows that there is more shared charge density between I anions and Ag atoms than between Rb cations and Ag atoms. This indicates that the interaction between the I anions and the Ag surface are the most significant in determining the energetics of the RbI monolayer. In order to qualitatively gauge the relative strengths of the RbI–Ag and Rb–I interactions, we plotted the difference between the electron density of the RbI/Ag system and electron densities of neutral Rb and iodine atoms, as well as the pristine Ag surface (Figure 6.3c). This electron density map shows that the strongest charge transfer is within the RbI monolayer, corresponding to the filling of the iodine p-orbitals, indicated by an increase in electron density in the directions of neighboring Rb (the diffuse decrease in electron density surrounding Rb indicates charge transfer out of their s-orbitals). However, the charge redistribution at the RbI–Ag interface is clearly significant, a consequence of both charge transfer and image charge formation.
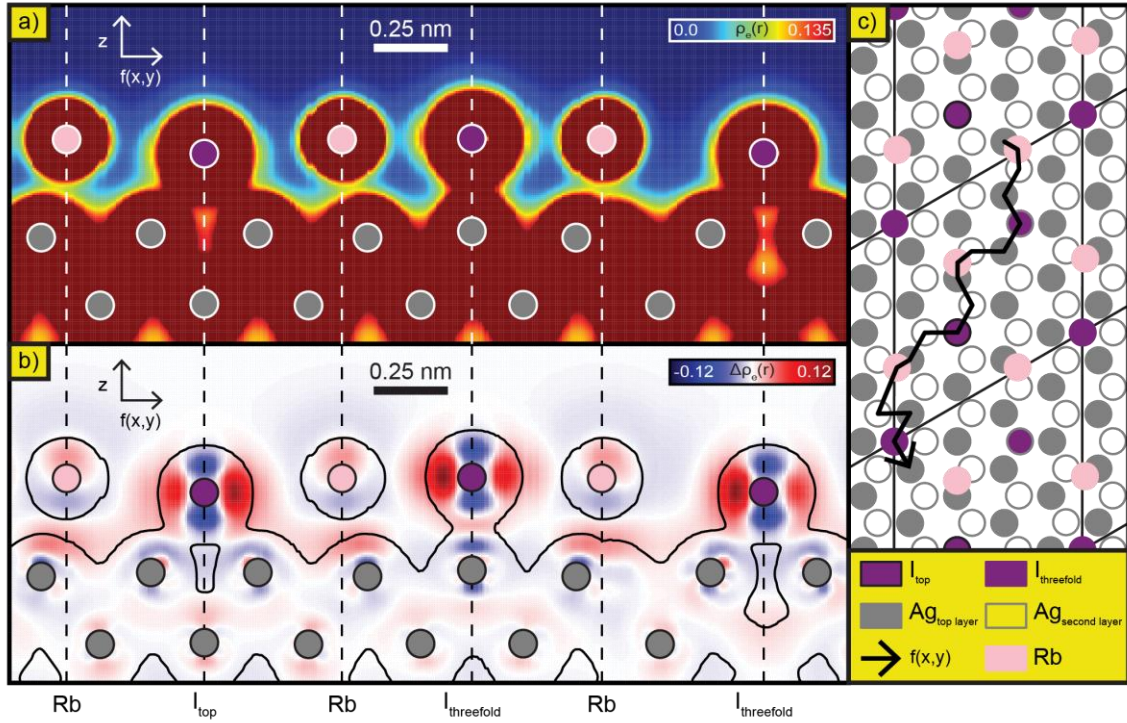
Figure 6.3: Depiction of the chemical interaction between a trigonal RbI monolayer and the Ag(111) surface. a) Total electron density sliced along the path shown in (c). b) Change in electron density due to interactions within the adlayer and between the surface and adlayer. The difference in electron density is calculated by subtracting the electron densities of isolated atoms in the adlayer and the pristine Ag(111) surface from that of the interacting RbI/Ag(111) system: $\Delta\rho_e = \rho_{RbI/Ag(111)} - \rho_{Ag(111)} - \sum\rho_{Rb} - \sum\rho_I$, where the sums are taken over each atom of the adlayer in isolation. The overlaid contour shows the total electron density at 0.135 electrons Å^{-3}. c) Atomic model of trigonal RbI monolayer, showing the path along which the electron density is sliced in (a) and (b).

Image charge formation, present both at the I–Ag and Rb–Ag interfaces

leads to more long-range interaction than that caused by charge transfer

(between iodide and Ag), which implies that the energetics of RbI

monolayers are more sensitive to the placement of the iodide (rather than

Rb) ions on the Ag surface. To qualitatively gauge the sensitivity of I–Ag

charge-transfer to the I and Rb placement on the Ag(111) surface, we

calculated the energies of individual I and Rb ions on a pristine Ag(111)

surface. Our results indicate that I anions strongly prefer the threefold hollow sites over directly on top of the Ag atom (top site), with a difference in energy of 0.44 eV between the two configurations. Despite exhibiting the same binding preference, Rb atoms favor the hollow site by only 0.06 eV, which confirms that the energetics of the RbI monolayer are more sensitive to the placement of the iodide. Guided by these results, we carried out calculations of several different RbI monolayers with similar three-fold symmetric structures, but with different coordination to the Ag(111) surface. The unit cell of the lowest-energy RbI structure found in these calculations ($I_{top\ site}$ in Figure 6.2c) contains two I anions at threefold hollow Ag(111) sites, consistent with our calculations for individual adatoms.

As a final test of the trigonal RbI monolayer structure, we calculated topographic images for each of the different RbI structures (Figure 6.4). Experimental STM topographies show an inversion of contrast as the bias voltage changes from 0.1 V to 4 V (Figures 6.4a, b). Among the different RbI monolayer structures simulated, only the one shown in Fig. 6.2c produced the same contrast reversal as the experiment (Figures 6.4a, b), as shown in Figures 6.4c,d.
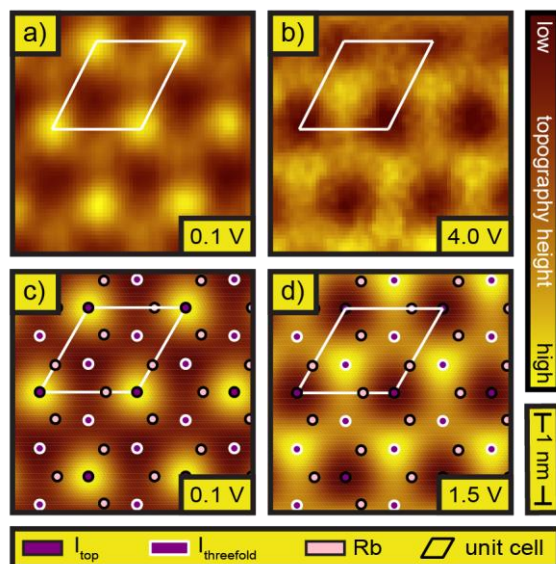
Figure 4: a,b) STM topographies (I=30 pA) showing an inversion of features between bias voltages of 0.1 and 4.0 V, white outline corresponds to smallest periodic unit of the trigonal phase RbI monolayer. c,d) DFT calculated LDOS maps integrated from the Fermi level up to 0.1 and 1.5 V, with the optimized trigonal phase adlayer and unit cell overlaid.

Analysis of the simulated images allows us to identify the origins of the observed contrast: at 0.1 V iodine states dominate the tunneling current, and the contrast originates from variations in the heights of I anions above the Ag surface, while at 4 V, the tip is further away from the surface, spatial resolution is reduced, and the STM images are dominated by the LDOS of the sample, rather than the corrugation. Variations in the heights of iodine atoms above the surface follows directly from their coordination to the Ag(111) surface (Figure 6.3a): the iodine directly on top of an Ag atom (I_{top}) has the largest height above the surface, while the two iodines in threefold coordination ($I_{threefold}$) sit deeper in a pocket of three Ag atoms. The difference in coordination for the threefold iodines lies in the second layer of Ag below the surface, as

the Ag atoms coordinated to the 'dark' ('semi-bright') iodine are coordinated to a total of 7 (3) other Ag atoms in the third row below the surface. Due to the higher relative coordination to the Ag surface, the Ag atoms bound to the 'dark' iodine propagate the image charge polarization more effectively, forming a strong image charge, and leading to a stronger attractive force on the 'dark' threefold iodine. Meanwhile, at larger biases, rubidium has the most unoccupied states, providing the most significant contribution to the tunneling current. The two threefold iodines each provide similar contributions to the tunneling current, while the top site iodine provides the least. In this energy range, Rb has the most unoccupied states, providing the most significant contribution to the tunneling current. The two threefold I anions each provide similar contributions to the tunneling current, while the top site I anion provides the least. This follows from a simple chemical explanation: the reduced coordination of the top-site iodide induces less splitting of atomic states and fewer unoccupied states available to contribute to tunneling, relative to those in the threefold hollow sites. There is no variation in the coordination of Rb^+ in the trigonal phase, meaning they have approximately identical LDOS contributions to the tunneling current.

We now move on to the structural characterization of the "square planar" (square in the following) phase type. At low bias voltages (right part of Figure 6.1b), the topography consists of approximately identical protrusions, which can be described by two orthogonal lattice vectors

oriented parallel ($S_{\bar{1}01}$) and perpendicular ($S_{\bar{1}2\bar{1}}$) to the [$\bar{1}01$] direction on the Ag(111) surface (Figure 6.5a). The protrusion spacing is on the order of the bulk RbI nearest same species neighbor distance (5.3 Å), which suggests that these protrusions are individual ions of the same species. As our calculations of the trigonal phase consistently show that the tunneling current is dominated by unoccupied iodine states at low voltage, it is likely that the protrusions are individual iodide ions. This interpretation is consistent with STM results of NaCl, where only Cl anions are imaged as protrusions at low bias voltage.[11, 17, 21] Intriguingly, the topography of this phase is dramatically different when sampled with a higher bias voltage (2V in Figure 6.5b), where the unit cell is an elongated rhomboid defined by two distinct lattice vectors (L_{short} and L_{long}) with an incident angle of approximately 79°. Based on our DFT calculations, we expect the tunneling current at this voltage range to be primarily affected by the LDOS of Rb ions. As a result, the significantly larger magnitudes of L_{short} and L_{long} relative to $S_{\bar{1}01}$ and $S_{\bar{1}2\bar{1}}$ suggests that the LDOS of Rb varies with respect to the Ag surface coordination. This finding can be explained by a moiré pattern, in which the LDOS of the Rb atoms varies with their registry to the Ag(111) surface. The existence of a moiré pattern is further supported by the orientation of the square phase with respect to the Ag(111) surface, as $S_{\bar{1}01}$ and $S_{\bar{1}2\bar{1}}$ are parallel to [$\bar{1}01$] and [$\bar{1}2\bar{1}$], but 80.1% and 4.0% longer respectively. This creates a lattice mismatch that is

commensurate with a periodicity defined by L_{short} and L_{long}, corresponding to approximately 5 and 30 Rb–Rb interatomic distances.
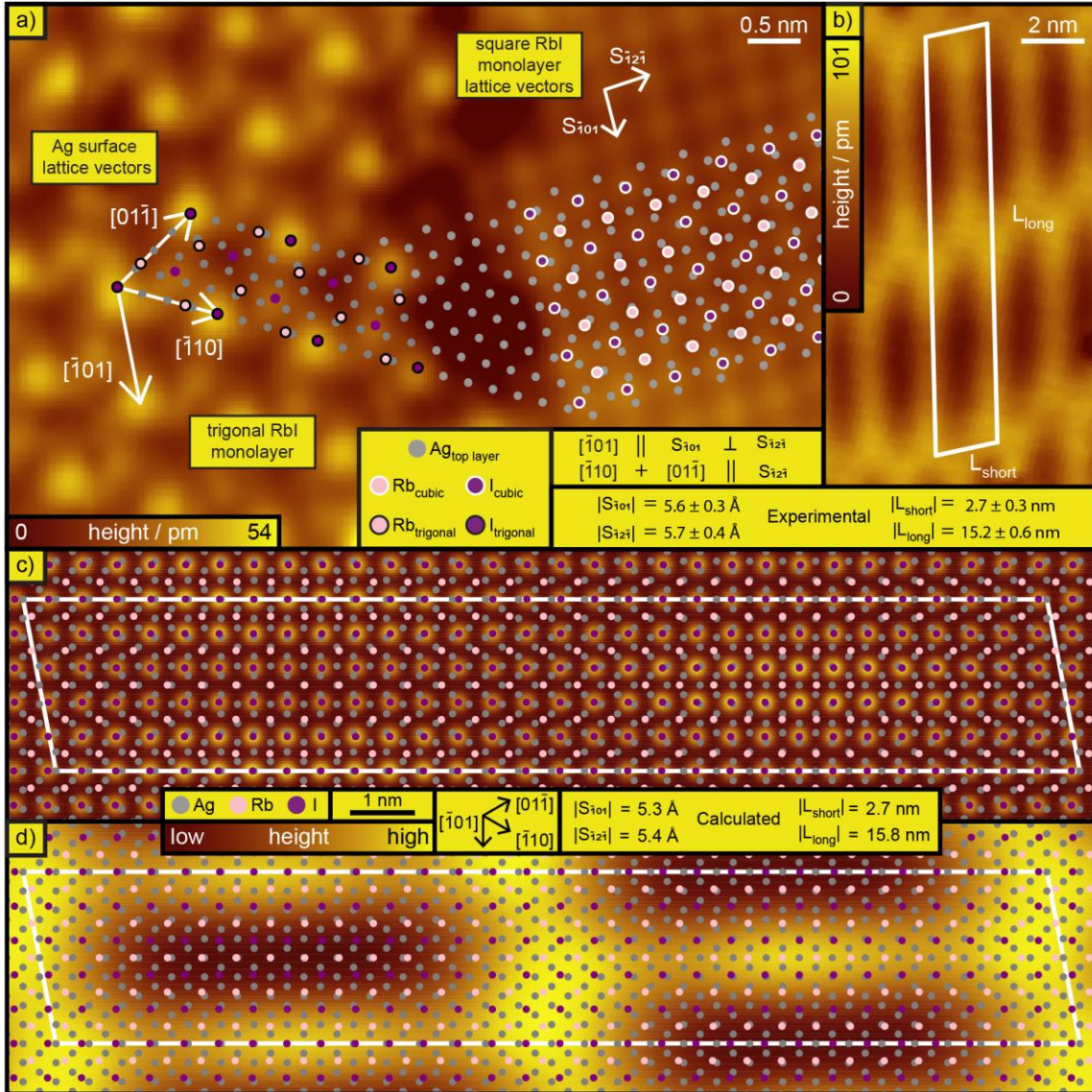
Figure 6.5: a) STM topography (-10 mV, -100 pA) of a domain boundary between trigonal phase (left) and square planar phase (right) RbI monolayers, showing the orientation of topographic features in each domain type with respect to the Ag(111) surface. The lattice dimensions shown in a,b are each the average of 10 measured values. b) STM topography (2.0 V, 10 pA) of a square RbI domain, with the DFT calculated unit cell of the moiré pattern overlaid. c,d) DFT calculated LDOS map of the square domain integrated up to 0.1 and 4 eV above the Fermi level, interpolated at distances from the surface of 5 and 25 Å respectively. The short lattice dimensions are an average of all atoms in the unit cell of the atomic model.

To further investigate the structure of the moiré pattern formed by the square phase, we have used DFT to optimize a variety of structures exhibiting square symmetry and the periodicity shown by L_{short} and L_{long}. The resulting structure (Figure 6.5c,d) reproduces the magnitudes of all experimental determined lattice parameters ($S_{\bar{1}01}$, $S_{\bar{1}2\bar{1}}$, L_{short}, L_{long}) to within the error of our measurements. Using this structure, we have simulated STM images at low and high bias voltages to compare to our experimental findings. At low bias (Figure 6.5c), the topography consists of protrusion features corresponding to individual iodide ions, which is consistent with our experimental findings. At higher bias (Figure 6.5d), our simulated topography yields elongated features similar to those observed in experiment. This provides a useful visualization of how the LDOS of Rb varies with registry to the Ag(111) surface: Rb ions have a larger LDOS and appear brighter due to a correspondingly increased contribution to the tunneling current when they are more highly coordinated to the Ag(111) surface. The elongated "dark" regions of the topography consist of Rb ions that are coordinated mostly to just one Ag atom, while the surrounding "bright" regions consist of Rb ions coordinated to two or three Ag atoms. This behavior is expected, as highly coordinated Rb ions will experience increased splitting of atomic orbitals relative to those with less coordination. We find this result to be consistent with the behavior of the LDOS in the trigonal phase.

We have shown that the behavior of the LDOS for both phase types is simply explained by the coordination of RbI to the Ag(111) substrate, and that this behavior dictates the monolayer topography at high bias voltages. We now extend this explanation to the band gap of the RbI monolayer, a value of functional significance for this material. To understand the band gap of both phase types and the phase transition, we used scanning tunneling spectroscopy to sample a one (spatial) dimensional LDOS map across a domain boundary separating the square and trigonal phase (Figure 6.6a). Our results show that the band gap is slightly smaller in the square phase than in the trigonal phase. The onset of the valence (Figure 6.6b, left) and conduction (Figure 6.6b, right) band appear approximately constant in the trigonal phase, with a band gap of approximately 7.6 eV. Contrastingly, the band gap of the square phase varies, with an average band gap of approximately 7.3 eV. To corroborate these experimental findings, we have estimated the average band gap (Figure 6.6c) for each monolayer phase by plotting a histogram of eigenenergies calculated by DFT. These calculations show that the band gap of the square phase is smaller than that of the trigonal phase. We find these results agree with our previous interpretations of the role of coordination in determining the LDOS of ions in the RbI monolayer, and can be qualitatively explained as follows. Each ion in the trigonal phase is coordinated to three of the opposite species within the monolayer (each Rb is coordinated to three I, and vice versa), resulting in the least atomic

splitting and the largest band gap. This trend follows for the square and bulk phases, in which each ion is coordinated to four and six of the opposite species respectively. The spatial variation of the band gap observed in the square phase results from variations in the registry of the monolayer with the Ag(111) surface. Since variations in the coordination of monolayer ions to the Ag(111) surface is much less dramatic in the trigonal phase, the band gap does not appear to vary spatially, or does so much less significantly than in the square phase. As these findings rely mostly on a simple chemical interpretation of the structural coordination, they may apply more generally to RbI structures grown on other substrates.
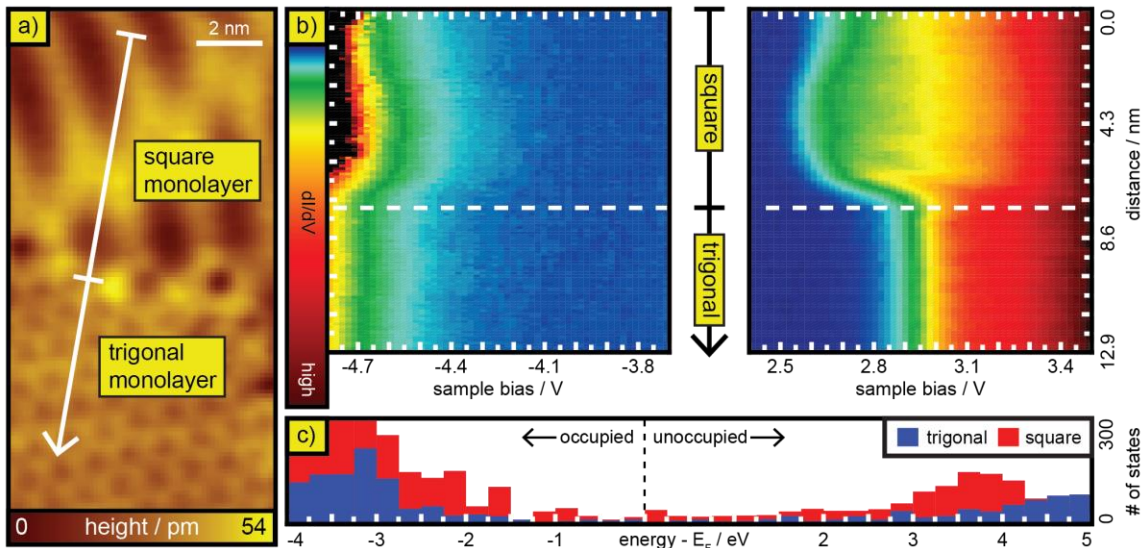
Figure 6.6: a) STM topography (V = 2 V, I = 100 pA) of a domain boundary between trigonal and square RbI monolayer phases, showing the STS line path for the spectra shown in (b); b) LDOS (measured as dI/dV) as a function of the bias voltage and position x along the path shown in panel(a). In panel b, the individual unoccupied and occupied LDOS spectra were normalized separately, for clarity.; c) Histogram of DFT calculated eigenenergies for the trigonal and square monolayer structures on Ag(111), depicting the reduced band gap of the square phase relative to that of the trigonal.

Finally, we discuss the origin of the structural bistability observed in the RbI monolayer. Fundamentally, the two monolayer phases have dramatically different planar atomic densities: ρ_{square} = 7.18 atoms/nm^2, $\rho_{trigonal}$ = 5.01 atoms/nm^2. We have calculated the binding energy of these structures to be 0.30 eV (square) and 0.54 eV (trigonal) per atom, indicating that the trigonal phase is energetically preferable. However, since the square phase is clearly prevalent despite exhibiting a smaller binding energy, we believe its presence to be related to the density of RbI ions on the surface. When the density of RbI ions on the surface is greater than the maximum planar density of the trigonal structure ($\rho_{trigonal}$), the trigonal monolayer phase can no longer be formed. In this case, there are two possibilities: 1) the RbI forms a bilayer of the trigonal monolayer; 2) the RbI reconstructs to the square phase. To test the likelihood of these possibilities we utilized DFT to optimize a double-layer form of the trigonal structure, which resulted in a planar density of 10.02 atoms/nm^2 and a binding energy of 0.21 eV per atom. This result suggests that it is energetically favorable for the monolayer to reconstruct to the square phase rather than to grow a second trigonal layer. However, it is also possible that, since these structures are kinetically trapped by the cryogenic conditions of our experiment, the binding energy does not offer a complete picture of the interactions that dictate single-layer growth of the RbI monolayer. In other words, as the

RbI monolayer is grown, the interactions between Rb and I may be more important than the Rb–Ag or I–Ag interactions (as shown in Figure 6.3). To test this, we examine the formation energies of the two monolayer phases in the absence of Ag(111) surface interactions, which shows that the square phase has a formation energy more favorable than the trigonal phase by 0.39 eV. This finding suggests that, as the density of the adlayer increases the interactions within the adlayer dominate, thus making the square phase more favorable. In conclusion, the bistability of the RbI monolayer can be explained by a combination of the binding energy of the monolayer to Ag(111) and the intra-adlayer interactions. Since the particular mechanism behind adlayer growth is beyond the scope of this work, we believe the density dependent reconstruction offers the best explanation a complete discussion of factors contributing to the bistability of the RbI monolayer.

6.5. Conclusion

We have identified and characterized two unique monolayer structures of RbI, which are structurally distinct from the bulk crystal. The bistability of these structures can be explained within the context of energetics, in which the structures observed in our experiment correspond to true potential energy minima. This behavior is drastically different than has been reported by STM for other alkali halides, in which only a single phase type was observed (similar to the square phase discussed here). The two RbI structure types yield different electronic

properties, which we find to be simply explained by differences in coordination and the resultingly proportionate extents of splitting this induces for the atomic orbitals of Rb and I. Due to the simplicity of this explanation, we expect this behavior to hold true for other strongly ionic structures grown on highly polarizable substrates. However, the bistability of phase types is also a unique result of the relative lattice constants for RbI and Ag(111), so we do not expect it to persist for all polarizable substrates.

6.6. Bridge to Chapter VII

We have determined the crystal structure and the surface atom coordination of a never-before-seen exotic crystal structure not found in bulk alkali halide crystals, and determined the origin of the how two distinct RbI crystal structures are simultaneously stable on the Ag(111) surface. We now turn our attention to how defects in a monolayer of RbI affect the electronic structure of the thin film, and what influence those defects have on carbon nanotubes (CNTs) deposited on top of the film. As CNT based devices are starting to leave university research labs and enter the realm of consumer devices, understanding the impact a dielectric interface has on the CNT electronic structure, and how any defects might adversely affect device performance is essential for future applications.

CHAPTER VII

IMPACT OF SUBSTRATE DEFECTS ON THE ELECTRONIC STRUCTURE OF SINGLE-WALLED CARBON NANOTUBES

The experimental work described in this chapter was conducted by Benjamin N. Taber, Christian F. Gervasi, and myself. Benjamen Taber, and I analyzed experimental data. I was the primary author of the paper that has not yet been submitted (as of November 1, 2021) and upon which this chapter is based, with assistance and guidance from George V. Nazin

7.1. Introduction

As electronic devices continue to shrink, silicon's limitations as a transistor channel material becomes increasingly more difficult to overcome. Due to their one-dimensionality, size, defined structure, and ballistic charge transport properties,[1-2] single-walled carbon nanotubes (CNTs) are a leading replacement channel material.[3] Many devices incorporating defect-free CNTs perform over an order-of-magnitude worse than their theoretical capability due to interactions between the SWCNTs and defects in the gate dielectrics and source and drain contacts.[1, 4-5] Understanding the impact of defects in the dielectric as well as the metal electrode on the CNT electronic structure is crucial for understanding single- and bulk-device behavior, but bulk experimental techniques are unable to resolve nanoscale interactions. STM can uniquely investigate the physical and electronic details of these interactions. Here, we use

STM to probe the physical structure and local density of states (LDOS) of CNTs adsorbed on both a dielectric and metal, as well as the LDOS of the substrate and its impact on the CNT LDOS. In these studies, monolayer RbI serves as a model dielectric and Au(111) serves as a model metal electrode for CNT-based devices.

7.2. Methods

Experiments were carried out in a home-built ultrahigh vacuum (UHV) cryogenic STM system.[6] All imaging and spectroscopic measurements were carried out at 26 K using electrochemically etched silver tips. A Au(111)/mica substrate was prepared in situ by using multiple neon sputter/anneal cycles. A sub-monolayer of RbI was deposited on to the Au surface (held at room temperature) via in situ sublimation in UHV conditions, then it is annealed at 40 °C for one hour. CNT(obtained from Sigma-Aldrich, >95% (carbon as CNT)) were deposited onto the RbI/Au(111)/mica substrate using the in-vacuum dry contact transfer method.[7-10]

7.3. Results and Discussion

RbI has previously been used as a dielectric in STM studies on Ag(111), and Cu(331)[11-12], but to date no studies of RbI on Au(111) have been reported. We observed that on Au(111), the RbI formed crystal islands of various sizes (from a few nm to tens of nm). The RbI formed single-layer crystals with a quasi-hexagonal pattern (Figure 7.1a) identical to the "trigonal planar" phase reported on Ag(111), and STS of

pristine RbI crystals (not shown) revealed a band gap of ~6.2 eV, in good agreement with the bulk.[13-15]

The Au(111)-(22 × √3) herringbone reconstruction was not observed through the RbI monolayer, unlike NaCl deposited on the Au(111) surface.[16] This suggests that either; 1) the interactions between the adlayer and the substrate cause the Au(111) substrate surface to reorganize out of the (22 × √3) configuration; or 2) the physical size of the ions in the adlayer and the intralayer interactions position the adlayer ions at a sufficient height above the substrate that the small (~0.15 Å) height differences in the herringbone structure do not affect the height of the adlayer considering the height difference between the protrusions and the depressions within the adlayer are (~0.30 Å). When NaCl is deposited onto a Cu(211) substrate, the Cu(211) surface will reconstruct, and NaCl will selectively grow only on the newly formed (311) facets.[17] Previous studies on molecular coverage have shown the removal of the Au(111)–(22 × √3) reconstruction with adlayer coverages as low as 0.25 of a monolayer.[18-20] DFT has been used to calculate the reconstruction energy and individual adsorbates (adatoms, sulfhydryl groups) decrease the reconstruction energy and will eventually remove the Au(111)–(22 × √3) reconstruction as coverage levels increase.[21]

It is therefore highly likely that the Au(111) surface has reconstructed into something other than the (22 × √3) structure in order to optimize interfacial lattice matching between the RbI layer and the Au.

It was shown that on Ag(111) when the RbI coverage is low it is energetically favorable to form the trigonal planar structure over the usual (100) terminated structure. Given the difference in lattice parameters between Ag (2.942 Å) and Au (2.950 Å) is only 0.27% the Ag(111) trigonal planar coordination to the substrate has been used, as STM parameters for atomic resolution were not found and DFT calculations have failed to converge. Follow up experiments with the Ag(111) substrate are currently being performed (1 November 2021). STS of pristine trigonal planar RbI on Au(111) (not shown) was featureless within the band gap similar to STS of pristine trigonal planar RbI on Ag(111). Further indicating the Au(111) RbI structure is very similar to the Ag(111) trigonal planar structure.

Of interest are the unique linear defects found in otherwise pristine RbI islands. The linear defects are aligned parallel to the <110> surface direction, they bisect the entire RbI island, only change directions by 120 °, and are found in both narrow and wide varieties, with a width of ~1 nm in the narrow part of the defect region, corresponding to approximately three bulk RbI lattice parameters (3.66 Å), and ~2 nm in the wide region (Figure 7.1a). STM topography imaging of the RbI crystal surrounding the faults revealed that the quasi-hexagonal pattern on either side was offset by approximately one-half of a hexagon, suggesting that the defects are anti-phase defects. Indicating that more than one

RbI crystal seeded and when they met the RbI in one of the crystals was offset by one row on the gold substrate, creating a grain boundary defect.
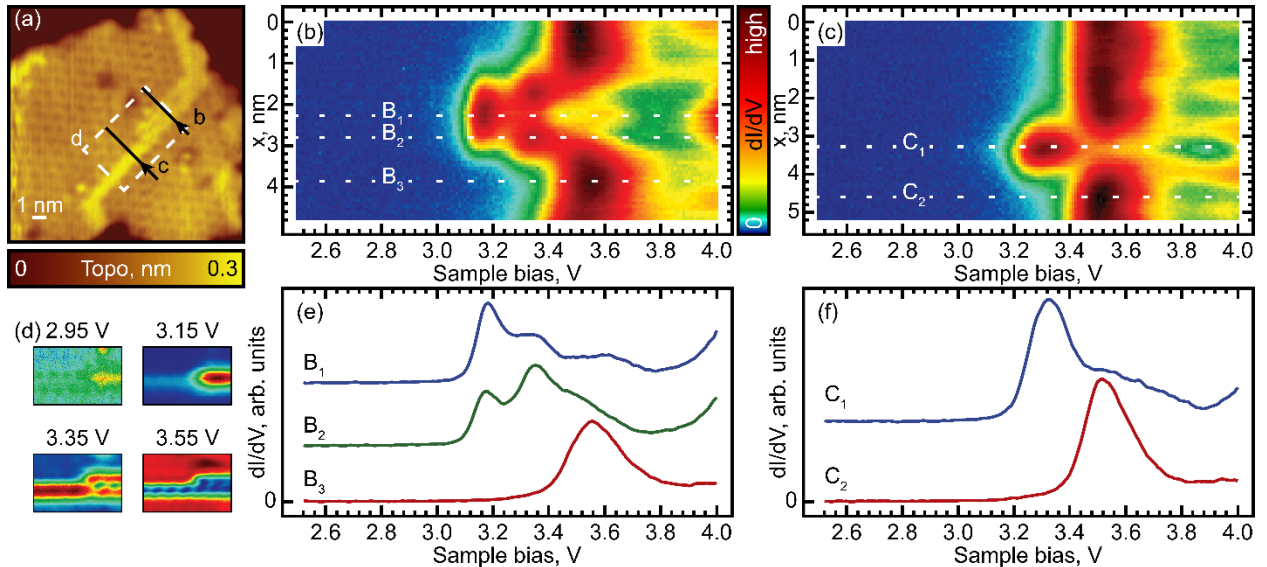
Figure 7.1. LDOS mapping of RbI grain boundary default. (a) STM topographic image. (b, c) LDOS (measured as dI/dV) as a function of the bias voltage and position x along the paths shown in panel a. (d) 2-D LDOS maps of the region in (a) outlined in the white dashed line. (e) Individual LDOS spectra from panel b measured at points B_1 through B_4. Spectra are offset for clarity. (f) Individual LDOS spectra from panel c measured at points C_1 and C_2. Spectra are offset for clarity.

One-dimensional (1D) LDOS mapping bisecting the "double-wide" anti-phase defect reveals states in the band gap just below the conduction band at ~3.15 V (one peak) and ~3.30 V (two peaks), with the pristine conduction band onset occurring at ~3.4 V (Figure 7.1b,e). By contrast, the "single-wide" anti-phase defect has only one sub-conduction band peak at ~3.3 V (Figure 7.1c,f). This difference in LDOS is further resolved by LDOS mapping in two spatial dimensions (Figure 7.1d), where individual nodes are both energetically and spatially localized within the defect region. In the 3.35 V 2D LDOS map isolated regions of depressed LDOS are found in a single row within the "single-

wide" section of the defect while within the "double-wide" area of the

defect the depressed regions are side-by-side. Of note is the LDOS

depressions within the "double-wide" defect are not aligned to the

depressions in the topography of the neighboring RbI, they are aligned

approximately 40 ° off axis relative to the depressions of the RbI located

to the left of the defect. Further supporting the grain boundary defect

assignment.
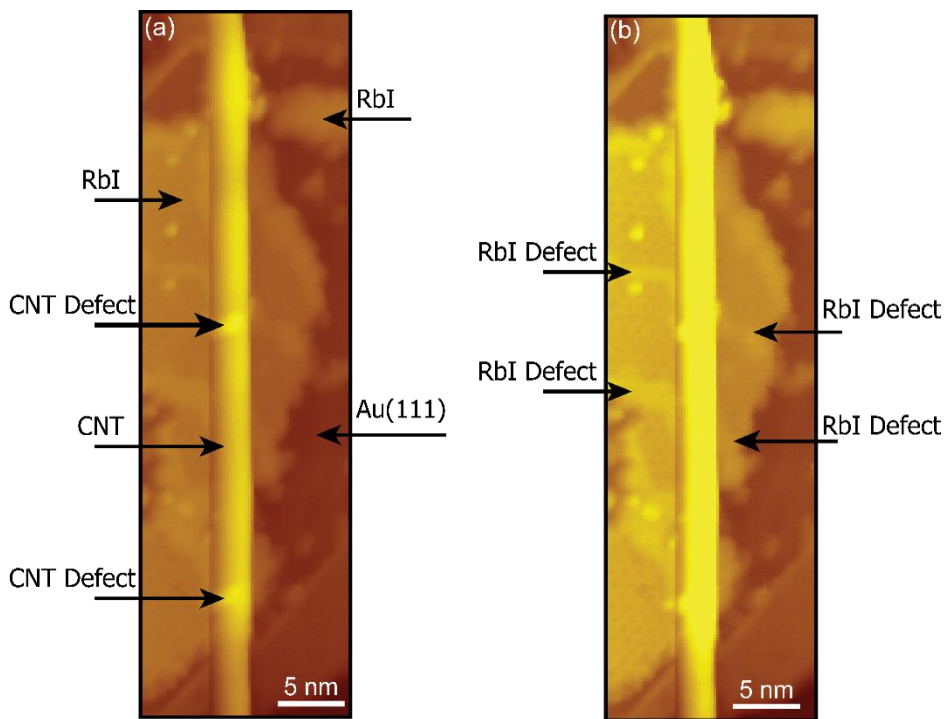
Figure7.2. (a) STM topographic image of a CNT adsorbed on a RbI island on Au(111), with noted CNT defects. (b) Enhanced contrast version of (a) with noted RbI "slip-stick fault" defects. Bias 1 V, 2 pA set point.

We investigated several CNTs adsorbed on both the RbI and

Au(111), but here we will focus on one particularly interesting example of

a CNT adsorbed across a monolayer RbI crystal (Figure 7.2). STM

imaging revealed that the CNT had two defects (likely Stone-Wales or

similar carbon coordination defects)[22] on the section of the nanotube adsorbed on the RbI crystal (Figure 7.2a). The RbI crystal contained defect-free regions separated by several linear defects, several of which crossed beneath the CNT (Figure 1b).

1D STS LDOS mapping of the CNT shows a correlation between the CNT local density of states (LDOS) and the topographic features of the RbI (Figure 7.3). 1D LDOS mapping of the RbI adjacent to the CNT (Figure 2b,d) reveals lower-lying unoccupied electronic states in the RbI linear defect regions (Figure 7.3 red lines, left side and yellow lines, right side; spectra adjusted to align to CNT LDOS map) as opposed to the defect-free regions. Interestingly, these RbI defect features correspond to particle-in-a-box (PIAB) -like features in the CNT LDOS (Figure 7.3c, green lines), with the spatial extent of the confining potential of the box approximately defined by the width of the RbI linear defect beneath the CNT. The LDOS of the CNT conduction band (0.7 V) is relatively consistent in the regions not immediately adjacent to the RbI defects, indicating there is only a weak electrostatic interaction between the CNT and the pristine RbI. There is some localized band bending of the conduction band as we travel from point D to point E, and this bending tracks very closely to the interface state in the RbI layer as shown in Figure 7.3c,d, same with the region between points F and G, indicating the defect states of the RbI grain boundary defect are clearly impacting the CNT LDOS. The valance band being at a minimum value (closest to

the fermi level) within the same regions (D to E and F to G) where the

conduction band is at a maximum (highest above the fermi level), is

indicative of periodic doping of the CNT,[9] most likely do to the RbI grain

boundary.
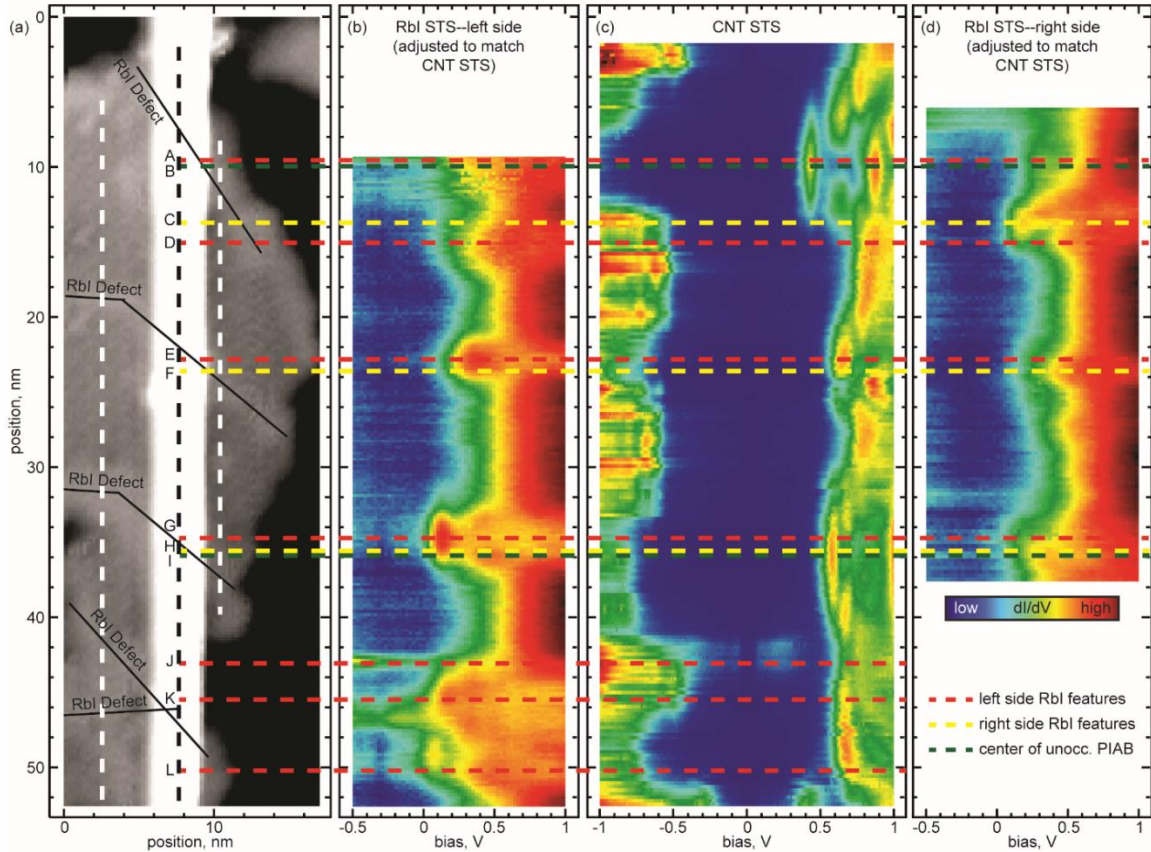
Figure 7.3: STS line scans along the length of a CNT adsorbed on RbI and along the adjacent RbI. (a) Grayscale STM image of the CNT adsorbed on RbI from Figure 1 with highlighted RbI defects (black lines). In order to better approximate the LDOS of the RbI beneath the CNT, RbI scans were adjusted down by 3.4 nm and up by 2 nm for the left and right sides, respectively, with the original paths of the RbI STS lines indicated by dashed white lines in (a). (b) Adjusted STS line of the RbI to the left of the CNT. (c) STS line scan of the CNT along the path indicated by the black dashed line in (a). (d) Adjusted STS line of the RbI to the right of the CNT. Red and yellow dashed lines correspond to observed features in the left- and right-side RbI scans, respectively, and the green dashed lines correspond to features in the CNT LDOS. 1 V bias set point for (b)-(d).

To further investigate the modulation of the CNT LDOS by the RbI, we performed 2D LDOS mapping of both the CNT and the surrounding RbI (Figure 7.4a), centered on the area denoted by lines G-I in Figure 7.3. Here, the RbI grain boundary defect acts as a confining potential, resulting in a PIAB-like feature in the unoccupied CNT LDOS (Figure 7.4b). This PIAB feature is more clearly observed with two-dimensional LDOS mapping (Figure 7.4c), where the RbI in the defect region shows enhanced LDOS at low bias (0.25 and 0.50 V) and the PIAB-like zero- and one-node features in the CNT LDOS appear at higher bias (0.55 and 0.675 V, respectively). Of note is the disorder in the CNT valance band starting just above point J, this appears to be the start of a section
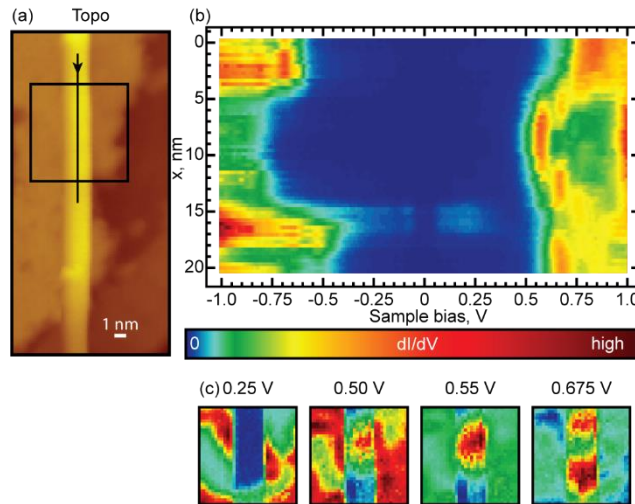
Figure 7.4. Spatial mapping of RbI grain boundary defect induced variations in CNT LDOS. (a) STM topographic image. (b) LDOS (measured as dI/dV) as a function of the bias voltage and position x along the paths shown in panel a. (c) 2-D LDOS maps of the region in (a) showing enhanced LDOS of the RbI in the defect region (0.25 and 0.50 V) and the corresponding localized zero- and one-node features in the CNT LDOS (0.55 and 0.675 V, respectively).

of the CNT either on the very edge of the RbI island or off the island and suspended above the Au substrate. The existence of a mid-band gap state at 0.1 V, and the accompanying shift in the valance band to ~-0.1 V could be due to charge redistribution at the RbI island edge caused by the Smoluchowski effect.[23-24]

The grain boundary defects in the RbI have a small height (~0.25 Å) difference as compared to the pristine trigonal planar structure. This raised region reduces the distance between the CNT and the RbI, much as the ridges in the Au herringbone (22 × √3) reconstruction have been shown to do.[5] This reduced distance leads to more electrons being transferred from the CNT to the RbI (and vice versa when the sample is negatively biased relative to the tip) in the region of the RbI grain boundary defect. The difference in lattice match between the CNT and the trigonal planar RbI versus the CNT and the RbI grain boundary is most likely different, and therefore the interaction between the CNT and the RbI is inhomogeneous, again changing the charge transfer characteristics of the CNT. As STS has shown (Figures 7.1 and 7.4) there is an increased LDOS within the grain boundary, both at voltages directly above the fermi level (Figure 7.4c) and just below the conduction band (Figure 7.1d). This increased LDOS acts as a localized interface dipole, [25] combined with the increased electron flow, the inhomogeneous charge transfer, can act as an energy barrier for charge carriers,[5, 25] and therefore create the PIAB-like states observed in the conduction band.

7.4. Conclusion

In this chapter we used STM/STS to investigate the effect pristine and grain boundary defects within a sub monolayer of rubidium iodide. When the CNT is adsorbed on the pristine region of the RbI there is only a weak electrostatic interaction and the wavefunction of the CNT is mostly decoupled from the Au/RbI interface state. On sections of the RbI monolayer with long-range linear defects the electrostatic interaction between the CNT and the RbI is much higher due to; a reduced distance between the CNT and RbI leading to increased charge transfer, an external dipole localized in the RbI defect, and inhomogeneous charge transfer. These results provide insight into the physical reasons why many CNT based devices perform so much worse than calculations predict. The physical crystal structure of the dielectric used in future CNT based transistors will need to be carefully chosen, to maximize the lattice matching, minimize the interactions between the substrate and the dielectric, while simultaneously minimizing any structural defects in the crystal lattice of the dielectric. Future studies on the interaction of CNTs on a variety of thin-film dielectrics will be needed.

7.5. Bridge to Chapter VIII

We now shift from experimental studies to the practical aspect of building a STM. The constraints that are placed on an instrument capable of achieving atomic resolution, of performing real space LDOS mapping, and most importantly being relatively user friendly are

numerous. In the next chapter we will describe the materials, the methods, and why each was chosen in fabricating the piezo-electric ceramic scanner that was used for the experimental work contained in this dissertation. We will also describe measures taken to isolate the system from any electromagnetic interference or radio frequency interference from sources internal and external to the STM itself.

CHAPTER VIII

MAGNETIC COUPLING STM SCANNER

8.1. Introduction

The Pan style design of our STM,[1] the choice of PZT-4 as the piezo-electric ceramic (piezo) for the scan tube, combined with the small diameter and thin walls of the piezo scan tube, means the piezo is structurally weak to any external lateral force exerted on the scan tube. The original design of the STM scanner (Figure 8.1) required the tips to be inserted laterally into a ceramic holder epoxied directly into the top opening of the piezo scan tube. The titanium tip stack shield has a small guide cut out that aligns the tip with the ceramic tip holder. If, when the tip is inserted through the titanium tip stack shield into the ceramic tip holder, the tip is slightly misaligned there is a good chance of breaking the piezo scan tube. If the handle on the tip holder is slightly askew the tip holder will be misaligned relative to the ceramic tip holder. The wobble stick used to manipulate items inside the chamber is directly coupled to atmospheric pressure and there is no pressure feedback when extending into the chamber, thus making it possible to apply a great deal of force onto whatever the working end of the wobble stick touches. The STM is designed to allow for Scanning Tunneling Luminescence experiments, which necessitates as much open space as possible in the bottom of the STM, eliminating the possibility of rigidly docking the

scanner assembly to eliminate the lateral forces present when exchanging a tip.
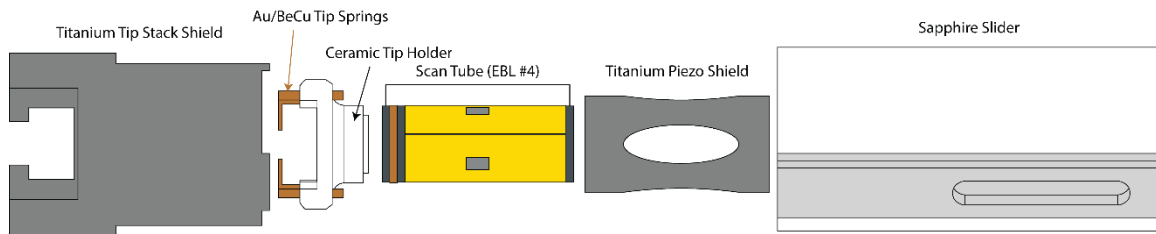
Figure 8.1. Exploded view of the original STM scanner assembly. Note: The titanium piezo shield (which is epoxied into the sapphire slider and surrounds the scan tube) has oval cut outs that align with the four quadrants on the scan tube to allow for making electrical connections to the piezo, the Ceramic Tip Holder is epoxied into the Scan Tube, and the slider has smooth sapphire faces (white) that are epoxied onto the alumina body (light grey), none of the wires are shown.

8.2. Magnetic Coupling System

I developed a magnetic coupling system (Figure 8.2) to mate the tip and the scan piezo in order to eliminate the lateral forces exerted upon the scan tube during tip exchanges. A magnetic coupling system was chosen for several reasons, with the most important considerations being, the design self-centers the tip, the magnets pull the tip vertically down into place thereby eliminating the lateral stress on the piezo scan tube, and the magnets ensure the tip has a good electrical connection with the preamp. Some of the secondary benefits of the magnetic design are, the addition of a shielding plane in between the scan tube and the tip, and improved shielding around the high voltage piezo wires in order to reduce any possible electromagnetic interference (EMI) or radio frequency interference (RFI).
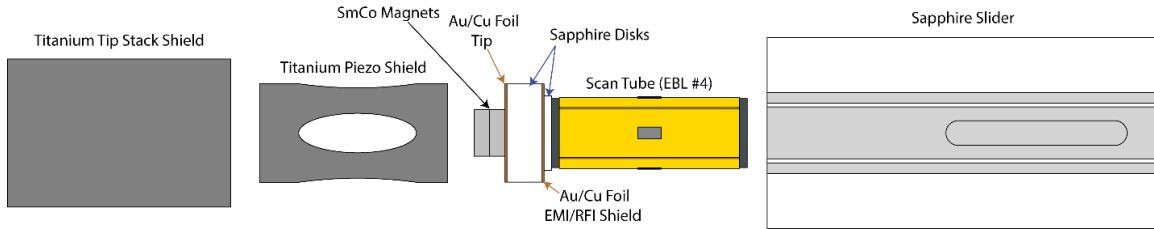
Figure 8.2. Exploded view of the new magnetic STM scanner assembly. Note: The titanium piezo shield (which is epoxied into the sapphire slider and surrounds the scan tube) has oval cut outs that align with the four quadrants on the scan tube to allow for making electrical connections to the piezo, the slider has smooth sapphire faces (white) that are epoxied onto the alumina body (light grey), none of the wires are shown.

The magnetic stack was designed so that a layer of EMI/RFI shielding was added to reduce any possible capacitive coupling between the tunneling current wire, the piezo and wires. Gold-plated copper foil was chosen for both the shielding and the tunneling current connections, as copper is easily formed, has a thermal expansion coefficient close to that of the sapphire insulators, is highly conductive ($\sim 6 \times 10^7$ S/m), and with the gold coating will not oxidize while curing the epoxy used in atmosphere. The EMI/RFI Au/Cu foil shield is electrically connected to the titanium piezo shield, the titanium tip stack shield, and connected to common on the STM controller. This is the only electrical connection to common for the STM controller as all other common connections for the STM are through a separate coarse approach piezo motor controller. Sapphire was used to electrically isolate the tunneling current connection from the shielding plane. Sapphire was chosen as the insulator as it is a good thermal conductor ($\sim 35 - 40$ W/(m·K)), has a

good dielectric constant, has a long history of being used in cryogenic systems, and is easily available in optically flat disks. I choose to use a thicker disk than necessary to reduce any possible capacitance between the shielding plane and the tip/preamp connection plane. Of note is that the optically flat disks have a very smooth surface and need to be "roughed" up to provide the epoxy with enough surface area to make a strong bond, I used 5 micron diamond sandpaper and a clean flat plane provided by the machine shop, each side of the sapphire disks only required a few seconds of sanding to roughen them up enough.

The structural connection between the scan tube and the magnetic stack was designed so that rather than have the bottom lip of the ceramic tip holder inside the hollow piezo scan tube, a small sapphire disk is epoxied on top of the scan tube. None of the magnetic stack extends down inside of the piezo scan tube, this ensures that any lateral force applied to the magnetic stack will cause the epoxy holding the sapphire disk to fail before the piezo scan tube breaks.

The electrical connection point between the wires leading to the preamp and the tip is the layer of gold coated copper foil directly connected to the Samarium Cobalt (SmCo) magnets. In the original design of the STM (Figure 8.1) the electrical connection between the preamp and the tip was a small titanium ball bearing in the scanner ceramic tip holder and a strip of gold on the bottom of the removable STM tip holder (his provided an unreliable preamp-tip connection which

required great care to determine if the tip was electrically connected and would intermittently fail requiring the reseating the tip and therefore increasing the chance of the piezo breaking). The SmCo magnets which are electrically conductive are epoxied to the center of the top layer of foil using an electrically and thermally conductive epoxy. The foil is epoxied to the sapphire disk using an electrically isolating and thermally conductive epoxy. The STM tips sit directly on top of the SmCo magnets creating an electrical connection between the tip and the preamp.

SmCo magnets were chosen over the other varieties of permanent magnets for several reasons. The STM operates at UHV conditions thus requiring all components be; UHV combatable, able to withstand high temperatures (~200 °C) bakeouts, function at cryogenic temperatures (~20 K), and have a coefficient of thermal expansion that is close to the rest of the components. SmCo are one of the strongest permanent rare-earth magnets, with only neodymium-based magnets being stronger. SmCo has a Curie temperature (700 – 800 °C depending on grade) much higher than that of neodymium-based magnets (310 – 400 °C depending on grade). SmCo magnets have better temperature coefficients than Neodymium, so they offer more stable magnetic fields over a wider temperature range. SmCo magnets have a proven track record of functioning at temperatures as low as 2 K and as high as 700 K, and in pressures ranging from 1×10^{-11} torr to greater than 1500 torr.[2-7] We used SmCo magnets coated with three layers, nickel, copper, then nickel

again, this prevents the sintered SmCo from fracturing, prevents corrosion, and improves the electrical connection between the tip and the preamp. Figure 8.3 shows the completed magnetic STM scanner assembly, note that the titanium tip stack shield is 1.0 mm short of the top of the SmCo magnets insuring the magnetic nickel tip holder cannot accidently make contact with the titanium shield.

The wire connecting the tip to the preamp is a very flexible coax cable with 38 AWG copper conductor wire and gold-plated copper braided shield with fluorinated ethylene propylene (FEP) as both the inner dielectric insulator and the outer dielectric sheath. The conductor is soldered directly to the Au/Cu foil the SmCo magnets are epoxied onto, and the braided shield is cut to prevent any electrical connections to the titanium tip stack shield or the tunneling current connection. Our STM control software uses single-ended measurements and as such any electrical noise is only on the tunneling current wire. The tunneling current wire runs along the exterior of the STM body (as do the high voltage piezo wires and the low voltage sample bias wire), to minimize any electrical noise from the nearby piezos as well as protecting the very thin FEP outer sheath I added a second layer of shielding, a bare silver-plated copper braided sheath, which is rigidly connected to the body of the STM providing an electrical connection to common, and is cut short to prevent any electrical connection to anything except the STM body.

117

Figure 8.3. Fully assembled magnetic STM scanner assembly. NOTE: The current design uses 38 AWG coax cable for the tunneling current wire, and not the 34 AWG twisted pair visible in this picture.

The new magnetic scanner assembly design necessitated a complete redesign of the STM tip holders. The new tip holders (Figure 8.4) are laser cut from 0.005" nickel and folded into the final shape. The sockets that hold the silver tip are gold flash over nickel, with a beryllium copper spring. The sockets are soldered to the nickel tip holder to provide a solid electrical connection between the tip and the magnets, this process will change to laser welding in the near future, which will remove the temperature limitations inherent in soldered connections. Nickel was chosen as it is ferromagnetic, has a very high melting point, has a high Curie temperature, high electrical conductivity, good thermal conductivity, is both corrosion and oxidation resistant, and is both strong yet malleable and ductile. The new tip holders are easier to fabricate, structurally stronger, make better electrical connections, and are less expensive than the original ceramic body tip holders.
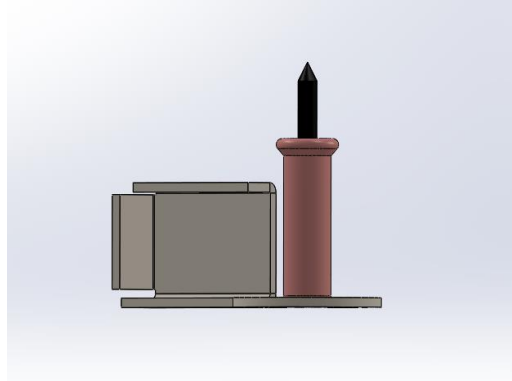
Figure 8.4. 3D model of the magnetic STM tip holder. The handle is 0.005" Ni, the socket is Au over Ni with a BeCu spring, and the tip is 0.5 mm diameter polycrystalline Ag. The total length of the tip holder is 0.32", the inner height of the handle is 0.112", and the height of the socket is 0.178".

The new nickel magnetic STM tip holders required that a number of UHV chamber items be completely redesigned; the precision magnetic manipulator used to exchange samples and tips between the load lock and the main UHV chamber; the "carousel" module inside the main chamber used to store samples (mounted on molybdenum sample holders) and tips; and the "heater" a multifunctional processing module. These modules required machined parts with ceramic tip holder slot cutouts be replaced with new machined parts with SmCo magnets.

8.3. Tunneling Current Noise Reduction

The magnetic STM scanner assembly was designed to not only make it safer and easier to replace the tip, but it was also designed to be less susceptible to EMI/RFI. To complement the new scanner assembly, numerous additional EMI/RFI reduction measures were taken to reduce interference from the electronic equipment in the STM room. The STM control hardware and the various electrical vacuum equipment (turbo

controllers, ion gauge, ion pump, etc.) are powered by an on-line double-conversion UPS. We found that with the STM controller connected to the UPS the electronic noise in the tunneling current was higher (~2.5 pA at 2 kHz) than when the controller was connected directly to the wall outlet (~1.5 pA at 2 kHz). I found that the isolation transformer built into the UPS was allowing electrical noise on the neutral line (not the hot or the ground lines) through to the STM control electronics. To eliminate the noise from the buildings electrical system both a new on-line double-conversion UPS, and most importantly a separate ferroresonant isolation transformer was installed between the STM control electronics and the new UPS.

A layer of grounded interference-shielding sleeving and conductive copper foil electrical tape were added to the following: the first stage preamp, the second stage preamp, the cable running between them, the cables running from the second stage preamp to the STM controller, the high-voltage cables running from the STM controller to the UHV feedthroughs for the scanner assembly, and the high-voltage cables running from the coarse approach piezo motor controller to the UHV chamber.

In addition to the measures taken to reduce the EMI/RFI interference from outside the UHV chamber measures were taken to reduce the interference from sources within the chamber. Along with adding a layer of EMI/RFI shielding into the piezo scanner assembly, the

high voltage twisted pair wires that run along the exterior of the STM to control the: coarse approach piezo motors, the sample alignment piezo motor, and the tip cylinder scanner piezo were routed through silver-plated copper braided shields, which are grounded directly to the body of the STM. The low voltage sample bias wire was also routed through a silver-plated copper braided shield to reduce the capacitive coupling with the sample alignment piezo motor, note that both the low voltage sample bias and the high voltage piezo motor wires are independently shielded. The electrical connections on the STM thermal shields were rearranged so that there was physically as much distance as possible between the connection points for the tunneling current wire, the sample bias wire, and the high voltage wires.

If the tip is outside of tunneling range, the sources of noise in the tunneling current should be purely electrical in nature due to ground loops, capacitive coupling, improper shielding, and the like. With the tip within tunneling range and the z-piezo feedback off, not only will electrical noise sources be present, but mechanical and acoustical sources will appear in the tunneling current as any variations in the tip-sample separation distance will not be corrected by the control software. With the EMI/RFI reduction measures in place at room temperature with the tip outside of tunneling range the peak-to-peak (pk–pk) amplitude of the tunneling current for the original design of the STM scanner assembly was approximately 3 pA, while for the new magnetic design the

pk–pk of the tunneling current is approximately 0.75 – 1 pA. At cryogenic temperatures with the tip within tunneling range on a clean Au(111) – (22 × √3) surface with 1 V sample bias and 20 pA set point (a typical setting for performing constant current topographies) the pk-pk for the original scanner was approximately 2 pA, while the magnetic design has a pk-pk of approximately 1 – 1.5 pA.

To quantify the difference between the original design of the STM scanner assembly and the magnetic design, fourier spectra of the tunneling current were (Figure 8.5) taken on a clean Au(111) – (22×√3) surface with 1 V sample bias and 20 pA set point at cryogenic temperatures shows an order of magnitude decrease in all sources of noise between the original design of the STM scanner (blue), and the new magnetic scanner assembly (red). This drastic reduction in noise in the tunneling current will allow for improved STS measurements by improving the signal-to-noise, reduce the integration time necessary for individual STS measurements, and give us the ability to perform inelastic tunneling $\left(\frac{d^2 I}{dV^2}\right)$ spectroscopy.
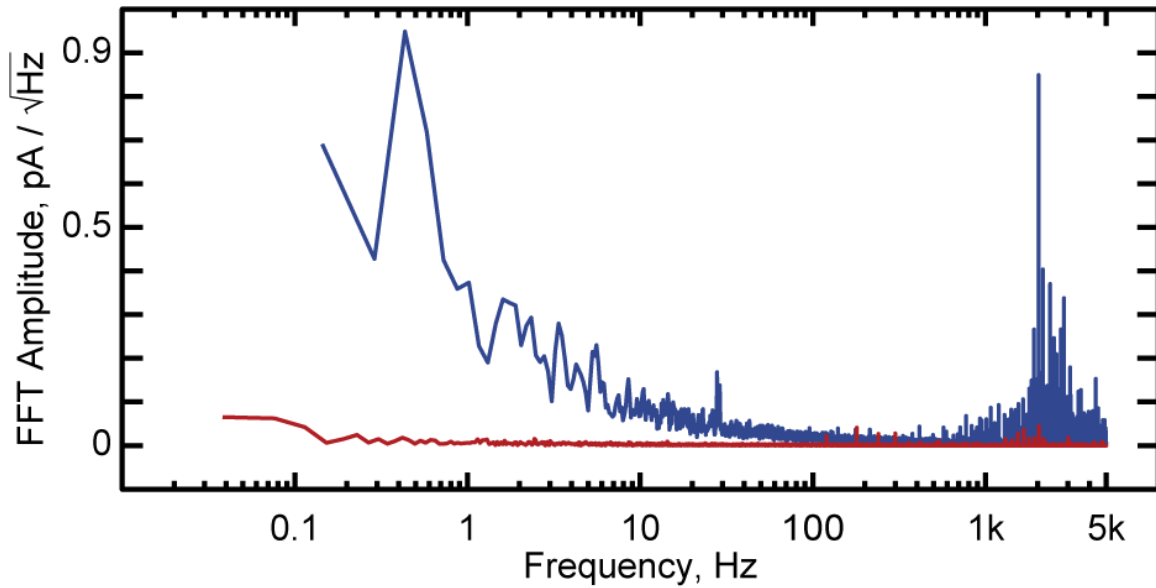
Figure 8.5. Fourier transform of the tunneling current showing the external mechanical/acoustical/electronic noise present in the tunneling current using, the original design of the STM scanner assembly (blue), and the new magnetic design (red). Maximum noise for the original design was 0.95 pA/√Hz at 457 mHz with the second highest being 0.85 pA/√Hz at 2.0 kHz. Maximum noise for the magnetic design was 65 fA/√Hz at 38 mHz with the second being 45 fA/√Hz at 2.0 kHz. Measurement conditions: tunneling set point 1 V at 20 pA, cryogenic temperatures 16 K (blue) 22 K (red), with the z-piezo feedback turned off.

CHAPTER VIII

CONCLUSIONS AND PROSPECTS

Nanomaterials are already starting to be incorporated into consumer electronics (quantum dot TVs), carbon nanotube field-effect transistors are starting to be fabricated by the research arms of the major commercial companies. As we continue to transition to smaller and smaller electronic devices understanding the effect atomic defects have on the electronic structure, and therefore charge transport and device performance, is the only way to engineer future technological progress. Devices are already small enough that quantum tunneling is affecting device performance, and the transition from dielectrics such as silicon dioxide to the exotic dielectrics, can only buy us so much time. The work contained in this dissertation used scanning tunneling microscopy and spectroscopy (STM/STS) to "see" the real space effect atomic scale defects have on the electronic structure of low-dimensional materials.

First, we examined hydrogen terminated silicon nanocrystals (SiNC). We found that the exposure to trace amounts of oxygen caused oxidation defects. These defects not only produced localized electronic states, but they also produced states that were delocalized throughout the entire SiNC. We used density functional theory (DFT) calculations to determine the oxidation defect was caused by either a single oxygen atom bridging between two silicon atoms(Si–O–Si), or hydroxyl group attached

124

to one silicon atom (Si–OH). Most importantly this study showed the very first steps in the silicon oxidation process.

STM was then used to remove individual hydrogen ligands from the SiNC surface. This caused the SiNC surface to initially reconstruct which cause a reduction in the band gap. As more hydrogen ligands were removed, midgap states deep in the band gap appeared, using DFT these states were attributed to dangling bonds on the SiNC surface. These dangling bonds were capable being charged and discharged repeatably. These findings provide a direct visualization of possible scenarios for defect generation in SiNC-based optical and opto-electronic devices, where surface defects could be created by photo-generated charge carriers with sufficient energies.

In the final experiment on SiNCs we turned to SiNCs with bistable electronic states. We used real-space two-dimensional STS mapping to determine the location-dependent voltage onsets of the band edge states and show the onsets fluctuate across the surface, unlike crystalline SiNC where the band onset is independent of location. A common defect in SiNCs is the presence of an amorphous thin (angstrom scale) surface layer on an otherwise single crystal SiNC. STM topographies showed SiNCs without any obvious crystallographic features, unlike SiNC's in previous studies. Through a combination of varied energetics of bistable electronic states, the varied spatial form of the intra band gap states, and the alignment with theoretical models for amorphous silicon, we showed

charge carrier self-trapping causing local structural changes within the SiNC.

We then turn from zero-dimensional nanocrystals to the study of a two-dimensional (2D) material. A model alkali halide dielectric was chosen as they are a well-known material and are widely used in STM as a method to decouple an adsorbate from the conductive substrate. We use rubidium iodide (RbI) as the model dielectric and using STM and STS we show, for the first time, a bistable crystal structure with one of the crystal structures a never-before-seen type not found in the bulk RbI crystal. The two crystal structures yield different electronic structures and

We then turn to an investigation of defects in the 2D layer of RbI on Au(111) and how those defects influence a carbon nanotube, a one-dimensional (1D) material, deposited onto both the metal substrate and the 2D layer of RbI. Using STM and STS we explore the impact of the defect on the electronic structure of the CNT. We correlate the intra band gap states in the CNT directly to crystal defects in the underlying dielectric. These results provide key insights into the impact external defects have on the electronic structure of CNTs.

We finally end with a description of the materials and methods used to fabricate an upgraded pan-style STM scanner assembly. We go into detail on why the radical redesign was necessary and the benefits of the redesigned assembly. We end by quantifying the reduction in

tunneling current noise. The recently updated STM is ready for the next generation of STM experiments, tip-enhanced raman spectroscopy, STM induced photoluminescence, near-field optical spectroscopy, and inelastic tunneling spectroscopy, all of which require an instrument with low frequency vibrations, low thermal drift, and very low electrical noise.

APPENDIX A

SUPPORTING MATERIAL FOR CHAPTER III
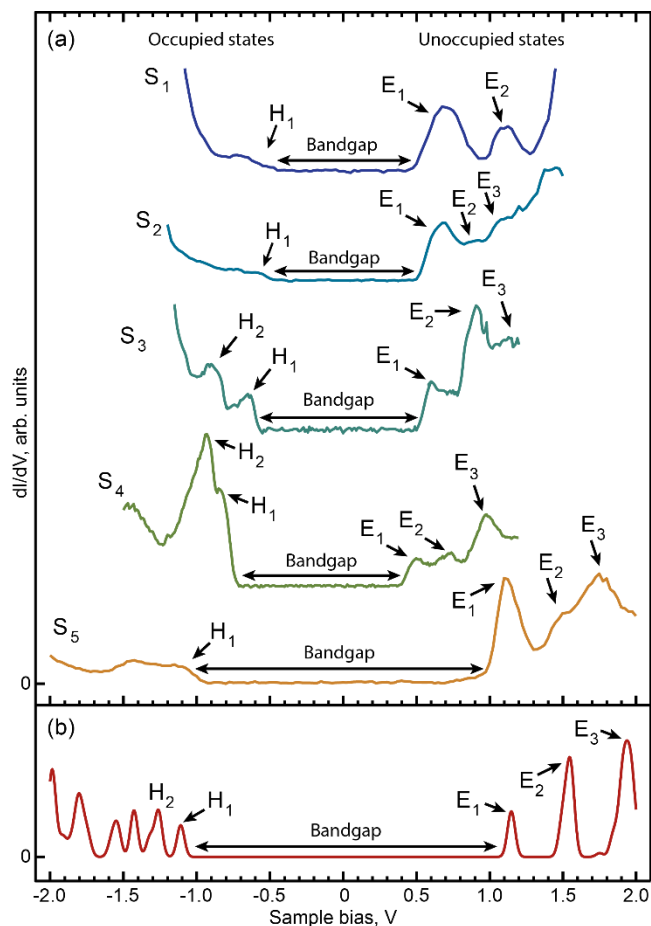
Figure A.1. Scanning Tunneling Spectroscopy of SiNCs. (a) Representative DOS spectra for five different SiNCs (Set point voltages and currents range from 1.0 V to 1.5 V, and 5 pA to 10 pA for the spectra shown). (b) Calculated DOS for a model with size comparable to a NC featuring spectrum S_5 from (a). Occupied and unoccupied states are indicated by arrows and marked with an 'H' and 'E' for holes and electrons respectively.
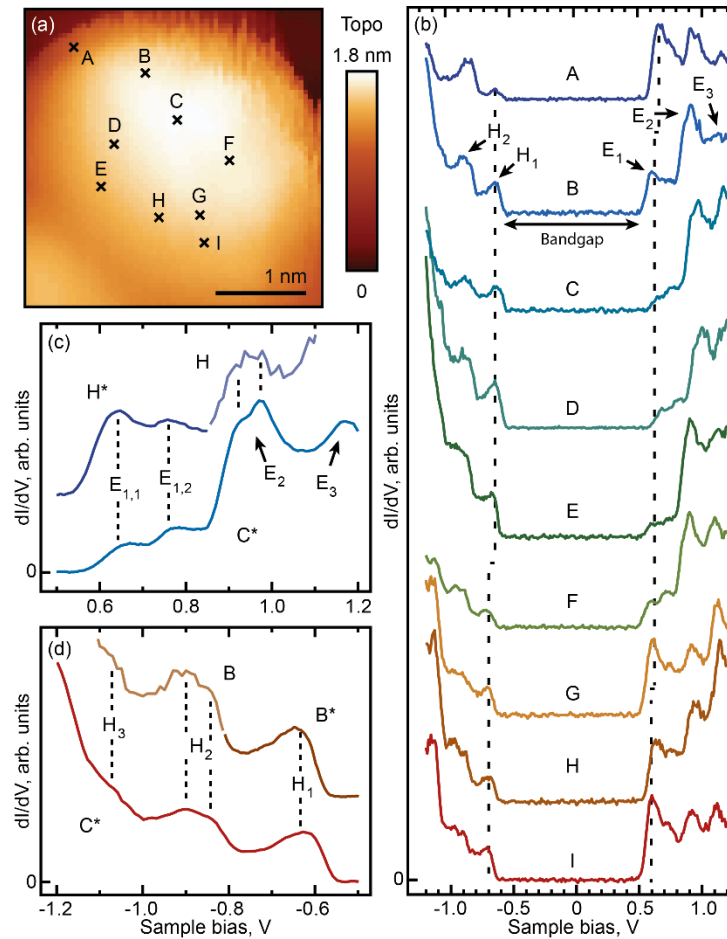
Figure A.2. STM/STS characterization of NC_1. (a) STM topography image of NC_1 [set point 1.2 V, 5.0 pA]. (b) STS spectra [set point 1.2 V, 10 pA] measured at the locations A-I marked in (a). Spectra are offset for clarity. Prominent occupied and unoccupied states are marked with an 'H' and 'E' respectively. Individual DOS peaks are observed at slightly different voltages across the NC due to the finite location-dependent voltage drop inside the NC. (c-d) Close-up of spectra from B, C and H locations showing finer structure (spectra marked "*" were acquired with better signal-to-noise ratio by using longer acquisition times).
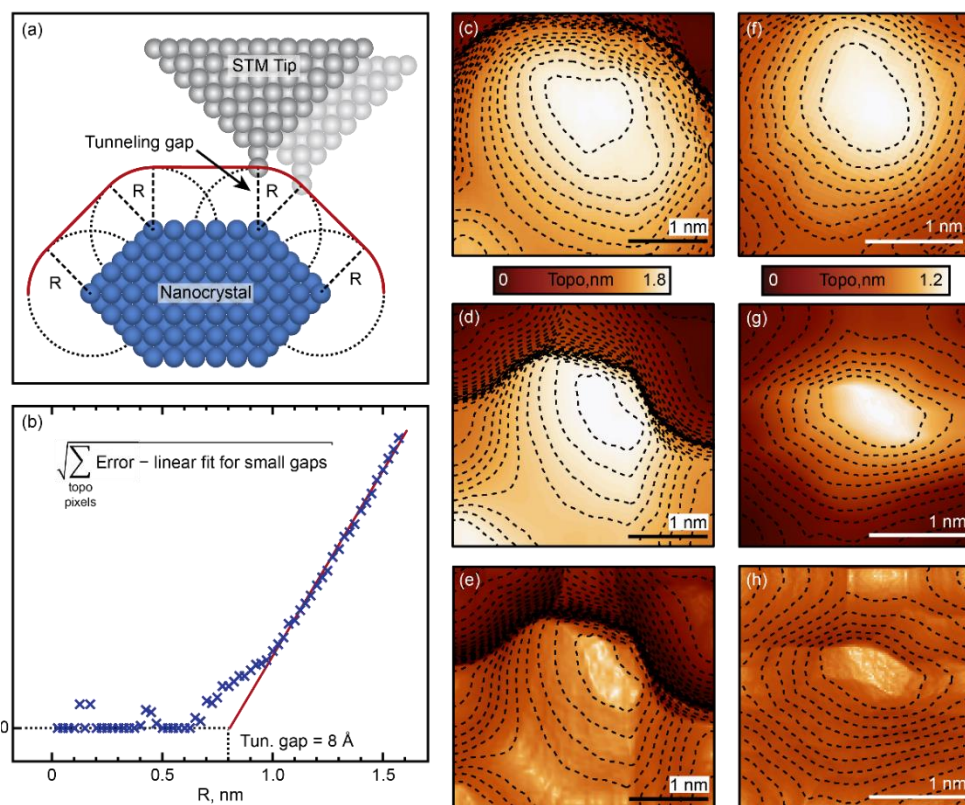
Figure A.3. Reconstruction of the NC shape from STM topography. (a) Trajectory of a STM tip over a three-dimensional object when scanned in the "constant tunneling current" regime typically used for STM topography. Apparent object shape is enlarged and sharp features are rounded due to the finite tip-sample distance and the possibility to tunnel sideways. Additional broadening occurs, in a similar fashion, due to the finite dimensions of the tip apex. Both effects can be accounted for (in the first approximation) by assuming that the tunneling current only depends on the distance (defined in three dimensions) between the tip apex and object of interest. This is equivalent to assuming that the tip wavefunctions have an approximately s-orbital nature at the tip apex, a common approximation in theoretical calculations of STM images. If the tip-object separation R is known [see (a)], then a model of the actual object shape can be calculated by constructing a 3D surface that consists of points located at identical minimal distances R from the experimental topographical surface [see (a)].

The calculation can also be reversed and a model of the STM topography can be recalculated from the calculated NC shape. The difference between the experimental STM topography and recalculated STM topography can be used as a measure of the accuracy of such a representation. The accuracy is affected by the noise in STM topography, and the value chosen as R. For example, if R is smaller than the characteristic dimensions of all features in the STM topography, the error is zero. If features with dimensions smaller than R are present in the

STM topography, then they may not contribute to the model of real NC shape, and may be lost in the recalculated STM topography, thus adding to the error. This means that when R is smaller than the actual gap (usually on the scale of several angstroms), the error is mostly dominated by the topographic noise and atomic-scale features. However, once R exceeds the real tunneling gap (the latter defines the curvature of the features in STM topography), an additional component of the error, caused by the mismatch between the true and calculated NC shapes, becomes non-zero. It is easy to show that the dependence of this error component on R is quadratic. In order to find the best fit to the real effective gap, we calculated the described error using different values of R, and found that at small values of R (where noise dominates) the dependence is linear [see (b)]. By subtracting this component from the error and plotting its square root as a function of R, we found that at higher R the dependence is linear, in accordance with the geometric considerations. A linear fit to this function allows us to find the best approximation to true R, as shown in figure (b).

(c) Experimental STM topography of NC_1 with its contour lines overlaid. (d) Calculated shape of the NC_1 using R=0.8 nm. Top facet of NC_1 was found to be flat and almost horizontal. (e) Model of NC_1 digitally processed to "sharpen" the features (pseudo-3D rendering). (f-h) Same as (c-e) for the NC_2.
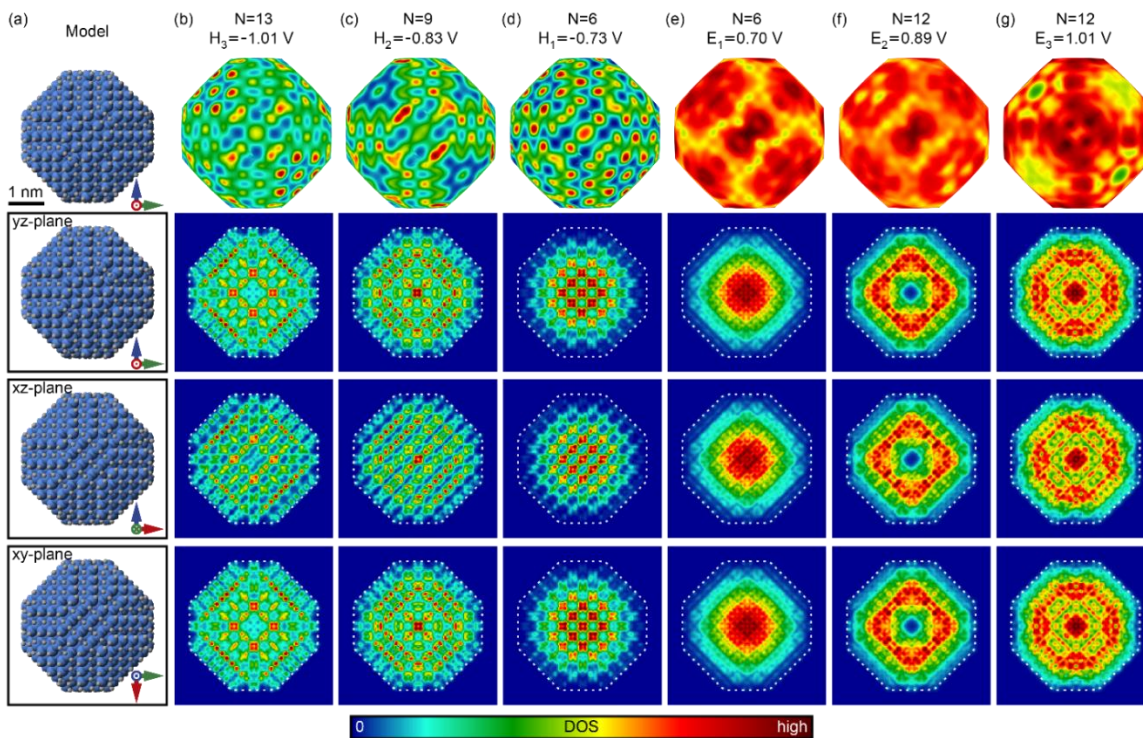
Figure A.4. Volume distribution of theoretical DOS for a model near-spherical (composition $H_{412}Si_{1087}$, diameter ~3.5 nm) SiNC without impurities. (a) NC geometry. (b-g) DOS for the peaks from Figure 2c. N is the number of individual states comprising the peak. First row represents the normalized DOS maps on the surface (identical to Figure 2e-j). Second, third, and fourth rows show bulk unnormalized DOS distributions across the main coordinate planes going through the center of the SiNC. Each displayed DOS datapoint was averaged over a 3.6 Å-long segment orthogonal to, and bisected by the corresponding plane.
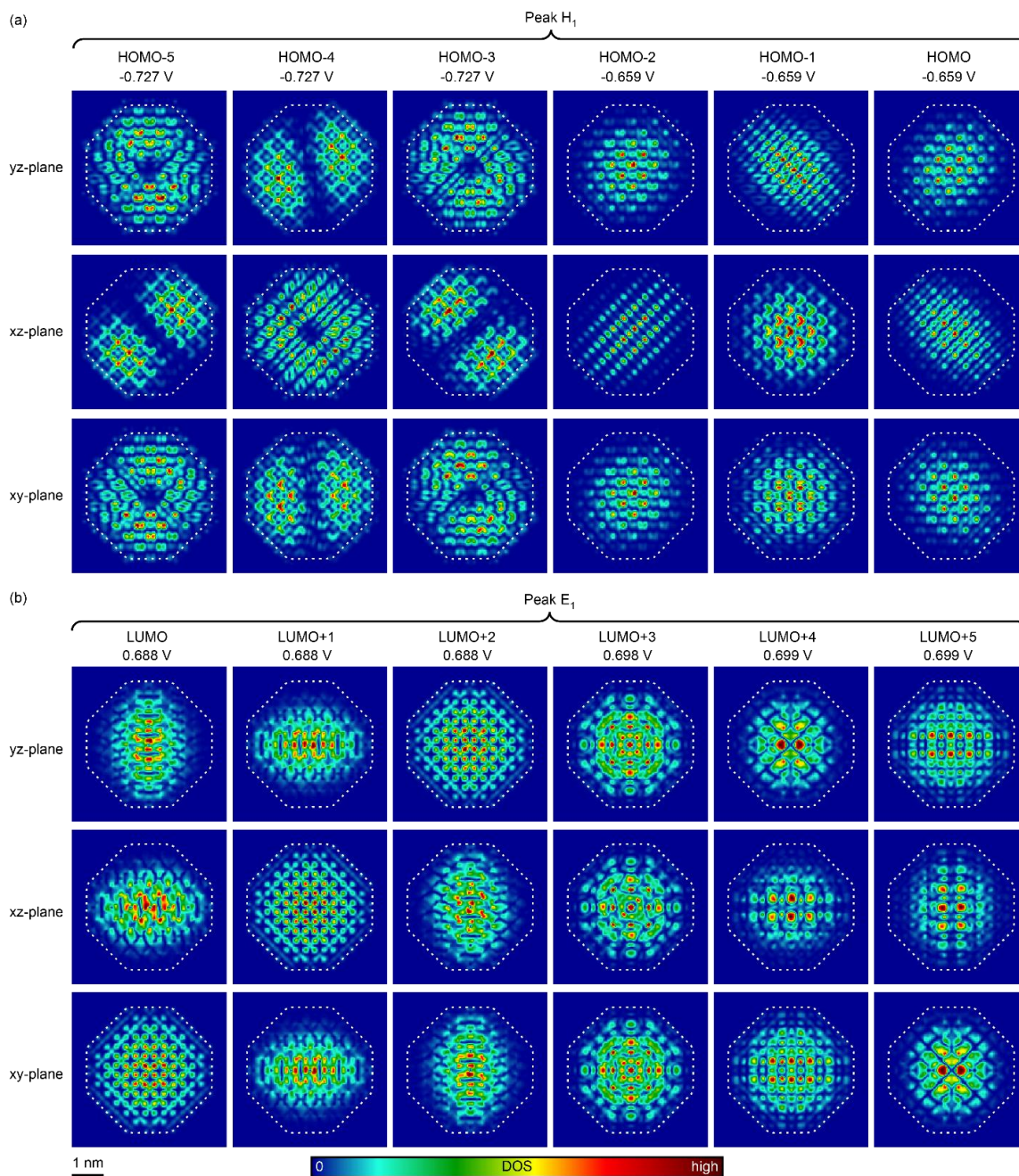
Figure A.5. Bulk cross-sections for individual orbitals of a model near-spherical (composition $H_{412}Si_{1087}$, diameter ~3.5 nm) SiNC without impurities. Section planes and view angles are the same as in Figure A.4. Each displayed DOS datapoint was averaged over a 3.6 Å-long segment orthogonal to, and bisected by the corresponding plane. (a) Highest occupied molecular orbitals (HOMO). (b) Lowest unoccupied molecular orbitals (LUMO).
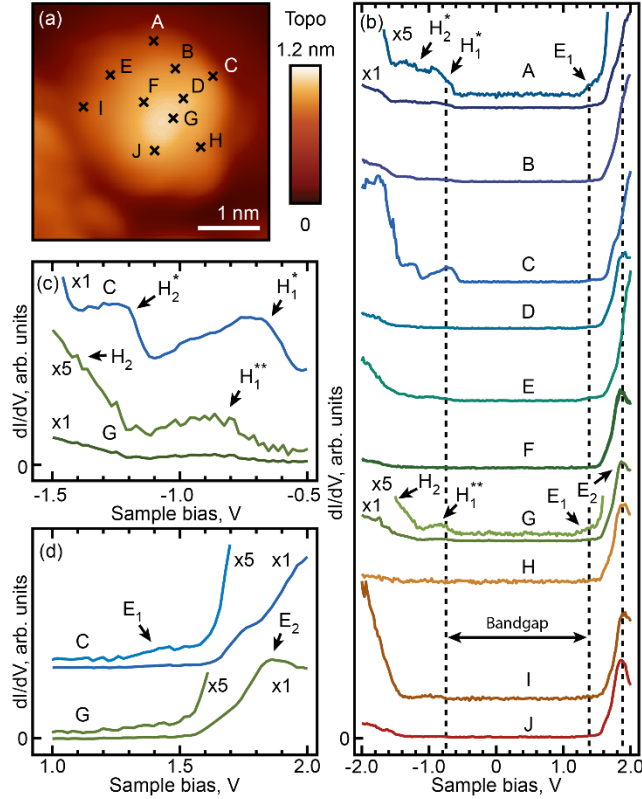
Figure A.6. STM/STS characterization of NC_2. (a) STM topography image of NC_2 [set point 2.2 V, 5.0 pA]. (b) DOS spectra [set point 2.0 V, 20 pA] measured at the locations A-I marked in (a). Spectra are offset for clarity. Prominent occupied and unoccupied states are marked with an 'H' and 'E' respectively. (c-d) Close-up of spectra from C, G and J locations.
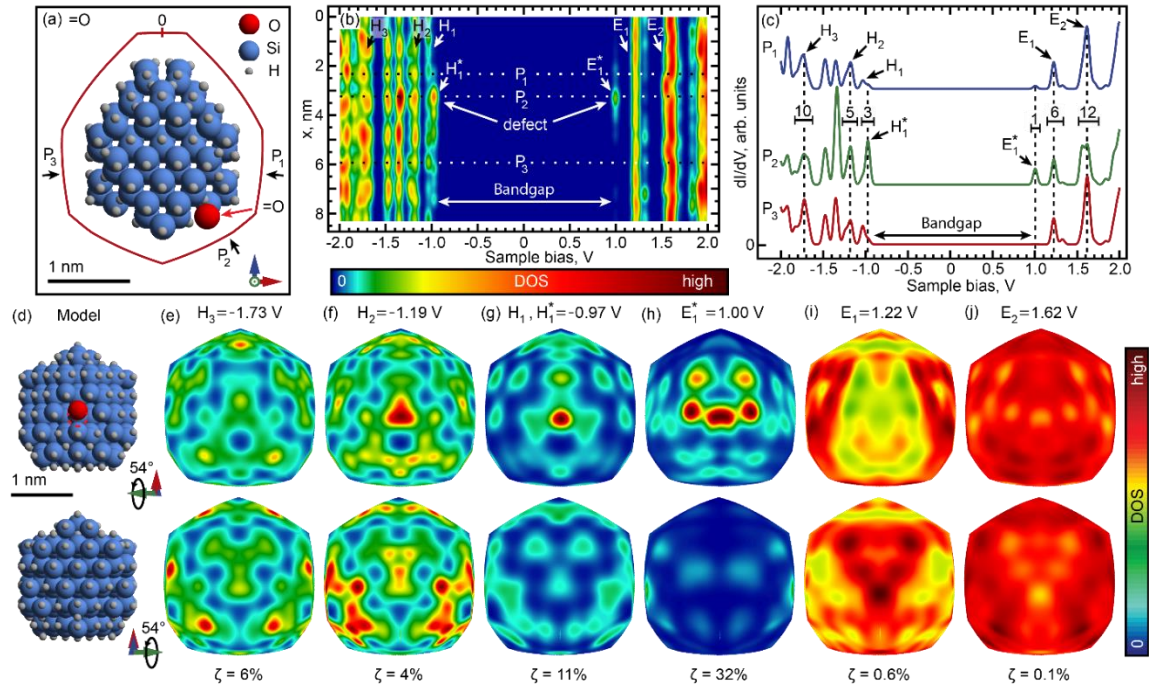
Figure A.7. Theoretical DOS for a model near-spherical (composition $H_{114}Si_{175}O$, diameter ~2 nm) SiNC with a Si=O impurity. Data arrangement and markings are the same as in Figure 2. In (c), P_2 corresponds to the defect location. Locations P_1 and P_3 correspond to locations P_2 and P_3 in Figures 4, S8 and S9. The top and bottom rows in (d-j) show opposite sides of the NC. To more closely reproduce experimental conditions, all spectra were normalized to give the same total current at 1.7 V.
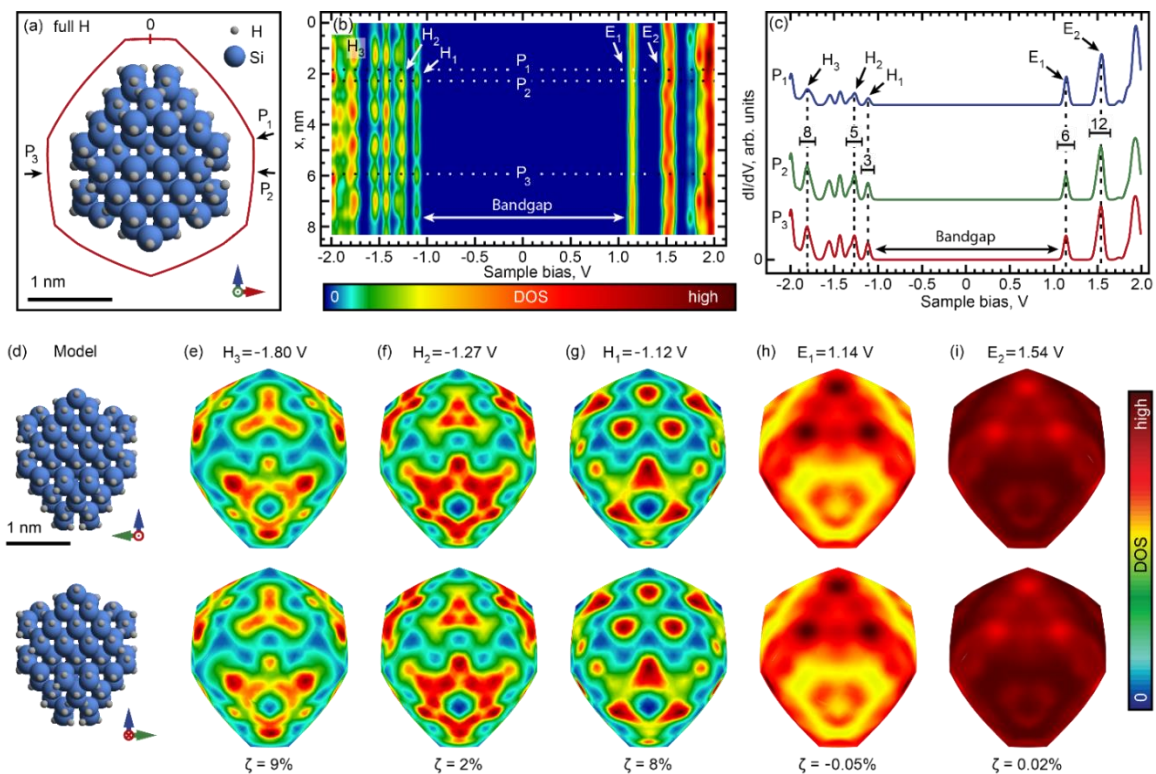
Figure A.8. Theoretical DOS for a model near-spherical (composition $H_{116}Si_{175}$, diameter ~2 nm) SiNC without impurities. Data arrangement and markings are the same as in Figure 2. In (c), locations P_1, P_2 and P_3 are the same as in Figures 4 and S9. The top and bottom rows in (d-i) show opposite sides of the NC. To more closely reproduce experimental conditions, all spectra were normalized to give the same total current at 1.7 V.
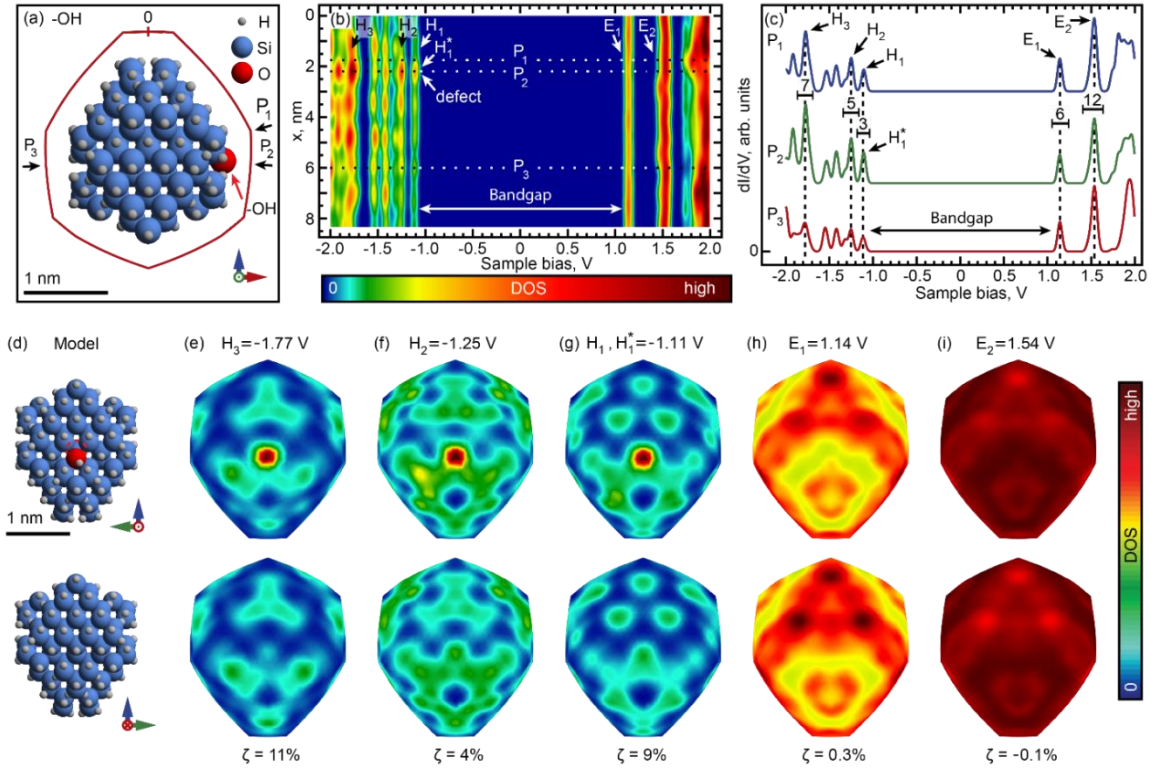
Figure A.9. Theoretical DOS for a model near-spherical (composition $H_{116}Si_{175}O$, diameter ~2 nm) SiNC with a Si–OH impurity. Data arrangement and markings are the same as in Figure 2. In (c), P_1 is the same location as in Figure 4. Location P_2 corresponds to the defect location. Location P_3 is positioned on the opposite side of NC with respect to P_2. The top and bottom rows in (d-i) show opposite sides of the NC. To more closely reproduce experimental conditions, all spectra were normalized to give the same total current at 1.7 V.
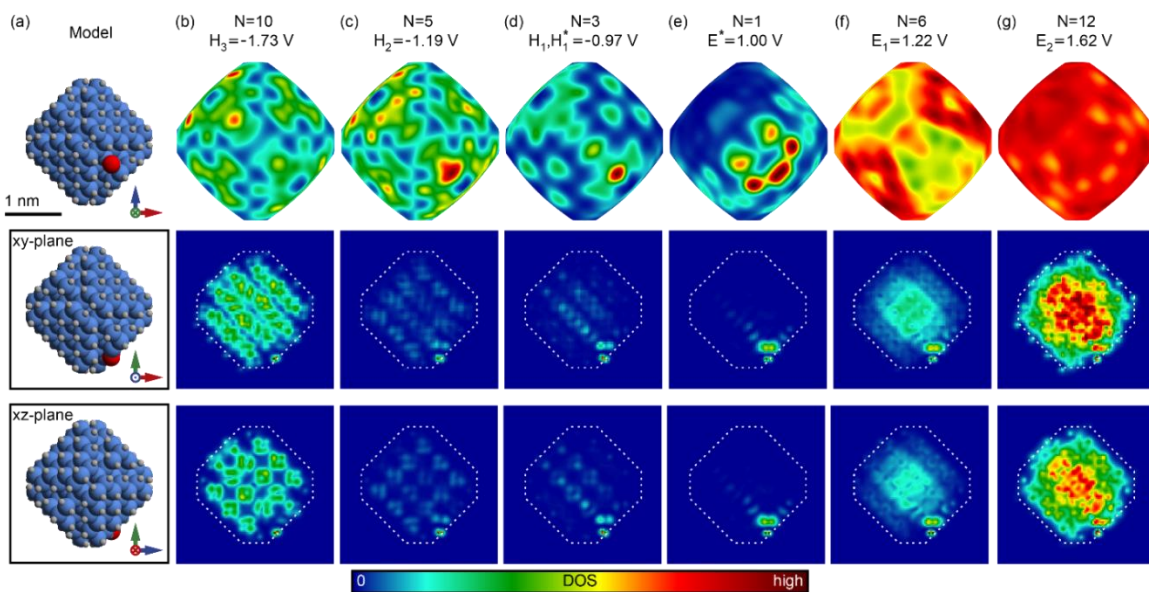
Figure A.10. Volume distribution of theoretical DOS for a model near-spherical (composition $H_{114}Si_{175}O$, diameter ~2 nm) SiNC with a Si=O impurity. (a) NC geometry. (b-g) DOS for the peaks from Figure A.7c. N is the number of individual states comprising the peak. First row represents the normalized DOS maps on the surface (identical to Figure A.7e-j). Second and third rows show bulk unnormalized DOS distributions across the main coordinate planes containing the oxygen atom. Each displayed DOS datapoint was averaged over a 3.6 Å-long segment orthogonal to, and bisected by the corresponding plane.
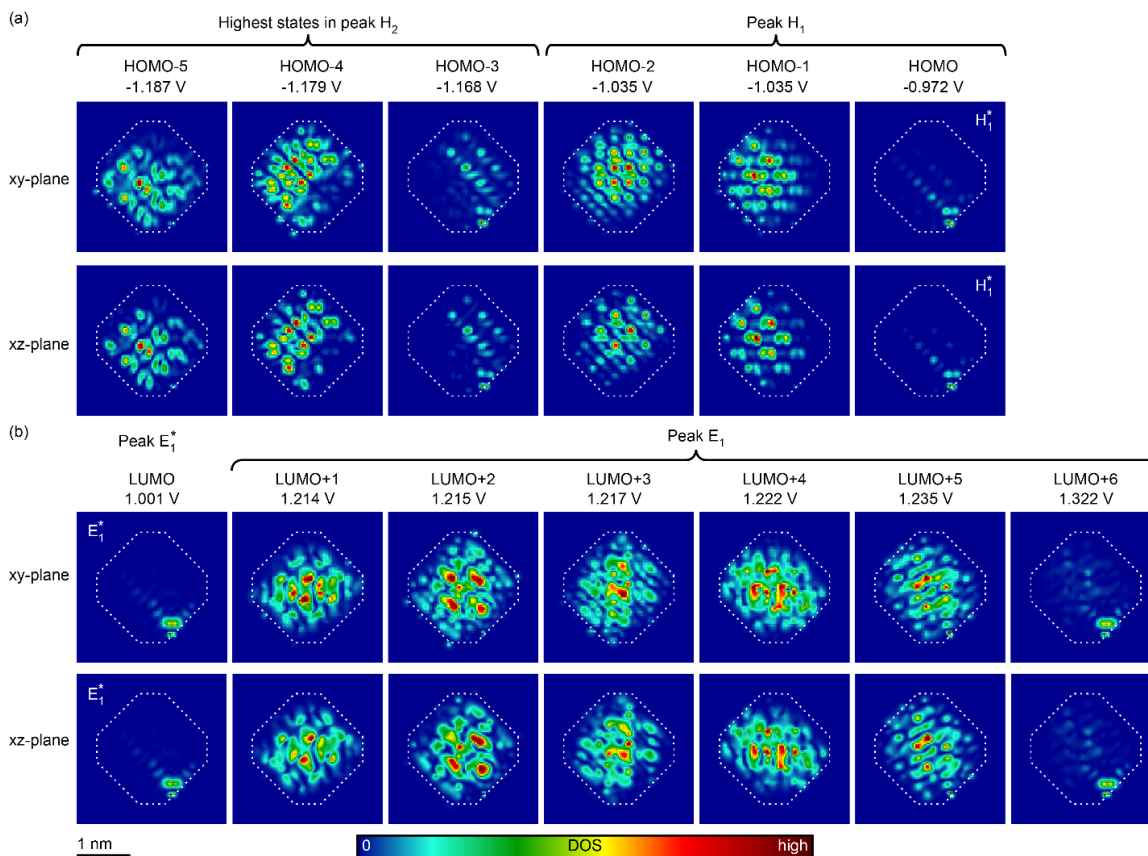
Figure A.11. Bulk cross-sections for individual orbitals of a model near-spherical (composition $H_{114}Si_{175}O$, diameter ~2 nm) SiNC with a Si=O impurity. Section planes and view angles are the same as in Figure A.10. Each displayed DOS datapoint was averaged over a 3.6 Å-long segment orthogonal to, and bisected by the corresponding plane. (a) Highest occupied molecular orbitals (HOMO). (b) Lowest unoccupied molecular orbitals (LUMO).
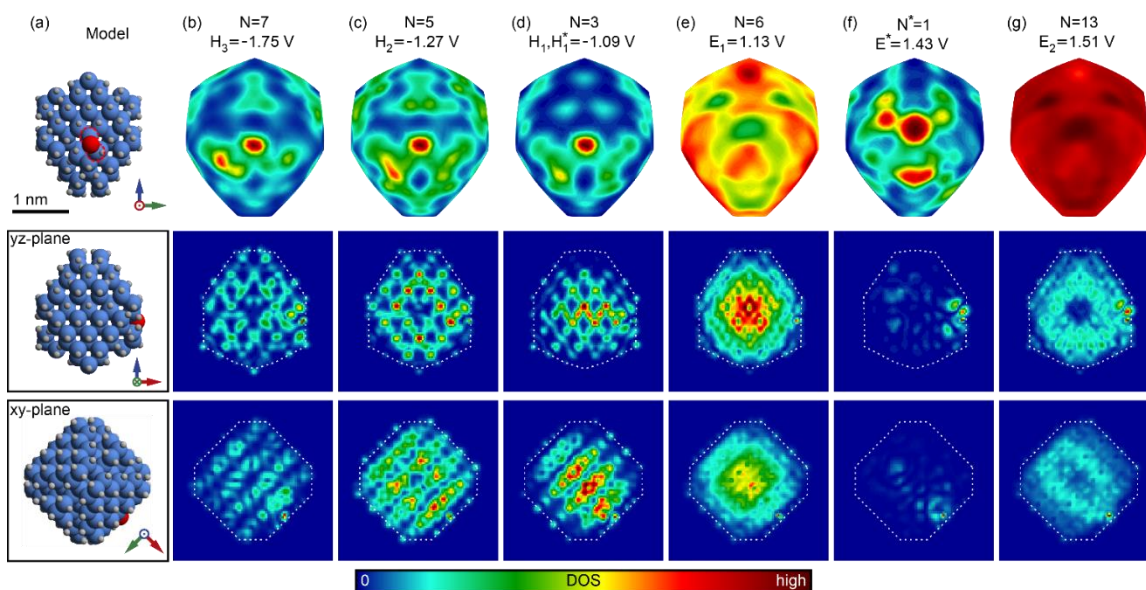
Figure A.12. Volume distribution of theoretical DOS for a model near-spherical (composition $H_{114}Si_{175}O$, diameter ~2 nm) SiNC with a Si−O−Si impurity. (a) NC geometry. (b-g) DOS for the peaks from Figure 4c. N is the number of individual states comprising the peak. First row represents the normalized DOS maps on the surface (identical to Figure 4e-j). Second and third rows show bulk unnormalized DOS distributions across the main coordinate planes containing the oxygen atom. Each displayed DOS datapoint was averaged over a 3.6 Å-long segment orthogonal to, and bisected by the corresponding plane.
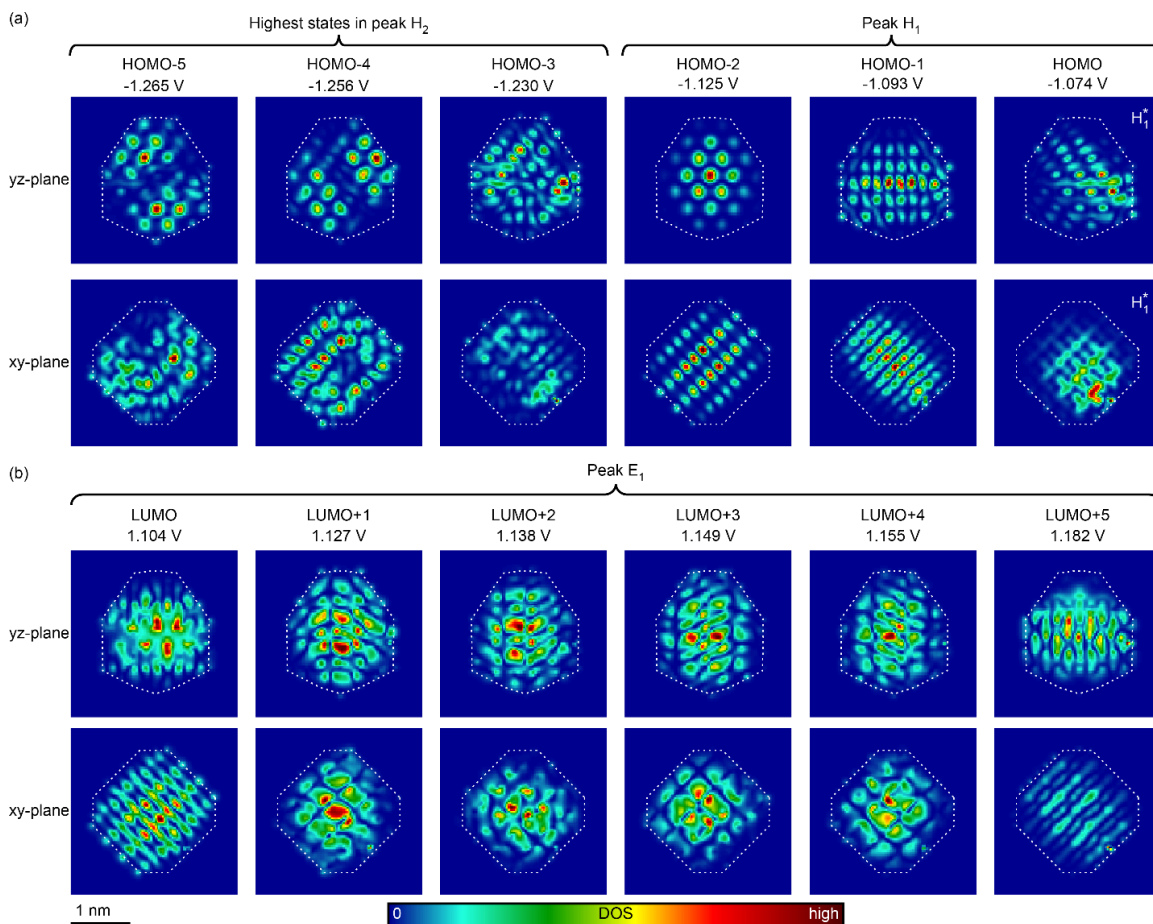
Figure A.13. Bulk cross-sections for individual orbitals of a model near-spherical (composition $H_{114}Si_{175}O$, diameter ~2 nm) SiNC with a Si−O−Si impurity. Section planes and view angles are the same as in Figure A.12. Each displayed DOS datapoint was averaged over a 3.6 Å-long segment orthogonal to, and bisected by the corresponding plane. (a) Highest occupied molecular orbitals (HOMO). (b) Lowest unoccupied molecular orbitals (LUMO).
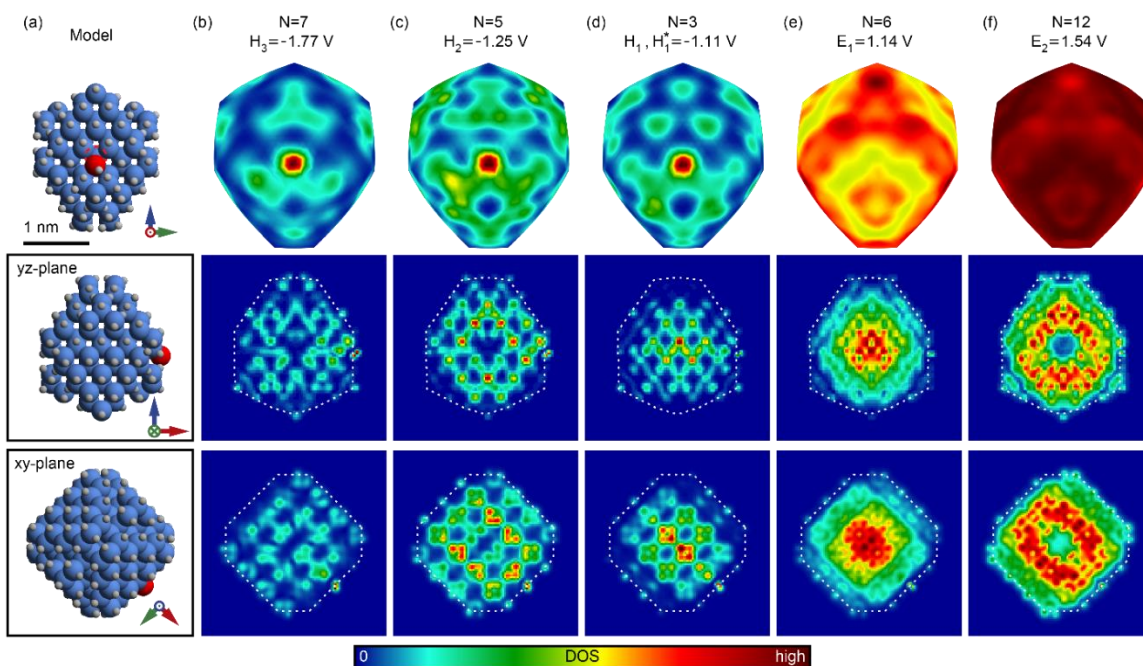
Figure A.14. Volume distribution of theoretical DOS for a model near-spherical (composition $H_{116}Si_{175}O$, diameter ~2 nm) SiNC with a Si−OH impurity. (a) NC geometry. (b-f) DOS for the peaks from Figure A.9c. N is the number of individual states comprising the peak. First row represents the normalized DOS maps on the surface (identical to Figure A.9e-i). Second and third rows show bulk unnormalized DOS distributions across the main coordinate planes containing the oxygen atom. Each displayed DOS datapoint was averaged over a 3.6 Å-long segment orthogonal to, and bisected by the corresponding plane.
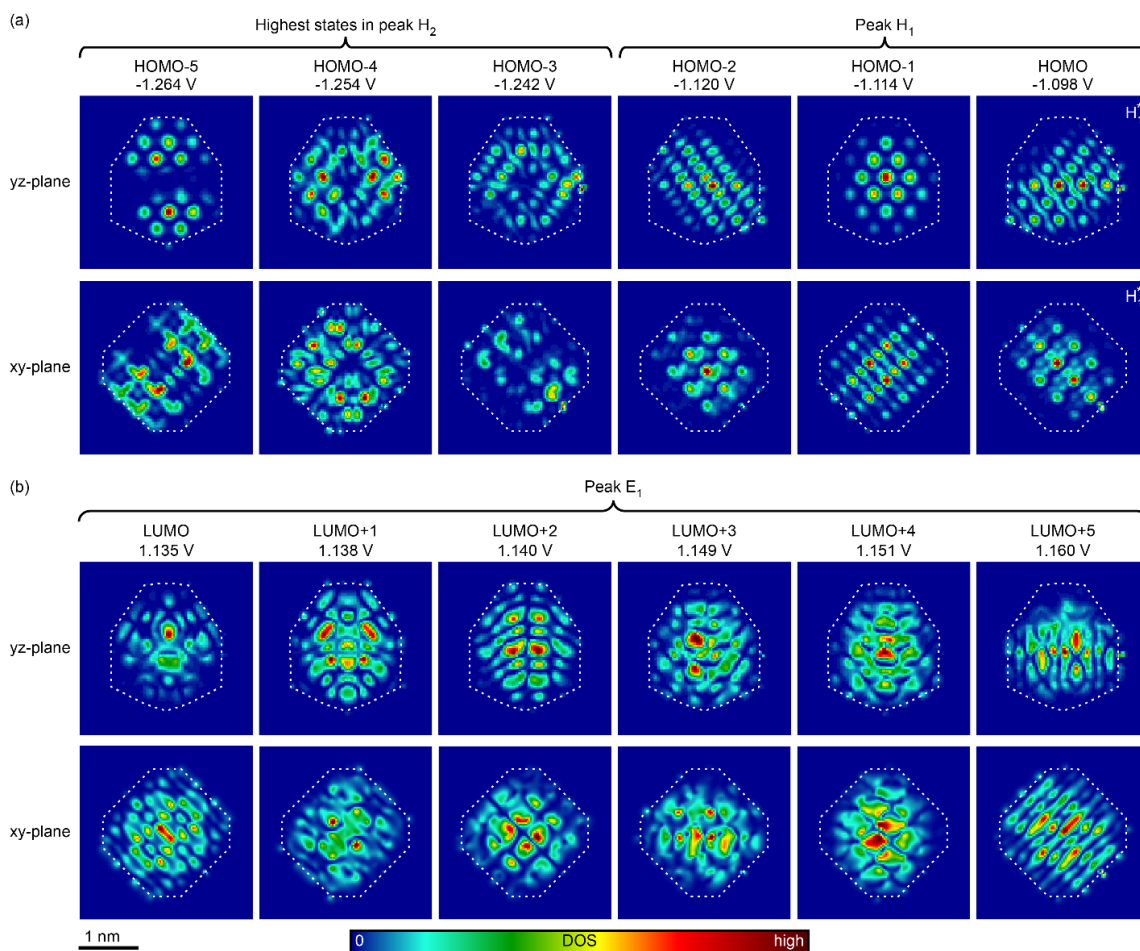
Figure A.15. Bulk cross-sections for individual orbitals of a model near-spherical (composition $H_{116}Si_{175}O$, diameter ~2 nm) SiNC with a Si−OH impurity. Section planes and view angles are the same as in Figure A.14. Each displayed DOS datapoint was averaged over a 3.6 Å-long segment orthogonal to, and bisected by the corresponding plane. (a) Highest occupied molecular orbitals (HOMO). (b) Lowest unoccupied molecular orbitals (LUMO).
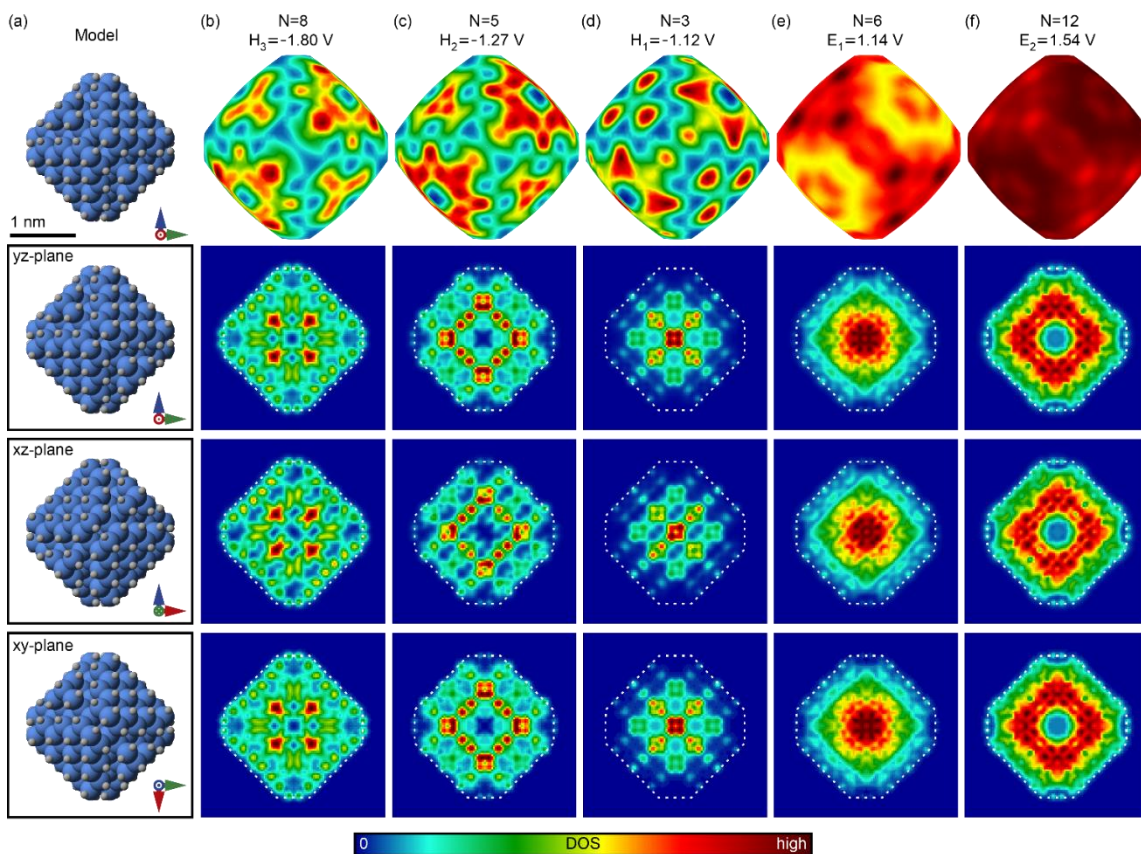
Figure A.16. Volume distribution of theoretical DOS for a model near-spherical (composition $H_{116}Si_{175}$, diameter ~2 nm) SiNC without impurities. (a) NC geometry. (b-f) DOS for the peaks from Figure A.8c. N is the number of individual states comprising the peak. First row represents the normalized DOS maps on the surface (identical to Figure A.8e-i). Second and third rows show bulk unnormalized DOS distributions across the main coordinate planes containing the oxygen atom. Each displayed DOS datapoint was averaged over a 3.6 Å-long segment orthogonal to, and bisected by the corresponding plane.

144
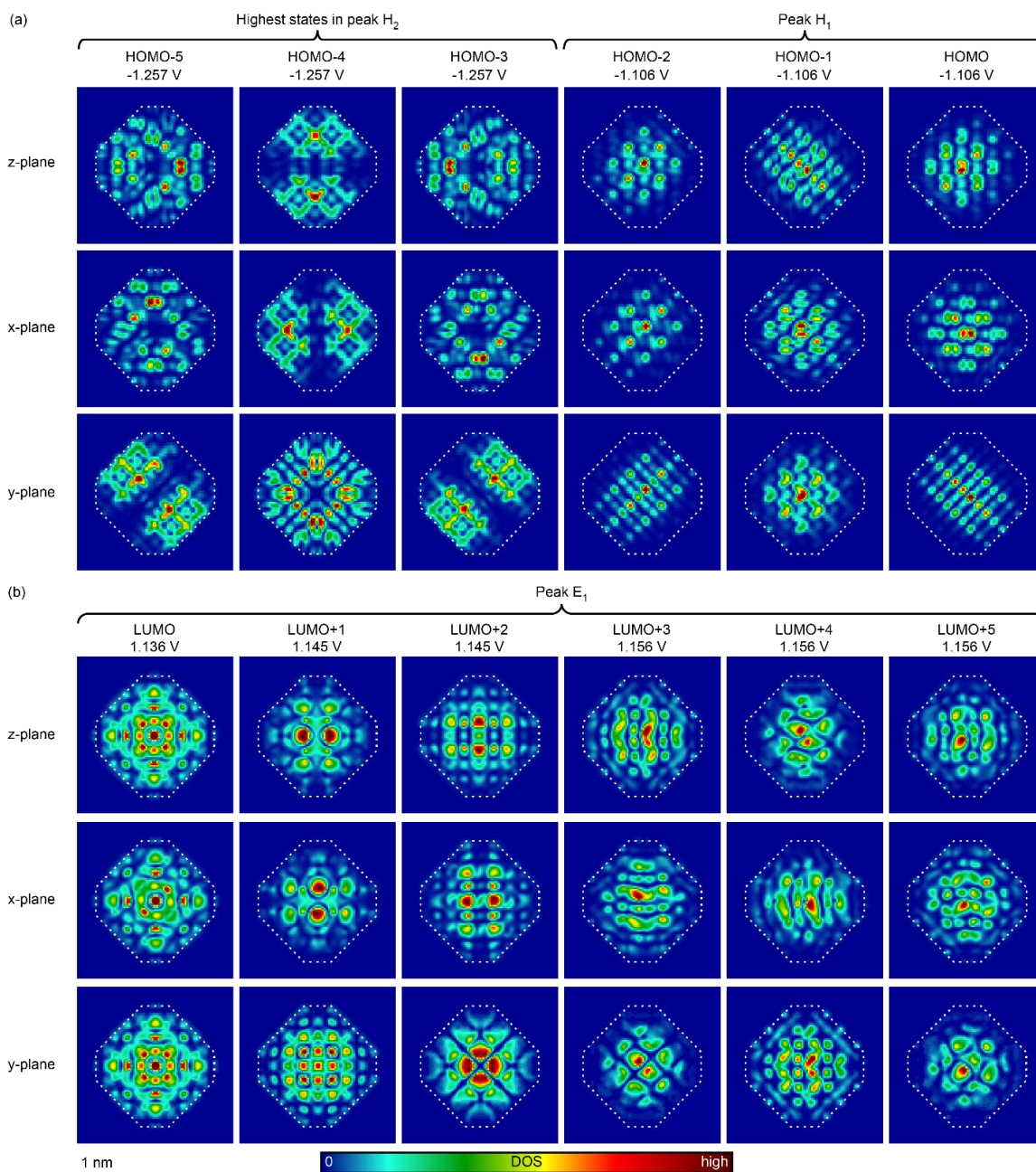
Figure A.17. Bulk cross-sections for individual orbitals of a model near-spherical (composition $H_{116}Si_{175}$, diameter ~2 nm) SiNC without impurities. Section planes and view angles are the same as in Figure A16. Each displayed DOS datapoint was averaged over a 3.6 Å-long segment orthogonal to, and bisected by the corresponding plane. (a) Highest occupied molecular orbitals (HOMO). (b) Lowest unoccupied molecular orbitals (LUMO).
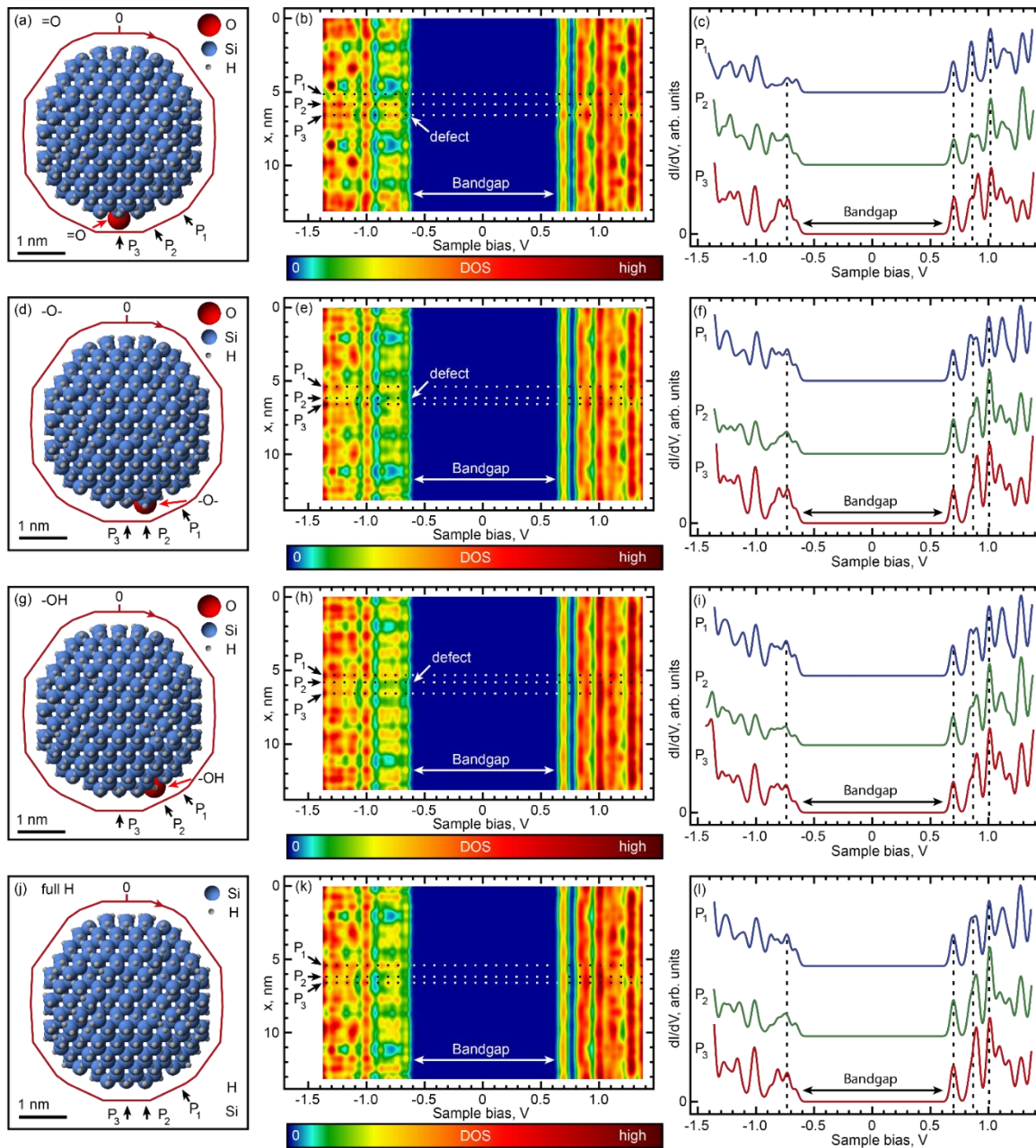
Figure A.18. Comparison of theoretical DOS for model near-spherical (diameter ~3.5 nm) SiNCs with and without impurities. (a) Geometry of a NC with a Si=O impurity and composition $H_{410}Si_{1087}O$. (b) Calculated 1D DOS map as a function of bias voltage and position x along the path shown in (a). (c) Individual DOS spectra from (b) measured at points P1 through P3. Spectra are offset for clarity. (d-f) Same as (a-c) for a NC with a Si−O−Si impurity and composition $H_{410}Si_{1087}O$. (g-i) Same as (a-c) for a NC with a Si−OH impurity and composition $H_{412}Si_{1087}O$. (j-l) Same as (a-c) for a NC without impurities, and composition $H_{412}Si_{1087}$. To more closely reproduce experimental conditions, all spectra were normalized to give the same total current at 1.35 V.

146

A.1 Free-standing H-SiNCs synthesis

Free-standing H-SiNCs were synthesized following a modified literature procedure[1]. Trichlorosilane (HSiCl$_3$, ≤ 98%; Alfa Aesar), pentane (anhydrous C$_5$H$_{12}$, Sigma-Aldrich), aqueous hydrofluoric acid (HF, 48.0–51.0%, Fisher Scientific), aqueous hydrochloric acid (HCl, 12N, Fisher Scientific), and ethanol (anhydrous EtOH, ACS grade, Pharmco-Aaper) were purchased for syntheses and used without further purification.

A Schlenk line was utilized to maintain an air-free environment during the sol-gel polycondensation with Ar flow as the inert gas. Other synthetic procedures, such as etching and solvent media switching, were done in air. For all aqueous solutions, electrophoretically pure water (nanopure water, 18 MΩ•cm resistivity) was used for aqueous mixtures preparation.

In a typical reaction, 4.5 mL of HSiCl$_3$ (45 mmol) was injected into a two-necked round-bottom flask, equipped with a small PTFE-coated magnetic stir bar. The flask with HSiCl$_{3(l)}$ was cooled in an ice bath for 10 minutes, then an aliquot (90 mmol) of nanopure water was quickly injected into the flask to accomplish hydrolysis and polycondensation of HSiCl$_3$. The mixture was cooled for another 3 minutes, then left under flowing Ar for 18h to purge HCl$_{(g)}$ byproduct. The resulting sol-gel hydrosilicate polymer was subsequently dried in *vacuo* for 18 hrs. This solid precursor was placed in an alumina boat, and was annealed at

147

1100 °C under flowing N_2 in a horizontal tube furnace (Lindberg Blue, Model TF55035A, Lindberg Scientific, Asheville, NC) for 10 hrs to produce nanocrystalline Si nanoparticles (NC Si NPs) embedded in SiO_x ($x \leq 2$) matrix (NC Si NPs/SiO_x). The annealed NC Si NPs/SiO_x powders (0.5 g) were ball-milled for 10 seconds in a tungsten carbide lined milling vial with two 1 cm tungsten carbide balls using a Spex 8000M mill mixer (SPEX SamplePrep, Metuchen, NJ). The milled NC Si NPs/SiO_x powder was subsequently etched in a chemical etching solution of 1:1:1 (by volume) ethanol/water/$HF_{(aq)}$ for 1 hr to liberate hydride-terminated Si NPs (SiNCs), which were then partitioned into pentane by biphasic extraction (10 × 5 mL of pentane extractions).

SUPPORTING MATERIAL FOR CHAPTER IV
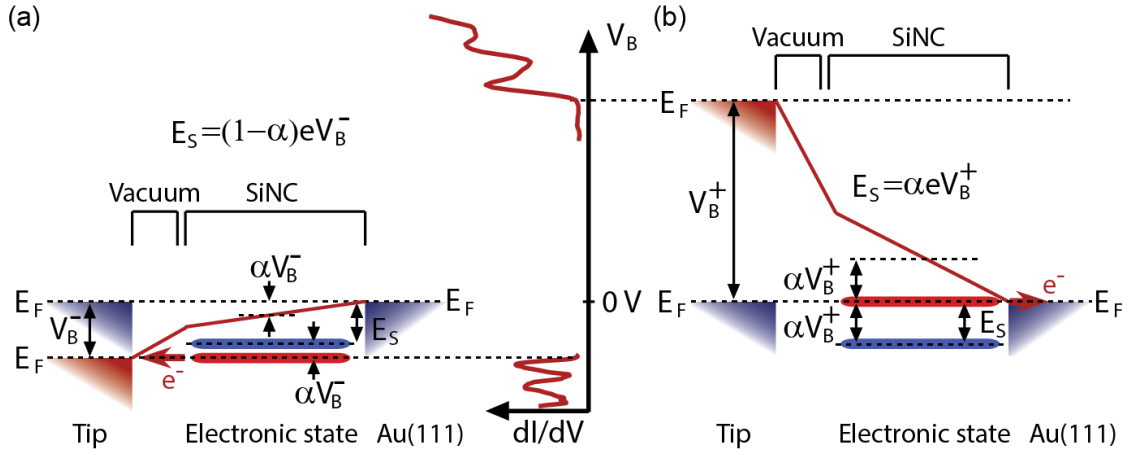
Figure B.1. Impact of the finite bias voltage drop inside a SiNC on the STS spectra. (a) "Direct" tunnelling through an occupied electronic state with energy E_S below the Fermi level (E_F) of the Au(111) substrate (corresponding states shown in blue). In a biased tunnel junction involving a SiNC (corresponding states shown in red), a finite voltage drop occurs across the SiNC volume changing the energy of all electronic states by $\alpha e V_B$, where V_B is the bias voltage, and $\alpha < 1$ is a function of the SiNC dimensions and dielectric susceptibility. Tunnelling into the state thus occurs when the Fermi level of the tip is aligned with the electronic state, which happens when $E_S = (1 - \alpha)e V_B$ (here, and everywhere in Figure B.1, we assume that all quantities are positive). The onset tunnelling voltage can thus be calculated as $E_S/(1 - \alpha)$.[2-3] (b) "Reverse" tunneling through an occupied state. In contrast to "direct" tunnelling, "reverse" tunneling is initiated when the Fermi level of the *Au(111) substrate* is aligned with the electronic state, which happens at opposite polarity to that of (a), when $E_S = \alpha e V_B$. This gives the onset tunnelling voltage of E_S/α.[2-3]
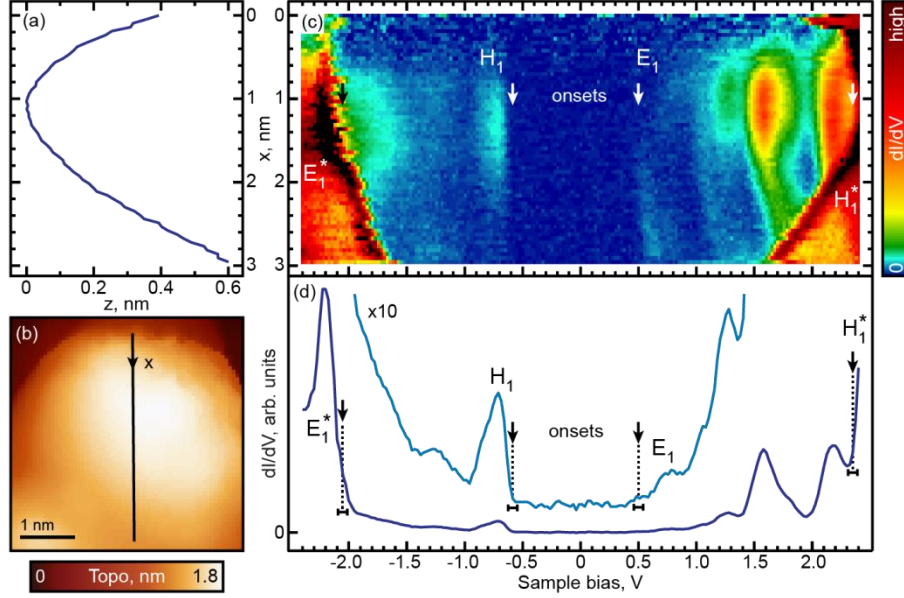
Figure B.2. Spatial mapping of LDOS for a representative SiNC showing spectral peaks corresponding to "direct" and "reverse" tunneling. (a) STM topographic profile [z height vs. x coordinate along the path shown in (b)]. (b) STM topographic image. Solid line is a trajectory for 1D STS mapping in (c). (c) dI/dV as a function of the bias voltage and position x along the path shown in (a). (d) Individual LDOS spectrum from (c) measured in the center of the path. Peaks originating from occupied (unoccupied) states produced by "direct" tunneling are marked 'H' ('E'), while peaks originating from "reverse" tunneling are marked 'H*' ('E*'). Horizontal error bars indicate the uncertainty in identification of the peak onsets. At the center of the SiNC, the ratio of the onsets for peaks E_1 and E_1^* gives $\alpha = 0.18 \pm 0.02$, and $\alpha = 0.20 \pm 0.02$ for peaks H_1 and H_1^*. (In the main text, we use $\alpha = 0.2$ as a representative value for SiNCs, to estimate the energy-voltage relationships for STS features corresponding to "direct" and "reverse" tunneling.) Voltage onsets for both "direct" and "reverse" tunnelling (at opposite bias polarities) vary with tip position on the NC surface. This is particularly noticeable for "reverse" tunneling peaks E_1^* and H_1^*, while the onsets of "direct" tunneling peaks E_1 and H_1 are relatively insensitive to the position along the SiNC. These onset variations are explained by the sensitivity of α to the geometry of the junction.[2] Indeed, both the tip position with respect to the SiNC, and the relative tip height z, which can both be expected to affect α, vary considerably across the scan range shown in the topography profiles (a) and (b). The larger sensitivity of peaks E_1^* and H_1^* to spatial location is explained by the fact that the onsets for these are inversely proportional to α (changes significantly), while the onsets for peaks E_1 and H_1 are inversely proportional to $1 - \alpha$ (changes relatively insignificantly due to the small value of α).
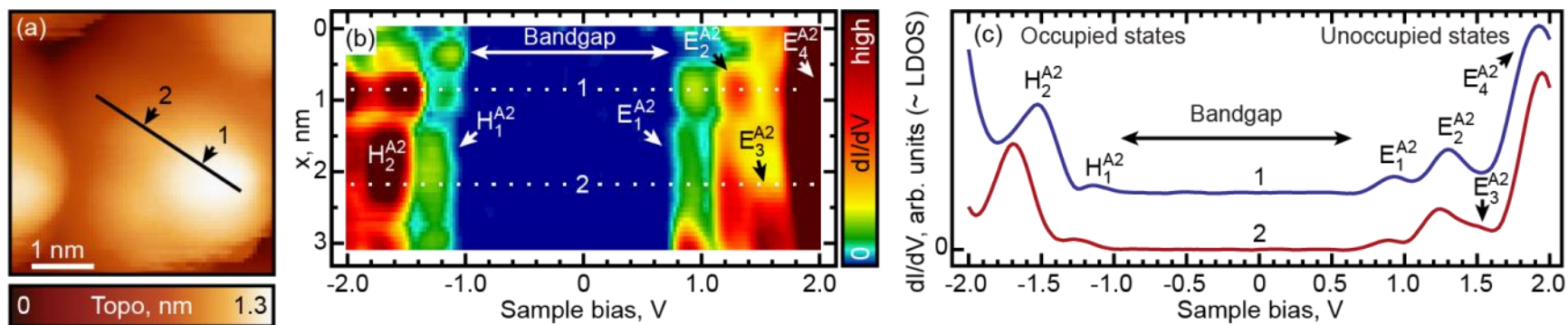
Figure B.3. Spatial mapping of LDOS for the SiNC from Figure 4.1(b) after partial dehydrogenation, but before DBs were generated. (a) Topography of the SiNC. (b) LDOS as a function of the bias voltage and position x along the path (solid line) shown in (a). (c) Individual LDOS spectra from (b) measured at points 1 and 2. Spectra are offset for clarity. Occupied and unoccupied states are marked 'H' and 'E' respectively.
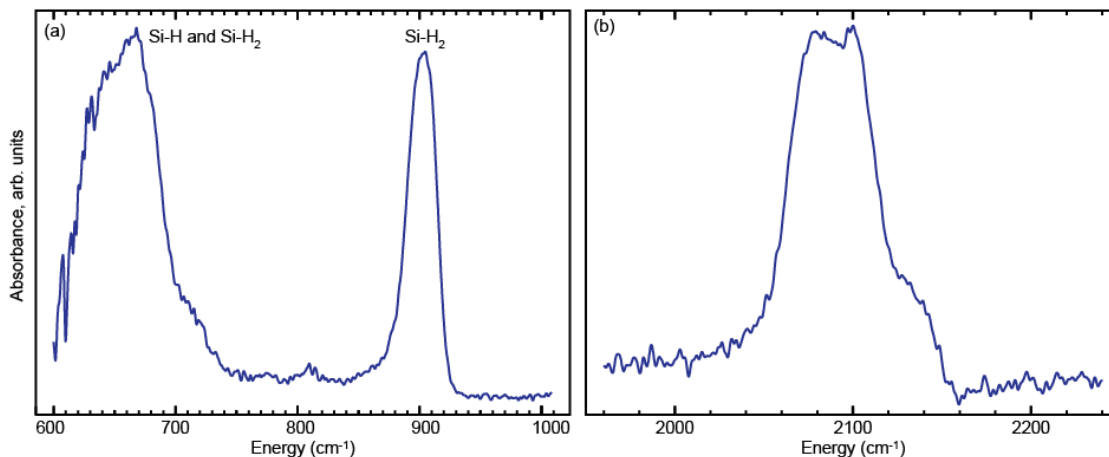
Figure B.4. FT-IR spectra of as-prepared hydrogen-terminated SiNCs dispersed in a hexane solution as described elsewhere.[4] (a) Low frequency region. Broad peak at 600-700 cm^{-1} includes: 1) the Si-H bending modes and Si-H$_2$ rocking mode of Si(100),[5] 2) the Si-H bending mode of Si(111)-(1×1),[6] and 3) the Si-H bending modes and Si-H$_2$ wagging mode originating from step-edges of vicinal H/Si(111) surfaces.[7] The peak at 904 cm^{-1}, on the other hand, has no contribution from Si-H: it contains the Si-H$_2$ scissoring bending mode,[5, 8] as well as the Si-H$_3$ degenerate deformation mode[9] (note that Si-H$_3$ population is expected to be significantly lower due to 2 times higher oxidation rate while exposed to the air during the measurement).[10] Intensity of both peaks are comparable, which suggests a significant presence of Si-H$_2$ on the {100}Times facets of measured SiNCs. For comparison, for the Si(100)-(3×1) surface, where ~1/3 of the surface Si atoms are terminated with dihydrides (and the rest are terminated with monohydrides), the relative intensity of the ~900 cm^{-1} region is an order of magnitude smaller than that of the ~600 cm^{-1}.[5] (b) High-frequency spectral region associated with silicon-hydride stretching modes. While the peak at 2100 cm^{-1} may be associated with both Si-H and Si-H$_2$, the shoulder observed at 2120-2140 cm^{-1} is indicative of Si-H$_2$.[5]
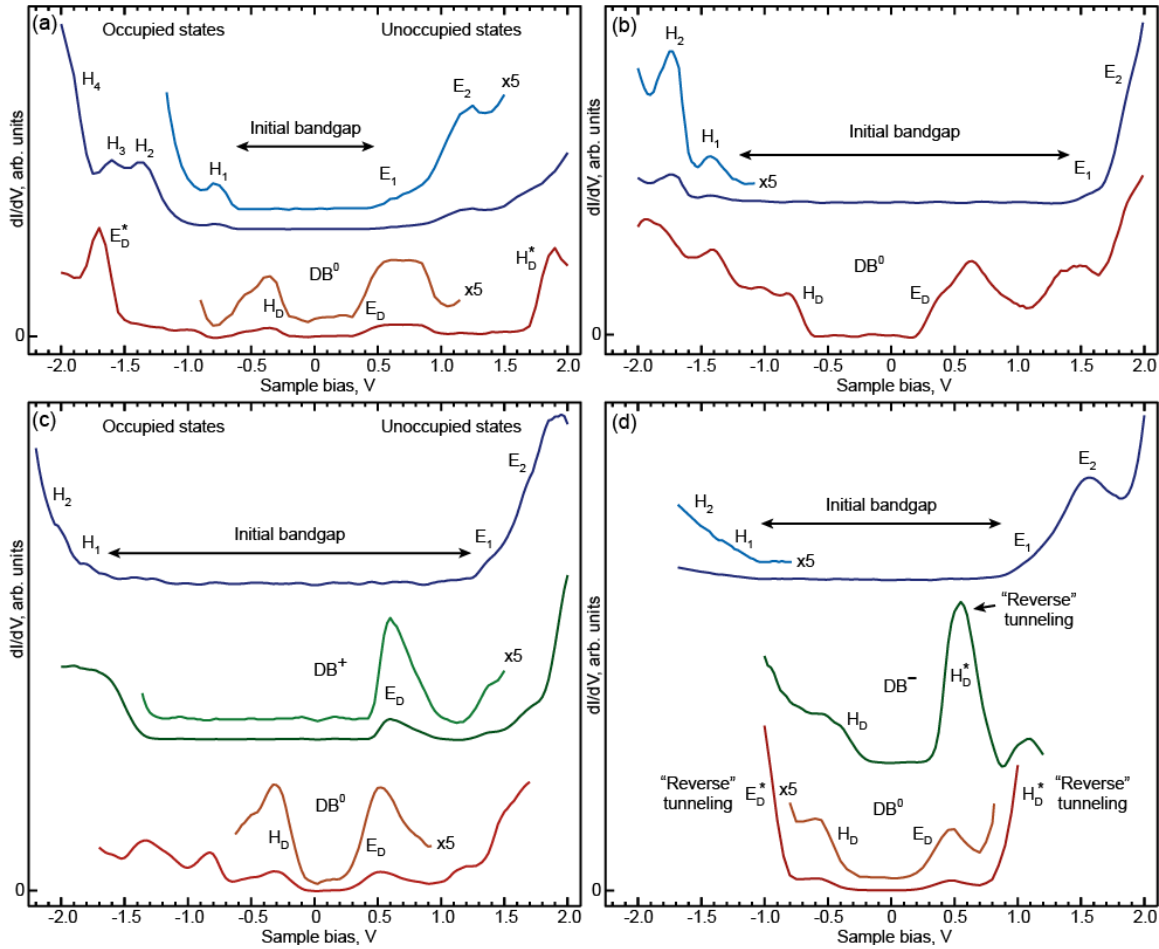
Figure B.5. STS characterization of additional SiNCs of different sizes. (a-d) STS spectra before ("pristine" state) and after application of ESD pulses causing reconstruction (narrowing of the bandgap) and the creation of localized DB states deep in the bandgap. The observed charge state of the DB is neutral (DB^0) in (a, b), switching from positive (DB^+) to neutral (DB^0) in (c), and switching from negative (DB^-) to neutral (DB^0) in (d). Note that "reverse" tunneling features (marked with "*") are observed in (a) and (d) with different values of α.

APPENDIX C

SUPPORTING MATERIAL FOR CHAPTER V

C.1. "Direct" and "reverse" tunneling in STS.

Figure 5.2c allows us to understand the nature of the observed peaks. Specifically, a salient feature of peak E_F^f in Figure 5.2c is the noticeable onset voltage variation along the scanned path, in contrast to peak H_F^f, which, despite being closely co-localized with peak E_F^f, does not show any distinguishable onset voltage variation. The observed differences in the spatial behavior of peaks E_F^f and H_F^f are indicative of "bipolar" tunneling, where individual states can contribute to tunneling current at either bias polarity, a consequence of existence of two tunneling barriers separating the state in question and tunneling contacts. "Bipolar" tunneling in STS measurements was previously demonstrated in experiments on molecular systems,[1-2] and, more recently, on SiNCs.[3] According to the "bipolar" tunneling model, the observed differences in the spatial behavior of peaks E_F^f and H_F^f can then be explained in the following fashion: For a state with energy E_S (measured with respect to the Fermi level of the sample), tunneling in double-barrier tunneling junction will occur at voltages $E_S/(1-\alpha)$ and $-E_S/\alpha$ [see Figure C.1 for a graphic illustration of these types of tunneling], where α<1 gives the fraction of the bias voltage dropped across the tunneling barrier existing between the state and the substrate.[1] Thus defined tunneling onsets $E_S/(1-\alpha)$ and $-E_S/\alpha$ correspond to the conventional (or "direct") type of tunneling, and "reverse" tunneling, respectively (Figure C.1). Because α depends on the overall geometry of the tunneling junction, both tunneling onsets are spatially-dependent. However, because α in the present situation is

small, the "direct" tunneling expression $E_S/(1-\alpha)$ changes significantly less than the "reverse" tunneling onset E_S/α. This identifies peaks E_F^f and H_F^f as those due to "direct" and "reverse" types of tunneling, respectively, with $\alpha \approx 0.06$ (here we assume that peaks E_F^f and H_F^f are produced by tunneling through the same state, which is supported by the fact that these peaks are co-localized).
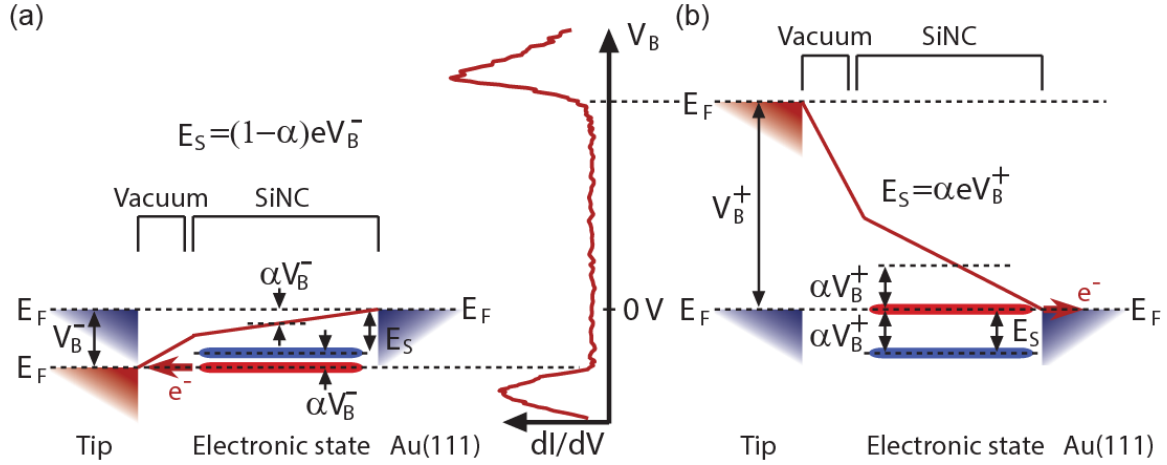
Figure C.1. Impact of the finite bias voltage drop inside a SiNC on the STS spectra. (a) "Direct" tunneling through an occupied electronic state with energy E_S below the Fermi level (E_F) of the Au(111) substrate (corresponding states shown in blue). In a biased tunnel junction involving a SiNC (corresponding states shown in red), a finite voltage drop occurs across the SiNC volume changing the energy of all electronic states by $\alpha e V_B$, where V_B is the bias voltage, and $\alpha < 1$ is a function of the SiNC dimensions and dielectric susceptibility. Tunneling into the state thus occurs when the Fermi level of the tip is aligned with the electronic state, which happens when $E_S = (1-\alpha)eV_B$ (here, and everywhere in Figure C.1, we assume that all quantities are positive). The onset tunneling voltage can thus be calculated as $E_S/(1-\alpha)$.[1-2] (b) "Reverse" tunneling through an occupied state. In contrast to "direct" tunneling, "reverse" tunneling is initiated when the Fermi level of the *Au(111) substrate* is aligned with the electronic state, which happens at opposite polarity to that of (a), when $E_S = \alpha e V_B$. This gives the onset tunneling voltage of E_S/α.[1-2]
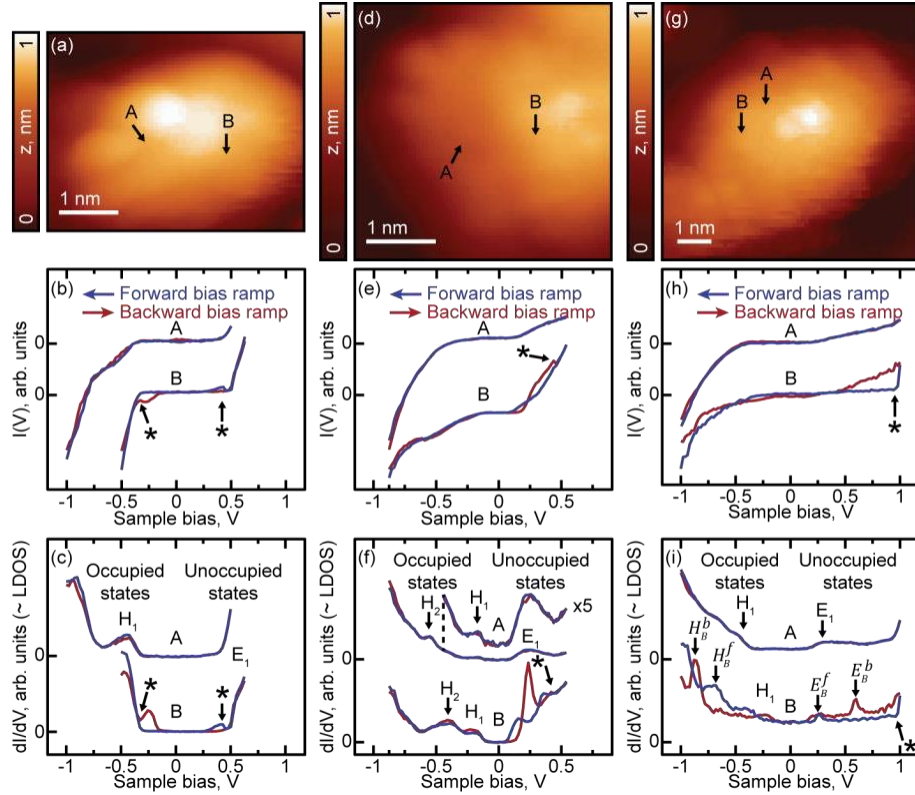
Figure C.2. STM/STS characterization of three additional SiNCs with bistable LDOS spectra. (a) Topographic image. (b,c) I(V) and dI/dV curves measured at the locations marked in (a). Each measurement is composed of a blue and red curve corresponding to the "forward" and "backward" bias ramps respectively. Switching events are seen as discontinuities in I(V) and dI/dV curves, and are each marked with an asterisk '*'. Each dI/dV curve serves as an estimate of the energy-dependent LDOS. H_1 and E_1 correspond to the band edge states, defined as states with LDOS delocalized over the entire SiNC surface. (d) Topographic image. (e,f) I(V) and dI/dV curves measured at the locations marked in (d). H_1 and E_1 correspond to the band edge states, and H_2 corresponds to next lowest occupied state. (g) Topographic image. (h,i) I(V) and dI/dV curves measured at the locations marked in (g). H_1 and E_1 correspond to the band edge states, while peak H_B^b (E_B^b) is caused by "reverse" tunneling through the same state as that of E_B^f (H_B^f). For all spectra, the current set-point was 10 pA.

156
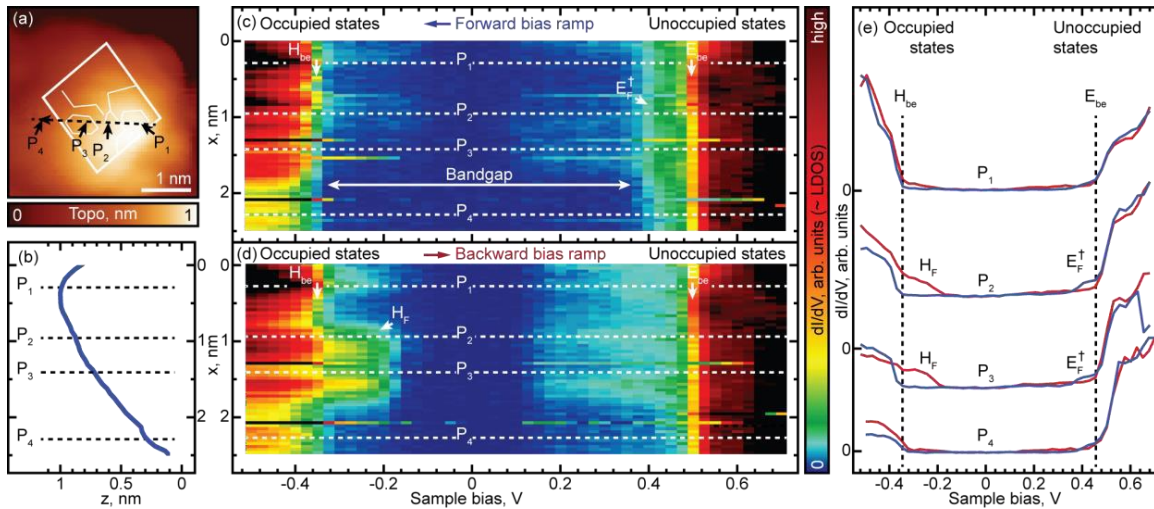
Figure C.3. Spatial cross-section of LDOS across a different SiNC than shown in Figure C.2 or the main text. (a) STM topographic image of the SiNC. (b) Topography profile along the path x shown in (a) with a dashed line. (c,d) "Forward" and "backward" bias ramp LDOS as a function of the bias voltage and position x along the path shown in (a). (e) Individual LDOS spectra from (c,d) measured at points P1 through P4. Spectra are offset for clarity. Horizontal lines of data that appear "discontinuous" in (c) are identical to those found in (d): the switch that typically occurs at negative voltages occurs at positive voltages for these lines. The spatial continuity of data assembled from different "forward" and "backward" LDOS spectra in (c) and (d) points to the extremely robust nature of the observed switching behavior.
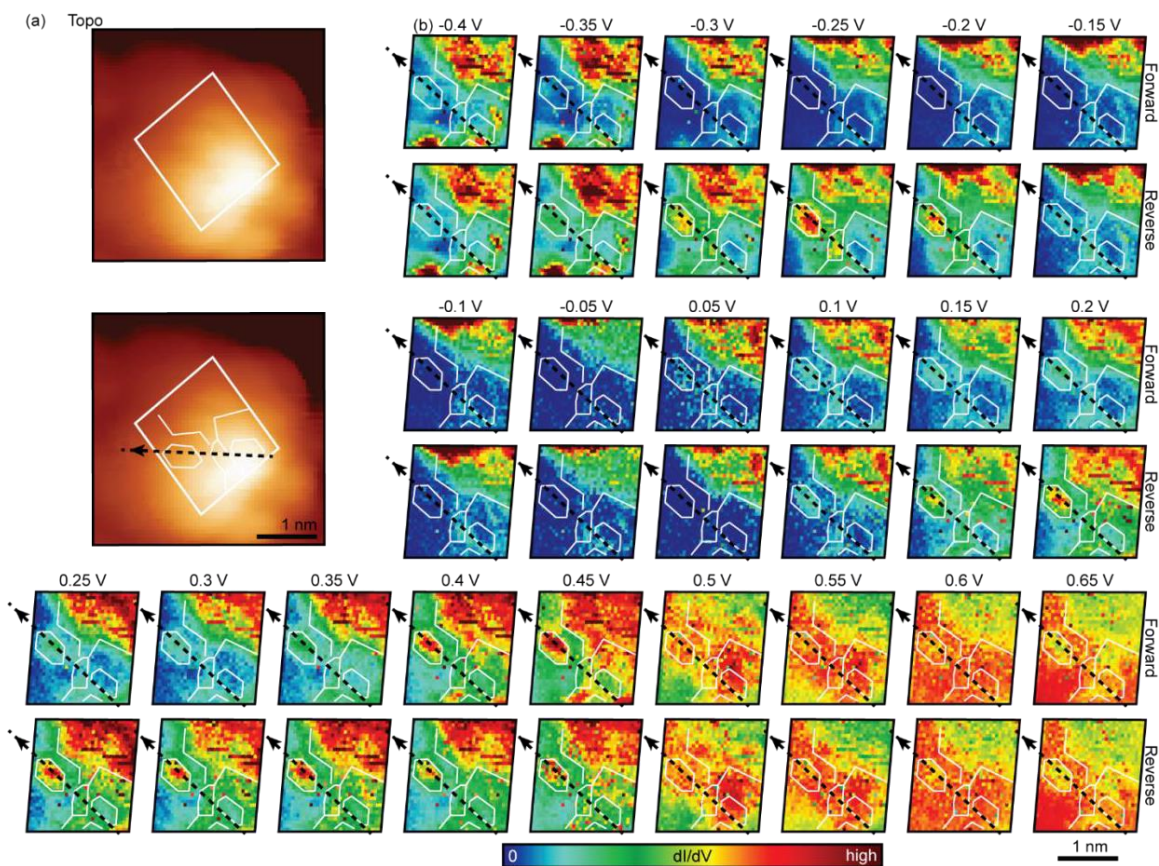
Figure C.4. Spatial mapping of LDOS across the SiNC from Figure C.2. (a) STM topographic image of the SiNC. (b) LDOS maps for selected bias voltage values (bandgap omitted). LDOS data was collected by recording the "forward" and "backward" pairs of spectra on a square grid of points across the SiNC surface. LDOS maps shown here are "cross-sections" of these "forward" and "backward" data sets corresponding to specific bias voltages. For each bias voltage value, the upper (lower) map corresponds to the "forward" ("backward") bias ramps. Individual pixels that appear to contain discontinuous data points correspond to points where conversion between "forward" and "backward" occurred at different voltages. Contour lines outline boundaries of distinctive features in LDOS maps (maps corresponding to 0.45 V, 0.25 V, and -0.25 V were used to define the boundaries).

C.2. Synthesis and Raman spectroscopy of SiNCs

The hydrogen-terminated silicon nanoparticles were synthesized as we have previously reported.[4] Briefly, silicon tetrachloride was hydrolyzed and polycondensed to produce a polymer with putative composition $(HSiO_{1.5})_n$, which was subsequently annealed at 1100°C under flowing N_2

to produce nanocrystalline Si particles embedded in an oxidized matrix. The nanocrystalline Si domains were liberated from the oxidized matrix using a wet chemical etch solution containing HF (49% aq.), ethanol, and water in a 1:1:1 ratio. At the completion of the 60 minute etch, the hydrogen-terminated silicon nanocrystals (H-Si NCs) were extracted into pentane for the STM/STS experiments. In a second experiment, the H-Si NCs were prepared identically, with the exception that they were extracted into hexane and used for Raman spectroscopy.

Directly after etching, the H-Si NCs in hexane were drop cast onto an aluminum foil substrate until a film of sufficient thickness developed. Raman spectra were then acquired using a Horiba HR800 UV Raman microscope system equipped with a 100 mW 532 nm diode-pumped solid-state laser. Spot measurements were taken at nine locations; the intensities of the nine spots were each normalized to the maximum intensity, and then averaged.

Using MagicPlot software (version 2.7.2), a linear baseline was first subtracted from the averaged data, which was then fit to three Gaussian peaks corresponding to the longitudinal optical (LO), amorphous phase transverse optical (TO_a), and nano-crystalline phase transverse optical (TO_{nc}) single phonons.[5] The LO peak was only used to improve the fit to the raw data and is not further discussed in this analysis. A summation of the fit results for the TO_a and TO_{nc} peaks is shown in Table C.1.

Calculated Curve	Center (cm^{-1})	Curve Area (arb. units)	% of each phase
TO_a	492.5	2.783	67.6
TO_{nc}	515.5	1.332	32.4

Table C.1. Peak position and area of the TO_a and TO_{nc} peaks shown in Figure 5.4. The percentage of each phase is also shown.

The Si-Si bonding for crystalline silicon is usually seen as a sharp peak at about 520 cm^{-1} and amorphous silicon shows a broad peak at around 480 cm^{-1}. A red shift of the crystalline peak is generally associated with lower dimensional crystalline structure *vs.* the bulk phase. The correlation length model presented by Richter, Wang, and Ley[6] relates the nano-crystalline domain size (D in nm) to the crystalline TO peak shift *vs.* the bulk crystalline peak at 520 cm^{-1}, as described in Equation 1 with parameters A = -52.3 cm^{-1}, γ = 1.586, and a = 0.543 nm (the Si lattice parameter). From this relationship, it follows that the average nanocrystalline domain is 2.55 nm in diameter.

$$\Delta\omega(D) = A\left(\frac{a}{D}\right)^{\gamma} \qquad (1)$$

From the integrated intensity of the fit TO$_{nc}$ and TO$_a$ curves, it was determined that the sample is on average 32.4% nanocrystalline Si (67.6% amorphous Si). The presence of both nanocrystalline and amorphous Si observed in the averaged Raman spectrum supports the interpretation of the STM/STS results, which noted differences in the contributions from these two phases as a function of the location of measurement.

REFERENCES CITED

REFERENCES CITED FOR CHAPTER I

(1)   Binnig, G.; Rohrer, H.; Gerber, C.; Weibel, E. Surface Studies by Scanning Tunneling Microscopy. *Phys. Rev. Lett.* **1982,** *49*, 57.

(2)   Binnig, G.; Rohrer, H.; Gerber, C.; Weibel, E. Tunneling through a controllable vacuum gap. *Appl. Phys. Lett.* **1982,** *40*, 178.

(3)   Binnig, G.; Garcia, N.; Rohrer, H.; Soler, J. M.; Flores, F. Electron-metal-surface interaction potential with vacuum tunneling: Observation of the image force. *Phys. Rev. B* **1984,** *30*, 4816.

(4)   Binnig, G.; Rohrer, H.; Gerber, C.; Weibel, E. 7 × 7 Reconstruction on Si(111) Resolved in Real Space. *Phys. Rev. Lett.* **1983,** *50*, 120.

(5)   Chadi, D. J.; Bauer, R. S.; Williams, R. H.; Hansson, G. V.; Bachrach, R. Z.; Mikkelsen, J. C.; Houzay, F.; Guichar, G. M.; Pinchaux, R.; Pétroff, Y. Atomic and electronic structure of the 7 × 7 reconstructed Si (111) surface. *Phys. Rev. Lett.* **1980,** *44*, 799.

(6)   Garcia, N. The surface profile of charge of Si(111)(7×7) obtained with He scattering. *Solid State Commun.* **1981,** *40*, 719.

(7)   Chadi, D. J. Atomic structure of Si(111) surfaces. *Surf. Sci.* **1980,** *99*, 1.

(8)   Hansson, G. V.; Bachrach, R. Z.; Bauer, R. S.; Chadi, D. J.; Göpel, W. Electronic structure of Si(111) surfaces. *Surf. Sci.* **1980,** *99*, 13.

(9)   Le Lay, G. New model for the reconstructed Si(111)7×7 and Si(111)√19×√19−R(±23°5) surfaces. *Surf. Sci. Lett* **1981,** *108*, L429.

(10)   Bennett, P. A.; Webb, M. W. The Si(111) 7 × 7 TO "1 × 1" transition. *Surf. Sci.* **1981,** *104*, 74.

(11)   Takayanagi, K.; Tanishiro, Y.; Takahashi, S.; Takahashi, M. Structure analysis of Si(111)-7 × 7 reconstructed surface by transmission electron diffraction. *Surf. Sci.* **1985,** *164*, 367.

(12)   Okumura, A.; Miyamura, K.; Gohshi, Y. The STM System Constructed for Analytical Application. *J. Microsc.* **1988,** *152*, 631.

(13)   Besocke, K. An easily operable scanning tunneling microscope. *Surf. Sci.* **1987,** *181*, 145.

(14)   Pan, S. H.; Hudson, E. W.; Davis, J. C. ^{3}He refrigerator based very low temperature scanning tunneling microscope. *Rev. Sci. Instrum.* **1999,** *70*, 1459.

(15)   Repp, J.; Meyer, G. Scanning Tunneling Spectroscopy of Molecules on Insulating Films. *CHIMIA* **2010,** *64*, 370.

(16)   Stipe, B. C.; Rezaei, M. A.; Ho, W. Single-molecule vibrational spectroscopy and microscopy. *Science* **1998,** *280*, 1732.

(17)   Ho, W. Single-molecule chemistry. *J. Chem. Phys.* **2002,** *117*, 11033.

(18)   Hoffman, J. E.; Hudson, E. W.; Lang, K. M.; Madhavan, V.; Eisaki, H.; Uchida, S.; Davis, J. C. A four unit cell periodic pattern of quasi-particle states surrounding vortex cores in $Bi_2Sr_2CaCu_2O_{8+\delta}$. *Science* **2002,** *295*, 466.

(19)   Heinrich, A. J.; Gupta, J. A.; Lutz, C. P.; Eigler, D. M. Single-atom spin-flip spectroscopy. *Science* **2004,** *306*, 466.

(20)   Coombs, J. H.; Gimzewski, J. K.; Reihl, B.; Sass, J. K.; Schlittler, R. R. Photon emission experiments with the scanning tunnelling microscope. *J. Microsc.* **1988,** *152*, 325.

(21)   Gimzewski, J. K.; Reihl, B.; Coombs, J. H.; Schlittler, R. R. Photon emission with the scanning tunneling microscope. *Z. Phys. B: Condens. Matter* **1988,** *72*, 497.

(22)   Moore, G. E. Cramming more components onto integrated circuits, Reprinted from Electronics, volume 38, number 8, April 19, 1965, pp.114 ff. *IEEE Solid-State Circuits Society Newsletter* **2006,** *11*, 33.

(23)   Pi, X. D.; Mangolini, L.; Campbell, S. A.; Kortshagen, U. Room-temperature atmospheric oxidation of Si nanocrystals after HF etching. *Phys. Rev. B* **2007,** *75*.

(24)   Kanemitsu, Y.; Okamoto, S.; Otobe, M.; Oda, S. Photoluminescence mechanism in surface-oxidized silicon nanocrystals. *Phys. Rev. B* **1997,** *55*, R7375.

(25)   Fernée, M. J.; Thomsen, E.; Jensen, P.; Rubinsztein-Dunlop, H. Highly efficient luminescence from a hybrid state found in strongly quantum confined PbS nanocrystals. *Nanotechnology* **2006,** *17*, 956.

(26)   Gao, J.; Johnson, J. C. Charge trapping in bright and dark states of coupled PbS quantum dot films. *ACS Nano* **2012,** *6*, 3292.

(27)   Tersoff, J. Low-frequency noise in nanoscale ballistic transistors. *Nano Lett.* **2007,** *7*, 194.

(28)   Wang, N. P.; Heinze, S.; Tersoff, J. Random-telegraph-signal noise and device variability in ballistic nanotube transistors. *Nano Lett.* **2007,** *7*, 910.

(29)   Swart, I.; Liljeroth, P.; Vanmaekelbergh, D. Scanning probe microscopy and spectroscopy of colloidal semiconductor nanocrystals and assembled structures. *Chem. Rev.* **2016,** *116*, 11181.

(30)   Bernard, R.; Comtet, G.; Dujardin, G.; Huc, V.; Mayne, A. J. Imaging and spectroscopy of individual CdSe nanocrystals on atomically resolved surfaces. *Appl. Phys. Lett.* **2005,** *87*, 053114.

REFERENCES CITED FOR CHAPTER II

(1)   Cohen-Tannoudji, C.; Laloë, F.; Diu, B. *Quantum mechanics*. Wiley: New York, 1977.

(2)   Chen, C. J. *Introduction to Scanning Tunneling Microscopy*. 2nd ed.; Oxford University Press: New York, 2008.

(3)   Shankar, R. *Principles of quantum mechanics*. 2nd ed.; Plenum Press: New York, 1994.

(4)   Chen, C. J. Theory of scanning tunneling spectroscopy. *J. Vac. Sci. Technol., A* **1988,** *6*, 319.

(5)   Bardeen, J. Tunnelling from a many-particle point of view. *Phys. Rev. Lett.* **1961,** *6*, 57.

(6)   Tersoff, J.; Hamann, D. R. Theory and application for the scanning tunneling microscope. *Phys. Rev. Lett.* **1983,** *50*, 1998.

(7)   Tersoff, J.; Hamann, D. R. Theory of the scanning tunneling microscope. *Phys. Rev. B* **1985,** *31*, 805.

(8)   Hamers, R. J.; Padowitz, D. F. Methods of tunneling spectroscopy with the STM. In *Scanning Probe Microscopy and Spectroscopy: Theory, Techniques, and Applications*, 2nd ed. ed.; Bonnell, D. Ed.; Wiley-WCH, Inc., 2000.

(9)   Hölzl, J.; Schulte, F. K. Work function of metals. In *Solid Surface Physics*, Hölzl, J.; Schulte, F. K.; Wagner, H. Eds.; Springer Tracts in Modern Physics, Springer Berlin Heidelberg, 1979; pp 1.

(10)   Garcia, N. Theory of Scanning Tunneling Microscopy and Spectroscopy: Resolution, Image and Field States, and Thin Oxide Layers. *IBM J. Res. Dev.* **1986,** *30*, 533.

(11)   Coombs, J. H.; Pethica, J. B. Properties of Vacuum Tunneling Currents: Anomalous Barrier Heights. *IBM J. Res. Dev.* **1986,** *30*, 455.

(12)   Pascual, J. I.; Corriol, C.; Ceballos, G.; Aldazabal, I.; Rust, H. P.; Horn, K.; Pitarke, J. M.; Echenique, P. M.; Arnau, A. Role of the electric field in surface electron dynamics above the vacuum level. *Phys. Rev. B* **2007,** *75*, 165326.

(13)   Hackley, J. D.; Kislitsyn, D. A.; Beaman, D. K.; Ulrich, S.; Nazin, G. V. High-stability cryogenic scanning tunneling microscope based on a closed-cycle cryostat. *Rev. Sci. Instrum.* **2014,** *85*, 103704.

(14)   Mastronardi, M. L.; Henderson, E. J.; Puzzo, D. P.; Ozin, G. A. Small silicon, big opportunities: the development and future of colloidally-stable monodisperse silicon nanocrystals. *Adv. Mater.* **2012,** *24*, 5890.

(15)   McVey, B. F.; Tilley, R. D. Solution synthesis, optical properties, and bioimaging applications of silicon nanocrystals. *Acc. Chem. Res.* **2014,** *47*, 3045.

(16)   Niesar, S.; Pereira, R. N.; Stegner, A. R.; Erhard, N.; Hoeb, M.; Baumer, A.; Wiggers, H.; Brandt, M. S.; Stutzmann, M. Low-Cost Post-Growth Treatments of Crystalline Silicon Nanoparticles Improving Surface and Electronic Properties. *Adv. Funct. Mater.* **2012,** *22*, 1190.

(17)   Dasog, M.; De los Reyes, G. B.; Titova, L. V.; Hegmann, F. A.; Veinot, J. G. Size vs surface: tuning the photoluminescence of freestanding silicon nanocrystals across the visible spectrum via surface groups. *ACS Nano* **2014,** *8*, 9636.

(18)   Dohnalová, K.; Gregorkiewicz, T.; Kůsová, K. Silicon quantum dots: surface matters. *J. Phys.: Condens. Matter* **2014,** *26,* 173201.

REFERENCES CITED FOR CHAPTER III

(1)   Xin, Y.; Nishio, K.; Saitow, K. I. White-blue electroluminescence from a Si quantum dot hybrid light-emitting diode. *Appl. Phys. Lett.* **2015,** *106,* 201102.

(2)   Hirschman, K. D.; Tsybeskov, L.; Duttagupta, S. P.; Fauchet, P. M. Silicon-based visible light-emitting devices integrated into microelectronic circuits. *Nature* **1996,** *384,* 338.

(3)   Govoni, M.; Marri, I.; Ossicini, S. Carrier multiplication between interacting nanocrystals for fostering silicon-based photovoltaics. *Nat. Photonics* **2012,** *6,* 672.

(4)   Cho, E. C.; Park, S.; Hao, X.; Song, D.; Conibeer, G.; Park, S. C.; Green, M. A. Silicon quantum dot/crystalline silicon solar cells. *Nanotechnology* **2008,** *19,* 245201.

(5)   Baxter, J. B.; Aydil, E. S. Nanowire-based dye-sensitized solar cells. *Appl. Phys. Lett.* **2005,** *86,* 1.

(6)   Plass, R.; Pelet, S.; Krueger, J.; Gratzel, M.; Bach, U. Quantum dot sensitization of organic-inorganic hybrid solar cells. *J. Phys. Chem. B* **2002,** *106,* 7578.

(7)   Gao, X. H.; Cui, Y. Y.; Levenson, R. M.; Chung, L. W. K.; Nie, S. M. In vivo cancer targeting and imaging with semiconductor quantum dots. *Nat. Biotechnol.* **2004,** *22,* 969.

(8)   Park, J.-H.; Gu, L.; von Maltzahn, G.; Ruoslahti, E.; Bhatia, S. N.; Sailor, M. J. Biodegradable luminescent porous silicon nanoparticles for in vivo applications. *Nat. Methods* **2009,** *8,* 331.

(9)   Buriak, J. M. Organometallic chemistry on silicon surfaces: formation of functional monolayers bound through Si-C bonds. *Chem. Commun.* **1999**, 1051.

(10)   Aldana, J.; Wang, Y. A.; Peng, X. G. Photochemical instability of CdSe nanocrystals coated by hydrophilic thiols. *J. Am. Chem. Soc.* **2001,** *123,* 8844.

(11)   Trani, F.; Cantele, G.; Ninno, D.; Iadonisi, G. Tight-binding calculation of the optical absorption cross section of spherical and ellipsoidal silicon nanocrystals. *Phys. Rev. B* **2005,** *72*, 075423.

(12)   Kocevski, V.; Eriksson, O.; Rusz, J. Transition between direct and indirect band gap in silicon nanocrystals. *Phys. Rev. B* **2013,** *87*, 245401.

(13)   Hapala, P.; Kusova, K.; Pelant, I.; Jelinek, P. Theoretical analysis of electronic band structure of 2- to 3-nm Si nanocrystals. *Phys. Rev. B* **2013,** *87*, 195420.

(14)   Wilson, W. L.; Szajowski, P. F.; Brus, L. E. Quantum confinement in size-selected, surface-oxidized silicon nanocrystals. *Science* **1993,** *262,* 1242.

(15)   Pavesi, L.; Dal Negro, L.; Mazzoleni, C.; Franzo, G.; Priolo, F. Optical gain in silicon nanocrystals. *Nature* **2000,** *408*, 440.

(16)   Anthony, R.; Kortshagen, U. Photoluminescence quantum yields of amorphous and crystalline silicon nanoparticles. *Phys. Rev. B* **2009,** *80*.

(17)   Timmerman, D.; Valenta, J.; Dohnalova, K.; de Boer, W. D. A. M.; Gregorkiewicz, T. Step-like enhancement of luminescence quantum yield of silicon nanocrystals. *Nat. Nanotechnol.* **2011,** *6*, 710.

(18)   Beard, M. C.; Knutsen, K. P.; Yu, P.; Luther, J. M.; Song, Q.; Metzger, W. K.; Ellingson, R. J.; Nozik, A. J. Multiple exciton generation in colloidal silicon nanocrystals. *Nano Lett.* **2007,** *7*, 2506.

(19)   Fischer, S. A.; Madrid, A. B.; Isborn, C. M.; Prezhdo, O. V. Multiple Exciton Generation in Small Si Clusters: A High-Level, Ab Initio Study. *J. Phys. Chem. Lett.* **2010,** *1*, 232.

(20)   Jaeger, H. M.; Hyeon-Deuk, K.; Prezhdo, O. V. Exciton Multiplication from First Principles. *Acc. Chem. Res.* **2013,** *46*, 1280.

(21)   Pi, X. D.; Mangolini, L.; Campbell, S. A.; Kortshagen, U. Room-temperature atmospheric oxidation of Si nanocrystals after HF etching. *Phys. Rev. B* **2007,** *75*.

(22)   Kanemitsu, Y.; Okamoto, S.; Otobe, M.; Oda, S. Photoluminescence mechanism in surface-oxidized silicon nanocrystals. *Phys. Rev. B* **1997,** *55*, R7375.

(23)   Wolkin, M. V.; Jorne, J.; Fauchet, P. M.; Allan, G.; Delerue, C. Electronic states and luminescence in porous silicon quantum dots: The role of oxygen. *Phys. Rev. Lett.* **1999,** *82*, 197.

(24)   van Buuren, T.; Dinh, L. N.; Chase, L. L.; Siekhaus, W. J.; Terminello, L. J. Changes in the Electronic Properties of Si Nanocrystals as a Function of Particle Size. *Phys. Rev. Lett.* **1998,** *80*, 3803.

(25)   Hessel, C. M.; Henderson, E. J.; Kelly, J. A.; Cavell, R. G.; Sham, T.-K.; Veinot, J. G. C. Origin of luminescence from silicon nanocrystals: a near edge X-ray absorption fine structure (NEXAFS) and X-ray excited optical luminescence (XEOL) study of oxide-embedded and free-standing systems. *J. Phys. Chem. C* **2008,** *112*, 14247.

(26)   Godefroo, S.; Hayne, M.; Jivanescu, M.; Stesmans, A.; Zacharias, M.; Lebedev, O. I.; Van Tendeloo, G.; Moshchalkov, V. V. Classification and control of the origin of photoluminescence from Si nanocrystals. *Nat. Nanotechnol.* **2008,** *3*, 174.

(27)   de Boer, W. D. A. M.; Timmerman, D.; Dohnalova, K.; Yassievich, I. N.; Zhang, H.; Buma, W. J.; Gregorkiewicz, T. Red spectral shift and enhanced quantum efficiency in phonon-free photoluminescence from silicon nanocrystals. *Nat. Nanotechnol.* **2010,** *5*, 878.

(28)   Liu, S. M. Luminescent silicon nanoparticles formed in solution. *J Nanosci Nanotechnol* **2008,** *8*, 1110.

(29)   Dasog, M.; Yang, Z.; Regli, S.; Atkins, T. M.; Faramus, A.; Singh, M. P.; Muthuswamy, E.; Kauzlarich, S. M.; Tilley, R. D.; Veinot, J. G. C. Chemical Insight into the Origin of Red and Blue Photoluminescence Arising from Freestanding Silicon Nanocrystals. *ACS Nano* **2013,** *7*, 2676.

(30)   Puzder, A.; Williamson, A. J.; Grossman, J. C.; Galli, G. Surface control of optical properties in silicon nanoclusters. *J. Chem. Phys.* **2002,** *117*, 6721.

(31)   Luppi, M.; Ossicini, S. Ab initio study on oxidized silicon clusters and silicon nanocrystals embedded in SiO2: Beyond the quantum confinement effect. *Phys. Rev. B* **2005,** *71*, 1.

(32)   Kocevski, V.; Eriksson, O.; Rusz, J. Size dependence of the stability, electronic structure, and optical properties of silicon nanocrystals with various surface impurities. *Phys. Rev. B* **2015,** *91*, 1.

(33)   Ramos, L. E.; Furthmuller, J.; Bechstedt, F. Effect of backbond oxidation on silicon nanocrystallites. *Phys. Rev. B* **2004,** *70.*

(34)   Vasiliev, I.; Chelikowsky, J. R.; Martin, R. M. Surface oxidation effects on the optical properties of silicon nanocrystals. *Phys. Rev. B* **2002,** *65,* 121302.

(35)   Puzder, A.; Williamson, A. J.; Grossman, J. C.; Galli, G. Computational studies of the optical emission of silicon nanocrystals. *J. Am. Chem. Soc.* **2003,** *125,* 2786.

(36)   Pennycook, T. J.; Hadjisavvas, G.; Idrobo, J. C.; Kelires, P. C.; Pantelides, S. T. Optical gaps of free and embedded Si nanoclusters: Density functional theory calculations. *Phys. Rev. B* **2010,** *82.*

(37)   Zhou, Z. Y.; Brus, L.; Friesner, R. Electronic structure and luminescence of 1.1-and 1.4-nm silicon nanocrystals: Oxide shell versus hydrogen passivation. *Nano Lett.* **2003,** *3,* 163.

(38)   Chen, C. J. *Introduction to Scanning Tunneling Microscopy.* 2nd ed.; Oxford University Press: New York, 2008.

(39)   Wolf, O.; Dasog, M.; Yang, Z.; Balberg, I.; Veinot, J. G. C.; Millo, O. Doping and quantum confinement effects in single Si nanocrystals observed by scanning tunneling spectroscopy. *Nano Lett.* **2013,** *13,* 2516.

(40)   Kislitsyn, D. A.; Gervasi, C. F.; Allen, T.; Palomaki, P. K. B.; Hackley, J. D.; Maruyama, R.; Nazin, G. V. Spatial Mapping of Sub-Bandgap States Induced by Local Nonstoichiometry in Individual Lead Sulfide Nanocrystals. *J Phys Chem Lett* **2014,** *5,* 3701.

(41)   Gervasi, C. F.; Kislitsyn, D. A.; Allen, T. L.; Hackley, J. D.; Maruyama, R.; Nazin, G. V. Diversity of sub-bandgap states in lead-sulfide nanocrystals: real-space spectroscopy and mapping at the atomic-scale. *Nanoscale* **2015,** *7,* 19732.

(42)   Hackley, J. D.; Kislitsyn, D. A.; Beaman, D. K.; Ulrich, S.; Nazin, G. V. High-stability cryogenic scanning tunneling microscope based on a closed-cycle cryostat. *Rev. Sci. Instrum.* **2014,** *85,* 103704.

(43)   Chiu, S.-K.; Manhat, B. A.; DeBenedetti, W. J. I.; Brown, A. L.; Fichter, K.; Vu, T.; Eastman, M.; Jiao, J.; Goforth, A. M. Aqueous red-emitting silicon nanoparticles for cellular imaging: Consequences of protecting against surface passivation by hydroxide and water for stable red emission. *J. Mater. Res.* **2013,** *28*, 216.

(44)   Ordejon, P.; Artacho, E.; Soler, J. M. Self-consistent order-N density-functional calculations for very large systems. *Phys. Rev. B* **1996,** *53*, 10441.

(45)   Soler, J. M.; Artacho, E.; Gale, J. D.; Garcia, A.; Junquera, J.; Ordejon, P.; Sanchez-Portal, D. The SIESTA method for ab initio order-N materials simulation. *J. Phys.: Condens. Matter* **2002,** *14*, 2745.

(46)   Hadjisavvas, G.; Remediakis, I. N.; Kelires, P. C. Shape and faceting of Si nanocrystals embedded in a−SiO$_2$: A Monte Carlo study. *Phys. Rev. B* **2006,** *74*, 165419.

(47)   Wang, Y. Q.; Smirani, R.; Ross, G. G. Nanotwinning in silicon nanocrystals produced by ion implantation. *Nano Lett.* **2004,** *4*, 2041.

(48)   Sun, Z.; Swart, I.; Delerue, C.; Vanmaekelbergh, D.; Liljeroth, P. Orbital and charge-resolved polaron states in CdSe dots and rods probed by scanning tunneling spectroscopy. *Phys. Rev. Lett.* **2009,** *102*, 196401.

(49)   Hessel, C. M.; Henderson, E. J.; Veinot, J. G. C. Hydrogen silsesquioxane: A molecular precursor for nanocrystalline Si-SiO$_2$ composites and freestanding hydride-surface-terminated silicon nanoparticles. *Chem. Mater.* **2006,** *18*, 6139.

(50)   Weeks, S. L.; Chaukulkar, R. P.; Stradins, P.; Agarwal, S. Photoluminescence behavior of plasma synthesized Si nanocrystals oxidized at low temperature in pure O$_2$ and H$_2$O. *J. Vac. Sci. Technol., A* **2014,** *32*, 050604.

(51)   Brawand, N. P.; Voros, M.; Galli, G. Surface dangling bonds are a cause of B-type blinking in Si nanoparticles. *Nanoscale* **2015,** *7*, 3737.

(52)   Miller, J. B.; Dandu, N.; Velizhanin, K. A.; Anthony, R. J.; Kortshagen, U. R.; Kroll, D. M.; Kilina, S.; Hobbie, E. K. Enhanced Luminescent Stability through Particle Interactions in Silicon Nanocrystal Aggregates. *ACS Nano* **2015,** *9*, 9772.

REFERENCES CITED FOR CHAPTER IV

(1)   Govoni, M.; Marri, I.; Ossicini, S. Carrier multiplication between interacting nanocrystals for fostering silicon-based photovoltaics. *Nat. Photonics* **2012,** *6*, 672.

(2)   Cho, E. C.; Park, S.; Hao, X.; Song, D.; Conibeer, G.; Park, S. C.; Green, M. A. Silicon quantum dot/crystalline silicon solar cells. *Nanotechnology* **2008,** *19*, 245201.

(3)   Baxter, J. B.; Aydil, E. S. Nanowire-based dye-sensitized solar cells. *Appl. Phys. Lett.* **2005,** *86*, 1.

(4)   Plass, R.; Pelet, S.; Krueger, J.; Gratzel, M.; Bach, U. Quantum dot sensitization of organic-inorganic hybrid solar cells. *J. Phys. Chem. B* **2002,** *106*, 7578.

(5)   Xin, Y.; Nishio, K.; Saitow, K. I. White-blue electroluminescence from a Si quantum dot hybrid light-emitting diode. *Appl. Phys. Lett.* **2015,** *106*, 201102.

(6)   Hirschman, K. D.; Tsybeskov, L.; Duttagupta, S. P.; Fauchet, P. M. Silicon-based visible light-emitting devices integrated into microelectronic circuits. *Nature* **1996,** *384*, 338.

(7)   Gao, X. H.; Cui, Y. Y.; Levenson, R. M.; Chung, L. W. K.; Nie, S. M. In vivo cancer targeting and imaging with semiconductor quantum dots. *Nat. Biotechnol.* **2004,** *22*, 969.

(8)   Park, J.-H.; Gu, L.; von Maltzahn, G.; Ruoslahti, E.; Bhatia, S. N.; Sailor, M. J. Biodegradable luminescent porous silicon nanoparticles for in vivo applications. *Nat. Methods* **2009,** *8*, 331.

(9)   Buriak, J. M. Organometallic chemistry on silicon surfaces: formation of functional monolayers bound through Si-C bonds. *Chem. Commun.* **1999**, 1051.

(10)   Aldana, J.; Wang, Y. A.; Peng, X. G. Photochemical instability of CdSe nanocrystals coated by hydrophilic thiols. *J. Am. Chem. Soc.* **2001,** *123*, 8844.

(11)   Wilson, W. L.; Szajowski, P. F.; Brus, L. E. Quantum confinement in size-selected, surface-oxidized silicon nanocrystals. *Science* **1993,** *262*, 1242.

(12)   Pavesi, L.; Dal Negro, L.; Mazzoleni, C.; Franzo, G.; Priolo, F. Optical gain in silicon nanocrystals. *Nature* **2000,** *408*, 440.

(13)   Anthony, R.; Kortshagen, U. Photoluminescence quantum yields of amorphous and crystalline silicon nanoparticles. *Phys. Rev. B* **2009,** *80.*

(14)   Timmerman, D.; Valenta, J.; Dohnalova, K.; de Boer, W. D. A. M.; Gregorkiewicz, T. Step-like enhancement of luminescence quantum yield of silicon nanocrystals. *Nat. Nanotechnol.* **2011,** *6*, 710.

(15)   Trani, F.; Cantele, G.; Ninno, D.; Iadonisi, G. Tight-binding calculation of the optical absorption cross section of spherical and ellipsoidal silicon nanocrystals. *Phys. Rev. B* **2005,** *72*, 075423.

(16)   Kocevski, V.; Eriksson, O.; Rusz, J. Transition between direct and indirect band gap in silicon nanocrystals. *Phys. Rev. B* **2013,** *87*, 245401.

(17)   Hapala, P.; Kusova, K.; Pelant, I.; Jelinek, P. Theoretical analysis of electronic band structure of 2- to 3-nm Si nanocrystals. *Phys. Rev. B* **2013,** *87*, 195420.

(18)   DeBenedetti, W. J. I.; Chiu, S. K.; Radlinger, C. M.; Ellison, R. J.; Manhat, B. A.; Zhang, J. Z.; Shi, J. Y.; Goforth, A. M. Conversion from Red to Blue Photoluminescence in Alcohol Dispersions of Alkyl-Capped Silicon Nanoparticles: Insight into the Origins of Visible Photoluminescence in Colloidal Nanocrystalline Silicon. *J. Phys. Chem. C* **2015,** *119*, 9595.

(19)   Gelloz, B.; Sano, H.; Boukherroub, R.; Wayner, D. D. M.; Lockwood, D. J.; Koshida, N. Stabilization of porous silicon electroluminescence by surface passivation with controlled covalent bonds. *Appl. Phys. Lett.* **2003,** *83*, 2342.

(20)   Wheeler, L. M.; Neale, N. R.; Chen, T.; Kortshagen, U. R. Hypervalent surface interactions for colloidal stability and doping of silicon nanocrystals. *Nat. Commun.* **2013,** *4*, 1.

(21)   Holmes, J. D.; Ziegler, K. J.; Doty, R. C.; Pell, L. E.; Johnston, K. P.; Korgel, B. A. Highly luminescent silicon nanocrystals with discrete optical transitions. *J. Am. Chem. Soc.* **2001,** *123*, 3743.

(22)   English, D. S.; Pell, L. E.; Yu, Z. H.; Barbara, P. F.; Korgel, B. A. Size tunable visible luminescence from individual organic monolayer stabilized silicon nanocrystal quantum dots. *Nano Lett.* **2002,** *2,* 681.

(23)   Ding, Y.; Sugaya, M.; Liu, Q.; Zhou, S.; Nozaki, T. Oxygen passivation of silicon nanocrystals: Influences on trap states, electron mobility, and hybrid solar cell performance. *Nano Energy* **2014,** *10*, 322.

(24)   Keunen, K.; Stesmans, A.; Afanas'ev, V. V. Inherent Si dangling bond defects at the thermal $(110)Si/SiO_2$ interface. *Phys. Rev. B* **2011,** *84*, 085329.

(25)   Li, Y.; Liang, P.; Hu, Z.; Guo, S.; You, Q.; Sun, J.; Xu, N.; Wu, J. Enhancement and stability of photoluminescence from Si nanocrystals embedded in a SiO_2 matrix by H_2-passivation. *Appl. Surf. Sci.* **2014,** *300*, 178.

(26)   Reboredo, F. A.; Galli, G. Theory of alkyl-terminated silicon quantum dots. *J. Phys. Chem. B* **2005,** *109*, 1072.

(27)   Pereira, R. N.; Rowe, D. J.; Anthony, R. J.; Kortshagen, U. Oxidation of freestanding silicon nanocrystals probed with electron spin resonance of interfacial dangling bonds. *Phys. Rev. B* **2011,** *83*, 155327.

(28)   Saito, Y.; Yoshida, A. Vacuum-Ultraviolet-Light-Induced Defects in Hydrogenated Amorphous-Silicon Films. *Philos. Mag. B* **1992,** *66*, 219.

(29)   Wu, J. J.; Kortshagen, U. R. Photostability of thermally-hydrosilylated silicon quantum dots. *Rsc Advances* **2015,** *5*, 103822.

(30)   Li, H. S.; Wu, Z. G.; Lusk, M. T. Dangling Bond Defects: The Critical Roadblock to Efficient Photoconversion in Hybrid Quantum Dot Solar Cells. *J. Phys. Chem. C* **2014,** *118*, 46.

(31)   Lannoo, M.; Delerue, C.; Allan, G. Nonradiative Recombination on Dangling Bonds in Silicon Crystallites. *J. Lumin.* **1993,** *57*, 243.

(32)   Brawand, N. P.; Voros, M.; Galli, G. Surface dangling bonds are a cause of B-type blinking in Si nanoparticles. *Nanoscale* **2015,** *7*, 3737.

(33)   Liu, C.-Y.; Holman, Z. C.; Kortshagen, U. R. Hybrid solar cells from P3HT and silicon nanocrystals. *Nano Lett.* **2009,** *9*, 449.

(34)   Miller, J. B.; Dandu, N.; Velizhanin, K. A.; Anthony, R. J.; Kortshagen, U. R.; Kroll, D. M.; Kilina, S.; Hobbie, E. K. Enhanced Luminescent Stability through Particle Interactions in Silicon Nanocrystal Aggregates. *ACS Nano* **2015,** *9*, 9772.

(35)   Hamers, R. J. Characterization of localized atomic surface defects by tunneling microscopy and spectroscopy. *J. Vac. Sci. Technol., B* **1988,** *6*, 1462.

(36)   Labidi, H.; Taucer, M.; Rashidi, M.; Koleini, M.; Livadaru, L.; Pitters, J.; Cloutier, M.; Salomons, M.; Wolkow, R. A. Scanning tunneling spectroscopy reveals a silicon dangling bond charge state transition. *New J. Phys.* **2015,** *17*, 073023.

(37)   Piva, P. G.; DiLabio, G. A.; Livadaru, L.; Wolkow, R. A. Atom-scale surface reactivity mediated by long-ranged equilibrium charge transfer. *Phys. Rev. B* **2014,** *90*, 155422.

(38)   Schofield, S. R.; Studer, P.; Hirjibehedin, C. F.; Curson, N. J.; Aeppli, G.; Bowler, D. R. Quantum engineering at the silicon surface using dangling bonds. *Nat Commun* **2013,** *4*, 1649.

(39)   Chen, C. J. *Introduction to Scanning Tunneling Microscopy.* 2nd ed.; Oxford University Press: New York, 2008.

(40)   Haider, M. B.; Pitters, J. L.; Dilabio, G. A.; Livadaru, L.; Mutus, J. Y.; Wolkow, R. A. Controlled coupling and occupation of silicon atomic quantum dots at room temperature. *Phys. Rev. Lett.* **2009,** *102*, 046805.

(41)   Pitters, J. L.; Livadaru, L.; Haider, M. B.; Wolkow, R. A. Tunnel coupled dangling bond structures on hydrogen terminated silicon surfaces. *J. Chem. Phys.* **2011,** *134*, 064712.

(42)   Engelund, M.; Zuzak, R.; Godlewski, S.; Kolmer, M.; Frederiksen, T.; García-Lekue, A.; Sánchez-Portal, D.; Szymonski, M. Tunneling spectroscopy of close-spaced dangling-bond pairs in Si(001):H. *Sci. Rep.* **2015,** *5*, 14496.

(43)   Wolf, O.; Dasog, M.; Yang, Z.; Balberg, I.; Veinot, J. G. C.; Millo, O. Doping and quantum confinement effects in single Si nanocrystals observed by scanning tunneling spectroscopy. *Nano Lett.* **2013,** *13*, 2516.

(44)   Kislitsyn, D. A.; Kocevski, V.; Mills, J. M.; Chiu, S. K.; Gervasi, C. F.; Taber, B. N.; Rosenfield, A. E.; Eriksson, O.; Rusz, J.; Goforth, A. M.; Nazin, G. V. Mapping of Defects in Individual Silicon Nanocrystals Using Real-Space Spectroscopy. *J Phys Chem Lett* **2016,** *7*, 1047.

(45)   Hackley, J. D.; Kislitsyn, D. A.; Beaman, D. K.; Ulrich, S.; Nazin, G. V. High-stability cryogenic scanning tunneling microscope based on a closed-cycle cryostat. *Rev. Sci. Instrum.* **2014,** *85*, 103704.

(46)   Chiu, S.-K.; Manhat, B. A.; DeBenedetti, W. J. I.; Brown, A. L.; Fichter, K.; Vu, T.; Eastman, M.; Jiao, J.; Goforth, A. M. Aqueous red-emitting silicon nanoparticles for cellular imaging: Consequences of protecting against surface passivation by hydroxide and water for stable red emission. *J. Mater. Res.* **2013,** *28*, 216.

(47)   Ordejon, P.; Artacho, E.; Soler, J. M. Self-consistent order-N density-functional calculations for very large systems. *Phys. Rev. B* **1996,** *53*, 10441.

(48)   Soler, J. M.; Artacho, E.; Gale, J. D.; Garcia, A.; Junquera, J.; Ordejon, P.; Sanchez-Portal, D. The SIESTA method for ab initio order-N materials simulation. *J. Phys.: Condens. Matter* **2002,** *14*, 2745.

(49)   Kocevski, V.; Eriksson, O.; Rusz, J. Size dependence of the stability, electronic structure, and optical properties of silicon nanocrystals with various surface impurities. *Phys. Rev. B* **2015,** *91*, 1.

(50)   Soukiassian, L.; Mayne, A. J.; Carbone, M.; Dujardin, G. Atomic-scale desorption of H atoms from the Si(100)−2×1:H surface: Inelastic electron interactions. *Phys. Rev. B* **2003,** *68*, 035303.

(51)   Bellec, A.; Riedel, D.; Dujardin, G.; Boudrioua, O.; Chaput, L.; Stauffer, L.; Sonnet, P. Electronic properties of the n-doped hydrogenated silicon (100) surface and dehydrogenated structures at 5 K. *Phys. Rev. B* **2009,** *80*, 245434.

(52)   Ye, W.; Min, K.; Peña Martin, P.; Rockett, A. A.; Aluru, N. R.; Lyding, J. W. Scanning tunneling spectroscopy and density functional calculation of silicon dangling bonds on the Si(100)-2×1:H surface. *Surf. Sci.* **2013,** *609*, 147.

(53)   Shen, T. C.; Wang, C.; Abeln, G. C.; Tucker, J. R.; Lyding, J. W.; Avouris, P.; Walkup, R. E. Atomic-scale desorption through electronic and vibrational excitation mechanisms. *Science* **1995,** *268*, 1590.

(54)   Becker, R. S.; Higashi, G. S.; Chabal, Y. J.; Becker, A. J. Atomic-scale conversion of clean Si(111):H-1×1 to Si(111)-2×1 by electron-stimulated desorption. *Phys. Rev. Lett.* **1990,** *65*, 1917.

(55)   Bellec, A.; Riedel, D.; Dujardin, G.; Rompotis, N.; Kantorovich, L. N. Dihydride dimer structures on the Si(100):H surface studied by low-temperature scanning tunneling microscopy. *Phys. Rev. B* **2008,** *78,* 165302.

(56)   Avouris, P.; Walkup, R. E.; Rossi, a. R.; Akpati, H. C.; Nordlander, P.; Shen, T. C.; Abeln, G. C.; Lyding, J. W. Breaking individual chemical bonds via STM-induced excitations. *Surf. Sci.* **1996,** *363,* 368.

(57)   Nazin, G. V.; Wu, S. W.; Ho, W. Tunneling rates in electron transport through double-barrier molecular junctions in a scanning tunneling microscope. *Proc. Natl. Acad. Sci. U. S. A.* **2005,** *102,* 8832.

(58)   Nazin, G. V.; Qiu, X. H.; Ho, W. Vibrational spectroscopy of individual doping centers in a monolayer organic crystal. *J. Chem. Phys.* **2005,** *122,* 181105.

(59)   Sun, Z.; Swart, I.; Delerue, C.; Vanmaekelbergh, D.; Liljeroth, P. Orbital and charge-resolved polaron states in CdSe dots and rods probed by scanning tunneling spectroscopy. *Phys. Rev. Lett.* **2009,** *102,* 196401.

(60)   Pradhan, N. A.; Liu, N.; Silien, C.; Ho, W. Tuning the bipolar conductance of an alkali-doped C60 layer sandwiched between two tunneling barriers. *Nano Lett.* **2005,** *5,* 55.

(61)   Wu, S. W.; Nazin, G. V.; Chen, X.; Qiu, X. H.; Ho, W. Control of relative tunneling rates in single molecule bipolar electron transport. *Phys. Rev. Lett.* **2004,** *93*.

(62)   Bellec, A.; Chaput, L.; Dujardin, G.; Riedel, D.; Stauffer, L.; Sonnet, P. Reversible charge storage in a single silicon atom. *Phys. Rev. B* **2013,** *88,* 241406.

(63)   Wu, S. W.; Ogawa, N.; Nazin, G. V.; Ho, W. Conductance hysteresis and switching in a single-molecule junction. *J. Phys. Chem. C* **2008,** *112,* 5241.

(64)   Brown, G. W.; Grube, H.; Hawley, M. E.; Schofield, S. R.; Curson, N. J.; Simmons, M. Y.; Clark, R. G. Imaging charged defects on clean Si(100)-(2×1) with scanning tunneling microscopy. *J. Appl. Phys.* **2002,** *92,* 820.

REFERENCES CITED FOR CHAPTER V

(1)   Govoni, M.; Marri, I.; Ossicini, S. Carrier multiplication between interacting nanocrystals for fostering silicon-based photovoltaics. *Nat. Photonics* **2012,** *6*, 672.

(2)   Cho, E. C.; Park, S.; Hao, X.; Song, D.; Conibeer, G.; Park, S. C.; Green, M. A. Silicon quantum dot/crystalline silicon solar cells. *Nanotechnology* **2008,** *19*, 245201.

(3)   Baxter, J. B.; Aydil, E. S. Nanowire-based dye-sensitized solar cells. *Appl. Phys. Lett.* **2005,** *86*, 1.

(4)   Plass, R.; Pelet, S.; Krueger, J.; Grätzel, M.; Bach, U. Quantum dot sensitization of organic-inorganic hybrid solar cells. *J. Phys. Chem. B* **2002,** *106*, 7578.

(5)   Xin, Y.; Nishio, K.; Saitow, K. I. White-blue electroluminescence from a Si quantum dot hybrid light-emitting diode. *Appl. Phys. Lett.* **2015,** *106*, 201102.

(6)   Hirschman, K. D.; Tsybeskov, L.; Duttagupta, S. P.; Fauchet, P. M. Silicon-based visible light-emitting devices integrated into microelectronic circuits. *Nature* **1996,** *384*, 338.

(7)   Dasog, M.; Kehrle, J.; Rieger, B.; Veinot, J. G. C. Silicon Nanocrystals and Silicon-Polymer Hybrids: Synthesis, Surface Engineering, and Applications. *Angew. Chem. Int. Ed.* **2016,** *55*, 2322.

(8)   Ashby, S. P.; Thomas, J. A.; García-Cañadas, J.; Min, G.; Corps, J.; Powell, A. V.; Xu, H.; Shen, W.; Chao, Y. Bridging silicon nanoparticles and thermoelectrics: Phenylacetylene functionalization. *Faraday Discuss.* **2014,** *176*, 349.

(9)   Gao, X.; Cui, Y.; Levenson, R. M.; Chung, L. W. K.; Nie, S. In vivo cancer targeting and imaging with semiconductor quantum dots. *Nat. Biotechnol.* **2004,** *22*, 969.

(10)   Park, J.-H.; Gu, L.; von Maltzahn, G.; Ruoslahti, E.; Bhatia, S. N.; Sailor, M. J. Biodegradable luminescent porous silicon nanoparticles for in vivo applications. *Nat. Methods* **2009,** *8*, 331.

(11)   Dohnalová, K.; Gregorkiewicz, T.; Kůsová, K. Silicon quantum dots: surface matters. *J. Phys.: Condens. Matter* **2014,** *26*, 173201.

(12)   Chen, C. J. *Introduction to Scanning Tunneling Microscopy*. 2nd ed.; Oxford University Press: New York, 2008.

(13)   Wolf, O.; Dasog, M.; Yang, Z.; Balberg, I.; Veinot, J. G. C.; Millo, O. Doping and quantum confinement effects in single Si nanocrystals observed by scanning tunneling spectroscopy. *Nano Lett.* **2013,** *13*, 2516.

(14)   Kislitsyn, D. A.; Kocevski, V.; Mills, J. M.; Chiu, S. K.; Gervasi, C. F.; Taber, B. N.; Rosenfield, A. E.; Eriksson, O.; Rusz, J.; Goforth, A. M.; Nazin, G. V. Mapping of Defects in Individual Silicon Nanocrystals Using Real-Space Spectroscopy. *J Phys Chem Lett* **2016,** *7*, 1047.

(15)   Kislitsyn, D. A.; Mills, J. M.; Kocevski, V.; Chiu, S. K.; DeBenedetti, W. J. I.; Gervasi, C. F.; Taber, B. N.; Rosenfield, A. E.; Eriksson, O.; Rusz, J.; Goforth, A. M.; Nazin, G. V. Communication: Visualization and spectroscopy of defects induced by dehydrogenation in individual silicon nanocrystals. *J. Chem. Phys.* **2016,** *144*, 241102.

(16)   Panthani, M. G.; Hessel, C. M.; Reid, D.; Casillas, G.; José-Yacamán, M.; Korgel, B. A. Graphene-supported high-resolution TEM and STEM imaging of silicon nanocrystals and their capping ligands. *J. Phys. Chem. C* **2012,** *116*, 22463.

(17)   Hannah, D. C.; Yang, J.; Kramer, N. J.; Schatz, G. C.; Kortshagen, U. R.; Schaller, R. D. Ultrafast Photoluminescence in Quantum-Confined Silicon Nanocrystals Arises from an Amorphous Surface Layer. *ACS Photonics* **2014,** *1*, 960.

(18)   Bagolini, L.; Mattoni, A.; Fugallo, G.; Colombo, L.; Poliani, E.; Sanguinetti, S.; Grilli, E. Quantum confinement by an order-disorder boundary in nanocrystalline silicon. *Phys. Rev. Lett.* **2010,** *104*, 176803.

(19)   Bagolini, L.; Mattoni, A.; Collins, R. T.; Lusk, M. T. Carrier localization in nanocrystalline silicon. *J. Phys. Chem. C* **2014,** *118*, 13417.

(20)   Mueller, T.; Johlin, E.; Grossman, J. C. Origins of hole traps in hydrogenated nanocrystalline and amorphous silicon revealed through machine learning. *Phys. Rev. B* **2014,** *89*, 115202.

(21)   Hackley, J. D.; Kislitsyn, D. A.; Beaman, D. K.; Ulrich, S.; Nazin, G. V. High-stability cryogenic scanning tunneling microscope based on a closed-cycle cryostat. *Rev. Sci. Instrum.* **2014,** *85*, 103704.

(22)   Chiu, S.-K.; Manhat, B. A.; DeBenedetti, W. J. I.; Brown, A. L.; Fichter, K.; Vu, T.; Eastman, M.; Jiao, J.; Goforth, A. M. Aqueous red-emitting silicon nanoparticles for cellular imaging: Consequences of protecting against surface passivation by hydroxide and water for stable red emission. *J. Mater. Res.* **2013,** *28*, 216.

(23)   Wagner, L. K.; Grossman, J. C. Microscopic description of light induced defects in amorphous silicon solar cells. *Phys. Rev. Lett.* **2008,** *101*, 265501.

(24)   Sun, Z.; Swart, I.; Delerue, C.; Vanmaekelbergh, D.; Liljeroth, P. Orbital and charge-resolved polaron states in CdSe dots and rods probed by scanning tunneling spectroscopy. *Phys. Rev. Lett.* **2009,** *102*, 196401.

(25)   Wolkin, M. V.; Jorne, J.; Fauchet, P. M.; Allan, G.; Delerue, C. Electronic states and luminescence in porous silicon quantum dots: The role of oxygen. *Phys. Rev. Lett.* **1999,** *82*, 197.

(26)   Puzder, A.; Williamson, A. J.; Grossman, J. C.; Galli, G. Surface control of optical properties in silicon nanoclusters. *J. Chem. Phys.* **2002,** *117,* 6721.

(27)   Vasiliev, I.; Chelikowsky, J. R.; Martin, R. M. Surface oxidation effects on the optical properties of silicon nanocrystals. *Phys. Rev. B* **2002,** *65*, 121302.

(28)   Puzder, A.; Williamson, A. J.; Grossman, J. C.; Galli, G. Surface Chemistry of Silicon Nanoclusters. *Phys. Rev. Lett.* **2002,** *88*, 4.

(29)   Brawand, N. P.; Voros, M.; Galli, G. Surface dangling bonds are a cause of B-type blinking in Si nanoparticles. *Nanoscale* **2015,** *7*, 3737.

(30)   Stokbro, K.; Quaade, U. J.; Lin, R.; Thirstrup, C.; Grey, F. Electronic mechanism of STM-induced diffusion of hydrogen on Si(100). *Faraday Discuss.* **2000,** *117*, 231.

(31)   Bellec, A.; Riedel, D.; Dujardin, G.; Boudrioua, O.; Chaput, L.; Stauffer, L.; Sonnet, P. Nonlocal activation of a bistable atom through a surface state charge-transfer process on Si(100)-(2×1):H. *Phys. Rev. Lett.* **2010,** *105*, 048302.

(32)   Dürr, M.; Höfer, U. Hydrogen diffusion on silicon surfaces. *Prog. Surf. Sci.* **2013,** *88*, 61.

(33)   Ghosh, B.; Takeguchi, M.; Nakamura, J.; Nemoto, Y.; Hamaoka, T.; Chandra, S.; Shirahata, N. Origin of the Photoluminescence Quantum Yields Enhanced by Alkane-Termination of Freestanding Silicon Nanocrystals: Temperature-Dependence of Optical Properties. *Sci. Rep.* **2016,** *6*, 1.

(34)   Petkov, V.; Hessel, C. M.; Ovtchinnikoff, J.; Guillaussier, A.; Korgel, B. A.; Liu, X. F.; Giordano, C. Structure-Properties Correlation in Si Nanoparticles by Total Scattering and Computer Simulations. *Chem. Mater.* **2013,** *25*, 2365.

(35)   Ritchie, A.; Cao, W.; Dasog, M.; Purkait, T. K.; Senger, C.; Hu, Y. F.; Xiao, Q. F.; Veinot, J. G. C.; Urquhart, S. G. Silicon 1s near edge X-ray absorption fine structure spectroscopy of functionalized silicon nanocrystals. *J. Chem. Phys.* **2016,** *145*, 154703.

(36)   Harris, J. T.; Hueso, J. L.; Korgel, B. A. Hydrogenated amorphous silicon (a-Si:H) colloids. *Chem. Mater.* **2010,** *22*, 6378.

(37)   Trani, F.; Cantele, G.; Ninno, D.; Iadonisi, G. Tight-binding calculation of the optical absorption cross section of spherical and ellipsoidal silicon nanocrystals. *Phys. Rev. B* **2005,** *72*, 075423.

(38)   Kocevski, V.; Eriksson, O.; Rusz, J. Transition between direct and indirect band gap in silicon nanocrystals. *Phys. Rev. B* **2013,** *87*, 245401.

(39)   Hapala, P.; Kusova, K.; Pelant, I.; Jelinek, P. Theoretical analysis of electronic band structure of 2- to 3-nm Si nanocrystals. *Phys. Rev. B* **2013,** *87*, 195420.

(40)   Khomyakov, P. A.; Andreoni, W.; Afify, N. D.; Curioni, A. Large-scale simulations of a-Si:H: The origin of mdgap sates rvisited. *Phys. Rev. Lett.* **2011,** *107*, 255502.

(41)   Pan, Y.; Inam, F.; Zhang, M.; Drabold, D. A. Atomistic origin of Urbach tails in amorphous silicon. *Phys. Rev. Lett.* **2008,** *100*, 206403.

(42)   Staebler, D. L.; Wronski, C. R. Reversible conductivity changes in discharge-produced amorphous Si. *Appl. Phys. Lett.* **1977,** *31*, 292.

(43)   Johlin, E.; Wagner, L. K.; Buonassisi, T.; Grossman, J. C. Origins of structural hole traps in hydrogenated amorphous silicon. *Phys. Rev. Lett.* **2013,** *110*, 146805.

(44)   Repp, J.; Meyer, G.; Olsson, F. E.; Persson, M. Controlling the charge state of individual gold adatoms. *Science* **2004,** *305*, 493.

(45)   Wu, S. W.; Ogawa, N.; Nazin, G. V.; Ho, W. Conductance hysteresis and switching in a single-molecule junction. *J. Phys. Chem. C* **2008,** *112*, 5241.

REFERENCES CITED FOR CHAPTER VI

(1)   Inouye, C. S.; Pong, W. Ultraviolet photoelectron spectra of rubidium halides. *Phys. Rev. B* **1977,** *15*, 2265.

(2)   Fröhlich, D.; Staginnus, B. New assignment of the band gap in the alkali bromides by two-photon spectroscopy. *Phys. Rev. Lett.* **1967,** *19*, 496.

(3)   Brown, F. C.; Gahwiller, C.; Fujita, H.; Kunz, A. B.; Scheifley, W.; Carrera, N. Extreme-Ultraviolet Spectra of Ionic Crystals. *Phys. Rev. B* **1970,** *2*, 2126.

(4)   Rothberg, G. M.; Eisenstadt, M.; Kusch, P. Free evaporation of alkali halide crystals. *J. Chem. Phys.* **1959,** *30*, 517.

(5)   Tasker, P. W. Surface Energies, Surface Tensions and Surface-Structure of the Alkali-Halide Crystals. *Philos. Mag. A* **1979,** *39*, 119.

(6)   Gerß, B.; Osterloh, N.; Heidorn, S. C.; Morgenstern, K. Diffusion limited aggregation in low temperature growth of sodium chloride. *Cryst. Growth Des.* **2015,** *15*, 3046.

(7)   Pivetta, M.; Patthey, F.; Stengel, M.; Baldereschi, A.; Schneider, W.-D. Local work function Moiré pattern on ultrathin ionic films: NaCl on Ag(100). *Phys. Rev. B* **2005,** *72*, 115404.

(8)   Calupitan, J. P. D. C.; Guillermet, O.; Galangau, O.; Yengui, M.; Echeverría, J.; Bouju, X.; Nakashima, T.; Rapenne, G.; Coratger, R.; Kawai, T. Adsorption of Terarylenes on Ag(111) and NaCl(001)/Ag(111): A Scanning Tunneling Microscopy and Density Functional Theory Study. *J. Phys. Chem. C* **2018,** *122*, 5978.

(9)   Heidorn, S.; Bertram, C.; Koch, J.; Boom, K.; Matthaei, F.; Safiei, A.; Henzl, J.; Morgenstern, K. Influence of substrate surface-induced defects on the interface state between NaCl(100) and Ag(111). *J. Phys. Chem. C* **2013,** *117*, 16095.

(10)   Hebenstreit, W.; Schmid, M.; Redinger, J.; Podloucky, R.; Varga, P. Bulk terminated NaCl(111) on aluminum: a polar surface of an ionic crystal? *Phys. Rev. Lett.* **2000,** *85*, 5376.

(11)   Hebenstreit, W.; Redinger, J.; Horozova, Z.; Schmid, M.; Podloucky, R.; Varga, P. Atomic resolution by STM on ultra-thin films of alkali halides: Experiment and local density calculations. *Surf. Sci.* **1999,** *424*, L321.

(12)   Lauwaet, K.; Schouteden, K.; Janssens, E.; Van Haesendonck, C.; Lievens, P.; Trioni, M. I.; Giordano, L.; Pacchioni, G. Resolving all atoms of an alkali halide via nanomodulation of the thin NaCl film surface using the Au(111) reconstruction. *Phys. Rev. B* **2012,** *85*, 245440.

(13)   Lauwaet, K.; Schouteden, K.; Janssens, E.; Van Haesendonck, C.; Lievens, P. Dependence of the NaCl/Au(111) interface state on the thickness of the NaCl layer. *J. Phys.: Condens. Matter* **2012,** *24*, 475507.

(14)   Bombis, C.; Kalashnyk, N.; Xu, W.; Lægsgaard, E.; Besenbacher, F.; Linderoth, T. R.; Besenbacher, F.; Linderoth, T. R. Hydrogen-bonded molecular networks of melamine and cyanuric acid on thin films of naCl on Au(111). *Small* **2009,** *5*, 2177.

(15)   Cañas-Ventura, M. E.; Xiao, W.; Ruffieux, P.; Rieger, R.; Müllen, K.; Brune, H.; Fasel, R. Stabilization of bimolecular islands on ultrathin NaCl films by a vicinal substrate. *Surf. Sci.* **2009,** *603*, 2294.

(16)   Sun, X.; Felicissimo, M. P.; Rudolf, P.; Silly, F. NaCl multi-layer islands grown on Au(111)-(22×√3) probed by scanning tunneling microscopy. *Nanotechnology* **2008,** *19*.

(17)   Olsson, F. E.; Persson, M. A density functional study of adsorption of sodium-chloride overlayers on a stepped and a flat copper surface. *Surf. Sci.* **2003,** *540*, 172.

(18)   Bombis, C.; Ample, F.; Mielke, J.; Mannsberger, M.; Villagómez, C. J.; Roth, C.; Joachim, C.; Grill, L. Mechanical behavior of nanocrystalline NaCl Islands on Cu(111). *Phys. Rev. Lett.* **2010,** *104*, 185502.

(19)   Repp, J.; Meyer, G.; Olsson, F. E.; Persson, M. Controlling the charge state of individual gold adatoms. *Science* **2004,** *305*, 493.

(20)   Swart, I.; Sonnleitner, T.; Repp, J. Charge state control of molecules reveals modification of the tunneling barrier with intramolecular contrast. *Nano Lett.* **2011,** *11*, 1580.

(21)   Olsson, F. E.; Persson, M.; Repp, J.; Meyer, G. Scanning tunneling microscopy and spectroscopy of NaCl overlayers on the stepped Cu(311) surface: Experimental and theoretical study. *Phys. Rev. B* **2005,** *71*, 075419.

(22)   Riemann, A.; Folsch, S.; Rieder, K. H. Epitaxial growth of alkali halides on stepped metal surfaces. *Phys. Rev. B* **2005,** *72*, 125423.

(23)   Repp, J.; Liljeroth, P.; Meyer, G. Coherent electron–nuclear coupling in oligothiophene molecular wires. *Nat. Phys.* **2010,** *6*, 975.

(24)   Liljeroth, P.; Repp, J.; Meyer, G. Current-Induced Hydrogen Tautomerization and Conductance Switching of Naphthalocyanine Molecules. *Science* **2007,** *317*, 1203.

(25)   Boschker, J. E.; Momand, J.; Bragaglia, V.; Wang, R.; Perumal, K.; Giussani, A.; Kooi, B. J.; Riechert, H.; Calarco, R. Surface reconstruction-induced coincidence lattice formation between two-dimensionally bonded materials and a three-dimensionally bonded substrate. *Nano Lett.* **2014,** *14*, 3534.

(26)   Edmonds, M. T.; Hellerstedt, J. T.; Tadich, A.; Schenk, A.; Odonnell, K. M.; Tosado, J.; Butch, N. P.; Syers, P.; Paglione, J.; Fuhrer, M. S. Stability and surface reconstruction of topological insulator Bi_2Se_3 on exposure to atmosphere. *J. Phys. Chem. C* **2014,** *118*, 20413.

(27)   Hosokawa, S.; Stellhorn, J. R.; Matsushita, T.; Happo, N.; Kimura, K.; Hayashi, K.; Ebisu, Y.; Ozaki, T.; Ikemoto, H.; Setoyama, H.; Okajima, T.; Yoda, Y.; Ishii, H.; Liao, Y. F.; Kitaura, M.; Sasaki, M. Impurity position and lattice distortion in a Mn-doped Bi_2Te_3 topological insulator investigated by x-ray fluorescence holography and x-ray absorption fine structure. *Phys. Rev. B* **2017,** *96*, 214207.

(28)   Yan, B.; Stadtmuller, B.; Haag, N.; Jakobs, S.; Seidel, J.; Jungkenn, D.; Mathias, S.; Cinchetti, M.; Aeschlimann, M.; Felser, C. Topological states on the gold surface. *Nat Commun* **2015,** *6*, 10167.

(29)   Chen, W.; Madhavan, V.; Jamneala, T.; Crommie, M. Scanning Tunneling Microscopy Observation of an Electronic Superlattice at the Surface of Clean Gold. *Phys. Rev. Lett.* **1998,** *80*, 1469.

(30)   Bürgi, L.; Brune, H.; Kern, K. Imaging of electron potential landscapes on Au(111). *Phys. Rev. Lett.* **2002,** *89*, 176801.

(31)   Libisch, F.; Geringer, V.; Subramaniam, D.; Burgdorfer, J.; Morgenstern, M. Diffractive-wave guiding of surface electrons on Au(111) by the herringbone reconstruction potential. *Phys. Rev. B* **2014,** *90,* 035442.

(32)   Kislitsyn, D. A.; Taber, B. N.; Gervasi, C. F.; Mannsfeld, S. C. B.; Zhang, L.; Briseno, A. L.; Nazin, G. V. Coverage-Dependent Self-Assembly Regimes of Alkyl-Substituted Thiophene Oligomers on Au(111): Scanning Tunneling Microscopy and Spectroscopy. *J. Phys. Chem. C* **2015,** *119,* 26959.

(33)   Sykes, E. C. H.; Mantooth, B. A.; Han, P.; Donhauser, Z. J.; Weiss, P. S. Substrate-mediated intermolecular interactions: A quantitative single molecule analysis. *J. Am. Chem. Soc.* **2005,** *127,* 7255.

(34)   Böhringer, M.; Morgenstern, K.; Schneider, W. D.; Berndt, R.; Mauri, F.; De Vita, A.; Car, R. Two-dimensional self-assembly of supramolecular clusters and Chains. *Phys. Rev. Lett.* **1999,** *83,* 324.

(35)   Clair, S.; Pons, S.; Seitsonen, A. P.; Brune, H.; Kern, K.; Barth, J. V. STM study of terephthalic acid self-assembly on Au(111): Hydrogen-bonded sheets on an inhomogeneous substrate. *J. Phys. Chem. B* **2004,** *108,* 14585.

(36)   Hackley, J. D.; Kislitsyn, D. A.; Beaman, D. K.; Ulrich, S.; Nazin, G. V. High-stability cryogenic scanning tunneling microscope based on a closed-cycle cryostat. *Rev. Sci. Instrum.* **2014,** *85,* 103704.

(37)   Kresse, G.; Furthmuller, J. Efficiency of ab-initio total energy calculations for metals and semiconductors using a plane-wave basis set. *Comput. Mater. Sci.* **1996,** *6,* 15.

(38)   Kresse, G.; Furthmuller, J. Efficient iterative schemes for ab initio total-energy calculations using a plane-wave basis set. *Phys. Rev. B* **1996,** *54,* 11169.

(39)   Kresse, G.; Hafner, J. Ab initio molecular dynamics for liquid metals. *Phys. Rev. B* **1993,** *47,* 558.

(40)   Blöchl, P. E. Projector augmented-wave method. *Phys. Rev. B* **1994,** *50,* 17953.

(41)   Perdew, J. P.; Ruzsinszky, A.; Csonka, G. I.; Vydrov, O. A.; Scuseria, G. E.; Constantin, L. A.; Zhou, X.; Burke, K. Restoring the density-gradient expansion for exchange in solids and surfaces. *Phys. Rev. Lett.* **2008,** *100,* 136406.

(42)   Krukau, A. V.; Vydrov, O. A.; Izmaylov, A. F.; Scuseria, G. E. Influence of the exchange screening parameter on the performance of screened hybrid functionals. *J. Chem. Phys.* **2006,** *125,* 224106.

(43)   Henkelman, G.; Arnaldsson, A.; Jonsson, H. A fast and robust algorithm for Bader decomposition of charge density. *Comp Mater Sci* **2006,** *36,* 354.

(44)   Sanville, E.; Kenny, S. D.; Smith, R.; Henkelman, G. Improved grid-based algorithm for Bader charge allocation. *J. Comput. Chem.* **2007,** *28,* 899.

(45)   Tang, W.; Sanville, E.; Henkelman, G. A grid-based Bader analysis algorithm without lattice bias. *J Phys Condens Matter* **2009,** *21,* 084204.

(46)   Yu, M.; Trinkle, D. R. Accurate and efficient algorithm for Bader charge integration. *J. Chem. Phys.* **2011,** *134,* 064111.

(47)   Momma, K.; Izumi, F. VESTA 3 for three-dimensional visualization of crystal, volumetric and morphology data. *J. Appl. Crystallogr.* **2011,** *44,* 1272.

(48)   Chen, C. J. *Introduction to Scanning Tunneling Microscopy.* 2nd ed.; Oxford University Press: New York, 2008.

(49)   Tikhomirova, K. A.; Tantardini, C.; Sukhanova, E. V.; Popov, Z. I.; Evlashin, S. A.; Tarkhov, M. A.; Zhdanov, V. L.; Dudin, A. A.; Oganov, A. R.; Kvashnin, D. G.; Kvashnin, A. G. Exotic Two-Dimensional Structure: The First Case of Hexagonal NaCl. *J Phys Chem Lett* **2020,** *11,* 3821.

REFERENCES CITED FOR CHAPTER VII

(1)   Tersoff, J. Low-frequency noise in nanoscale ballistic transistors. *Nano Lett.* **2007,** *7,* 194.

(2)   Javey, A.; Guo, J.; Wang, Q.; Lundstrom, M.; Dai, H. J. Ballistic carbon nanotube field-effect transistors. *Nature* **2003,** *424,* 654.

(3)   Franklin, A. D. Nanomaterials in transistors: From high-performance to thin-film applications. *Science* **2015,** *349.*

(4)   Wang, N. P.; Heinze, S.; Tersoff, J. Random-telegraph-signal noise and device variability in ballistic nanotube transistors. *Nano Lett.* **2007,** *7*, 910.

(5)   Clair, S.; Shin, H. J.; Kim, Y.; Kawai, M. Electronic modulations in a single wall carbon nanotube induced by the Au(111) surface reconstruction. *Appl. Phys. Lett.* **2015,** *106*, 053111.

(6)   Hackley, J. D.; Kislitsyn, D. A.; Beaman, D. K.; Ulrich, S.; Nazin, G. V. High-stability cryogenic scanning tunneling microscope based on a closed-cycle cryostat. *Rev. Sci. Instrum.* **2014,** *85*, 103704.

(7)   Albrecht, P. M.; Lyding, J. W. Ultrahigh-vacuum scanning tunneling microscopy and spectroscopy of single-walled carbon nanotubes on hydrogen-passivated Si(100) surfaces. *Appl. Phys. Lett.* **2003,** *83*, 5029.

(8)   Clair, S.; Rabot, C.; Kim, Y.; Kawai, M. Adsorption mechanism of aligned single wall carbon nanotubes at well defined metal surfaces. *J. Vac. Sci. Technol., B* **2007,** *25*, 1143.

(9)   Shin, H. J.; Clair, S.; Kim, Y.; Kawai, M. Electronic structure of single-walled carbon nanotubes on ultrathin insulating films. *Appl. Phys. Lett.* **2008,** *93*, 233104.

(10)   Ruppalt, L. B.; Lyding, J. W. Charge transfer between semiconducting carbon nanotubes and their doped GaAs(110) and InAs(110) substrates detected by scanning tunnelling spectroscopy. *Nanotechnology* **2007,** *18*, 215202.

(11)   Repp, J.; Liljeroth, P.; Meyer, G. Coherent electron–nuclear coupling in oligothiophene molecular wires. *Nat. Phys.* **2010,** *6*, 975.

(12)   Liljeroth, P.; Repp, J.; Meyer, G. Current-Induced Hydrogen Tautomerization and Conductance Switching of Naphthalocyanine Molecules. *Science* **2007,** *317*, 1203.

(13)   Inouye, C. S.; Pong, W. Ultraviolet photoelectron spectra of rubidium halides. *Phys. Rev. B* **1977,** *15*, 2265.

(14)   Fröhlich, D.; Staginnus, B. New assignment of the band gap in the alkali bromides by two-photon spectroscopy. *Phys. Rev. Lett.* **1967,** *19*, 496.

(15)   Brown, F. C.; Gahwiller, C.; Fujita, H.; Kunz, A. B.; Scheifley, W.; Carrera, N. Extreme-Ultraviolet Spectra of Ionic Crystals. *Phys. Rev. B* **1970,** *2*, 2126.

(16)   Lauwaet, K.; Schouteden, K.; Janssens, E.; Van Haesendonck, C.; Lievens, P.; Trioni, M. I.; Giordano, L.; Pacchioni, G. Resolving all atoms of an alkali halide via nanomodulation of the thin NaCl film surface using the Au(111) reconstruction. *Phys. Rev. B* **2012,** *85*, 245440.

(17)   Fölsch, S.; Helms, A.; Zöphel, S.; Repp, J.; Meyer, G.; Rieder, K. H. Self-organized patterning of an insulator-on-metal system by surface faceting and selective growth: NaCl/Cu(211). *Phys. Rev. Lett.* **2000,** *84*, 123.

(18)   Kautz, N. A.; Kandel, S. A. Alkanethiol/Au(111) self-assembled monolayers contain gold adatoms: scanning tunneling microscopy before and after reaction with atomic hydrogen. *J. Am. Chem. Soc.* **2008,** *130*, 6908.

(19)   Fitts, W. P.; White, J. M.; Poirier, G. E. Low-coverage decanethiolate structure on Au(111): Substrate effects. *Langmuir* **2002,** *18*, 1561.

(20)   Jewell, A. D.; Tierney, H. L.; Sykes, E. C. H. Gently lifting gold's herringbone reconstruction: Trimethylphosphine on Au(111). *Phys. Rev. B* **2010,** *82*, 205401.

(21)   Liu, Y. D.; Ozolins, V. Self-Assembled Monolayers on Au(111): Structure, Energetics, and Mechanism of Reconstruction Lifting. *J. Phys. Chem. C* **2012,** *116*, 4738.

(22)   Charlier, J. C.; Blase, X.; Roche, S. Electronic and transport properties of nanotubes. *Rev. Mod. Phys.* **2007,** *79*, 677.

(23)   Smoluchowski, R. Anisotropy of the electronic work function of metals. *Phys. Rev.* **1941,** *60*, 661.

(24)   Park, J. Y.; Sacha, G. M.; Enachescu, M.; Ogletree, D. F.; Ribeiro, R. A.; Canfield, P. C.; Jenks, C. J.; Thiel, P. A.; Saenz, J. J.; Salmeron, M. Sensing dipole fields at atomic steps with combined scanning tunneling and force microscopy. *Phys. Rev. Lett.* **2005,** *95*, 136802.

(25)   Nishidate, K.; Hasegawa, M. Deformation and transfer doping of a single-walled carbon nanotube adsorbed on metallic substrates. *Phys. Rev. B* **2010,** *81*, 125414.

REFERENCES CITED FOR CHAPTER VIII

(1)   Hackley, J. D.; Kislitsyn, D. A.; Beaman, D. K.; Ulrich, S.; Nazin, G. V. High-stability cryogenic scanning tunneling microscope based on a closed-cycle cryostat. *Rev. Sci. Instrum.* **2014,** *85,* 103704.

(2)   Trout, S. R.; Graham, C. D. High field magnetic measurements on sintered SmCo5 permanent magnets. *AIP Conf. Proc.* **1976,** *29,* 608.

(3)   Fredricksen, C. J.; Nelson, E. W.; Muravjov, A. V.; Peale, R. E. High field p-Ge laser operation in permanent magnet assembly. *Infrared Phys. Technol.* **2003,** *44,* 79.

(4)   Welander, P.; Barmatz, M.; Hahn, I. New small nano-Kelvin resolution thermometer for low temperature experiments. *IEEE Trans. Instrum. Meas.* **1999,** *1,* 413.

(5)   Herbschleb, C. T.; Van Der Tuijn, P. C.; Roobol, S. B.; Navarro, V.; Bakker, J. W.; Liu, Q.; Stoltz, D.; Cañas-Ventura, M. E.; Verdoes, G.; Van Spronsen, M. A.; Bergman, M.; Crama, L.; Taminiau, I.; Ofitserov, A.; Van Baarle, G. J. C.; Frenken, J. W. M. The ReactorSTM: Atomically resolved scanning tunneling microscopy under high-pressure, high-temperature catalytic reaction conditions. *Rev. Sci. Instrum.* **2014,** *85,* 083703.

(6)   Beck, D.; Batzill, M.; Baur, C.; Kim, J.; Koel, B. E. Ultrahigh vacuum instrument that combines variable-temperature scanning tunneling microscopy with Fourier transform infrared reflection-absorption spectroscopy for studies of chemical reactions at surfaces. *Rev. Sci. Instrum.* **2002,** *73,* 1267.

(7)   Tao, F.; Tang, D.; Salmeron, M.; Somorjai, G. A. A new scanning tunneling microscope reactor used for high-pressure and high-temperature catalysis studies. *Rev. Sci. Instrum.* **2008,** *79,* 084101.

REFERENCES CITED FOR APPENDIX A

(1)   Henderson, E. J.; Kelly, J. A.; Veinot, J. G. C. Influence of $HSiO_{1.5}$ Sol-Gel Polymer Structure and Composition on the Size and Luminescent Properties of Silicon Nanocrystals. *Chem. Mater.* **2009,** *21,* 5426

REFERENCES CITED FOR APPENDIX B

(1)   Henderson, E. J.; Kelly, J. A.; Veinot, J. G. C. Influence of $HSiO_{1.5}$ Sol-Gel Polymer Structure and Composition on the Size and Luminescent Properties of Silicon Nanocrystals. *Chem. Mater.* **2009,** *21*, 5426.

(2)   Nazin, G. V.; Wu, S. W.; Ho, W. Tunneling rates in electron transport through double-barrier molecular junctions in a scanning tunneling microscope. *Proc. Natl. Acad. Sci. U. S. A.* **2005,** *102*, 8832.

(3)   Nazin, G. V.; Qiu, X. H.; Ho, W. Vibrational spectroscopy of individual doping centers in a monolayer organic crystal. *J. Chem. Phys.* **2005,** *122*, 181105.

(4)   DeBenedetti, W. J. I.; Chiu, S. K.; Radlinger, C. M.; Ellison, R. J.; Manhat, B. A.; Zhang, J. Z.; Shi, J. Y.; Goforth, A. M. Conversion from Red to Blue Photoluminescence in Alcohol Dispersions of Alkyl-Capped Silicon Nanoparticles: Insight into the Origins of Visible Photoluminescence in Colloidal Nanocrystalline Silicon. *J. Phys. Chem. C* **2015,** *119*, 9595.

(5)   Weldon, M. K.; Queeney, K. T.; Gurevich, A. B.; Stefanov, B. B.; Chabal, Y. J.; Raghavachari, K. Si–H bending modes as a probe of local chemical structure: Thermal and chemical routes to decomposition of H2O on Si(100)-(2×1). *J. Chem. Phys.* **2000,** *113*, 2440.

(6)   Ferguson, G. A.; Raghavachari, K.; Michalak, D. J.; Chabal, Y. Adsorbate−Surface Phonon Interactions in Deuterium-Passivated Si(111)-(1×1). *J. Phys. Chem. C* **2008,** *112*, 1034.

(7)   Caudano, Y.; Thiry, P. A.; Chabal, Y. J. Investigation of the bending vibrations of vicinal H/Si(111) surfaces by infrared spectroscopy. *Surf. Sci.* **2002,** *502*, 91.

(8)   Dumas, P.; Chabal, Y. J. Electron energy loss spectroscopy of H-terminated Si(111) and Si(100) prepared by chemical etching. *J. Vac. Sci. Technol., A* **1992,** *10*, 2160.

(9)   Holm, J.; Roberts, J. T. Surface chemistry of aerosolized silicon nanoparticles: evolution and desorption of hydrogen from 6-nm diameter particles. *J. Am. Chem. Soc.* **2007,** *129*, 2496.

(10)   Zhang, X.; Garfunkel, E.; Chabal, Y. J.; Christman, S. B.; Chaban, E. E. Stability of HF-etched Si(100) surfaces in oxygen ambient. *Appl. Phys. Lett.* **2001,** *79*, 4051.

REFERENCES CITED FOR APPENDIX C

(1)   Nazin, G. V.; Wu, S. W.; Ho, W. Tunneling rates in electron transport through double-barrier molecular junctions in a scanning tunneling microscope. *Proc. Natl. Acad. Sci. U. S. A.* **2005,** *102*, 8832.

(2)   Nazin, G. V.; Qiu, X. H.; Ho, W. Vibrational spectroscopy of individual doping centers in a monolayer organic crystal. *J. Chem. Phys.* **2005,** *122*, 181105.

(3)   Kislitsyn, D. A.; Mills, J. M.; Kocevski, V.; Chiu, S. K.; DeBenedetti, W. J. I.; Gervasi, C. F.; Taber, B. N.; Rosenfield, A. E.; Eriksson, O.; Rusz, J.; Goforth, A. M.; Nazin, G. V. Communication: Visualization and spectroscopy of defects induced by dehydrogenation in individual silicon nanocrystals. *J. Chem. Phys.* **2016,** *144*, 241102.

(4)   Chiu, S.-K.; Manhat, B. A.; DeBenedetti, W. J. I.; Brown, A. L.; Fichter, K.; Vu, T.; Eastman, M.; Jiao, J.; Goforth, A. M. Aqueous red-emitting silicon nanoparticles for cellular imaging: Consequences of protecting against surface passivation by hydroxide and water for stable red emission. *J. Mater. Res.* **2013,** *28*, 216.

(5)   Wei, W. S.; Xu, G. Y.; Wang, J. L.; Wang, T. M. Raman spectra of intrinsic and doped hydrogenated nanocrystalline silicon films. *Vacuum* **2007,** *81*, 656.

(6)   Richter, H.; Wang, Z. P.; Ley, L. The One Phonon Raman-Spectrum in Microcrystalline Silicon. *Solid State Commun.* **1981,** *39*, 625.